

Title	周波数変調原子間力顕微鏡を用いた力学的散逸エネルギー測定による表面電子特性の研究
Author(s)	Md Mahamudul, Hasan
Citation	
Issue Date	2022-06
Type	Thesis or Dissertation
Text version	ETD
URL	<a href="http://hdl.handle.net/10119/18032">http://hdl.handle.net/10119/18032</a>
Rights	
Description	Supervisor:富取 正彦, 先端科学技術研究科, 博士

**Study of Surface Electronic Properties through Measurement  
of Mechanical Energy Dissipation using Frequency  
Modulation Atomic Force Microscopy**

Md Mahamudul Hasan

**Japan Advanced Institute of Science and Technology**

Doctoral Dissertation

**Study of Surface Electronic Properties through Measurement  
of Mechanical Energy Dissipation using Frequency  
Modulation Atomic Force Microscopy**

Md Mahamudul Hasan

**Supervisor: Professor Dr. Masahiko Tomitori**

**Graduate School of Advanced Science and Technology  
Japan Advanced Institute of Science and Technology  
[Materials Science]**

**June 2022**

**Referee in Chief:**

**Professor Dr. Masahiko Tomitori**

Japan Advanced Institute of Science and Technology

**Referees:**

**Professor Dr. Yoshifumi Oshima**

Japan Advanced Institute of Science and Technology

**Professor Dr. Yukiko Takamura**

Japan Advanced Institute of Science and Technology

**Professor Dr. Toshu An**

Japan Advanced Institute of Science and Technology

**Professor Dr. Takashi Ichii**

Kyoto University

## Abstract

In the last three decades, a variety of surface structures of exotic materials have been profoundly investigated on a nanoscale by atomic force microscopy (AFM) using a tiny cantilever. Therein the force acting between a sample and an atomically sharpened tip on the cantilever was measured from the bending of the cantilever. While the bending was kept constant and the tip was scanned over the surface, the surface topography was depicted apparently. However, it was pointed out that damages of the tip and the sample surface often took place while scanning in contact of the tip to the sample. Toward no damage observation with high force sensitivity at an atomic level, frequency modulation (FM)-AFM was invented, in which the cantilever was oscillated at its resonance frequency ( $f$ ) and the shift of the frequency ( $\Delta f$ ) due to the change of the force was measured precisely and kept constant during scanning. Under this control, the weak force interactions were successfully measured, leading to depiction of the atom-resolved images. In the FM-AFM, the tip was able to be brought closer to the surface less than 1 nm in a stable manner. This means that we can survey the electrical and mechanical properties of the sample through the tip in close proximity to the sample surface. Based on the FM-AFM, various mechanical and electrical properties of samples have been unveiled.

Among the atom-level analysis by the FM-AFM, it is noticeable that the conservative and non-conservative (dissipative) force interactions between the tip and the sample can be separately measured. Through the non-conservative interactions, mechanical energy stored in the oscillating cantilever dissipates. One of the dissipative interactions is Joule heat induced by displacement current through the gap between a sample and the oscillating tip under an electric potential difference; the gap is simply modeled by a capacitor of two different materials of a tip and a sample. When there are resistive parts in the tip-sample system, the displacement current makes Joule heat, which decreases the mechanical oscillation energy stored in the oscillating cantilever. In the present work, the change in energy dissipation is measured by FM-AFM with a conductive tip for a mica nanosheet with varying thicknesses of nanometers placed on a conductive substrate. The mica nanosheet acts as an ultra-thin dielectric layer, which changes the capacitance between the tip and the sample. The characteristics over the conductive substrate is measured and compared with mica nanosheet varying for thin to thick layers. From the dissipation data that depends linearly on electrostatic interaction, the resistance generating the Joule heat is estimated.

In the dissertation contents, for the test sample, mica nanosheets are used, which can be regarded as a 2D single-crystal insulating material. Its minimum thickness is 1 nm. The mica nanosheets have attracted much interest owing to its high dielectric constant, excess thermal stability, and high resistivity used for quantum tunneling barriers. Phlogopite, a member of the mica family, is artificially synthesized with high purity. The perfectly cleavable basal (001) plane of phlogopite is suitable to prepare ultra-thin

nanosheets. Our developed mechanical exfoliation technique using a polyurethane hand roller is used to exfoliate and affix the nanosheet on the conductive substrate; here an iridium (Ir)-coated Si (Ir/Si) substrate is used, on which it is found for the nanosheets to be mechanically stable. The dimensions of the mica nanosheets on the substrate are measured by the FM-AFM, and the usefulness of the hand roller technique is demonstrated. For the tip, a commercially available platinum–iridium (Pt – Ir) tip on a Si cantilever is used, resulting in high-reproducible results.

The topographic and energy dissipation images of the sample surface are simultaneously observed, and the changes in the resonance frequency shift ( $\Delta f$ ) and dissipation ( $D_{\text{dis}}$ ) with respect to the sample bias voltage at our preferred set point are measured over the mica nanosheets, for example, 4-layer (4 nm), 8-layer (8 nm), 11-layer (11 nm) and 15-layer (15 nm), and no-mica (bare) regions on the Ir/Si substrate. From the  $\Delta f$ –distance curves, the numerically converted attractive forces using Sader method where stable scanning was performed at target  $\Delta f$  measured with a magnitude of  $\sim 1\text{ nN}$  over the sample surfaces. From the dissipation mapping, we observed faint contrast for thicker mica similar in dimension to that of topographic contrast but almost nothing for the thinner mica sheet.

When we performed the spectroscopic measurement, we observed almost equal dissipation for bare Ir/Si and thin mica nanosheet (4-layer) measured separately, but higher in dissipation for the thicker mica sheets (11- and 15-layer) following sharp ordinary parabolic behavior and a tendency to increase with respect to its thicknesses. By fitting our parabolic curve, we measured the contact potential value (CPD) for the corresponding surfaces which later been used to extract pure electrostatic ( $\Delta f_{\text{ele}}$ ) force interaction. From the dissipation ( $D_j$ ) and  $\Delta f_{\text{ele}}$  curves which are linear in characteristics for all layers, the surface resistance for Joule dissipation was measured and summarized as the order in  $\text{G}\Omega$ . We explained such a high resistance value for the metal and thin nanosheet is possibly due to surface charge scattering and dielectric loss under tip oscillation. The present work possibly paves the way for nanoscale mechanical and electrical characterization based on measurement of the energy dissipation via non-contact probing in the FM-AFM.

## Keywords:

1. Frequency modulated atomic force microscopy (FM-AFM), 2. Phlogopite mica, 3. Polyurethane hand roller, 4. Charge scattering, 5. Energy dissipation.

## **Acknowledgments**

Firstly, I wish to express my deep gratitude to my supervisor Prof. Masahiko Tomitori, Graduate School of Advanced Science and Technology, Japan Advanced Institute of Science and Technology, for providing me the opportunity to be his student. His kind guidance, encouragement, constructive criticism, and suggestions contributed to the necessary inspiration in the completion of this work. His utmost faith in me was the prime source of motivation for me to stay focused during the entire time of research and preparation of this thesis.

I would like to express my deep thanks to the internal committee members Professor Yoshifumi Oshima, Professor Yukiko Takamura, and Professor Toshu An, School of Materials Science at JAIST, and my special thanks to Professor Takashi Ichii, the University of Kyoto as an external committee.

I would like to express my deep thanks to my laboratory members and research group under Professor Toyoko Arai and Professor Yoshifumi Oshima.

Finally, I express my heartfelt gratitude to my parents and my little brother, for their positivity, relentless support, and encouragement in difficult times. I would like to dedicate this work to my parents, who have always believed in me and my dreams. Their faith makes me stronger every time and fuels my passion to dream big.

Hasan Md Mahamudul

Tomitori lab, School of materials science, JAIST

Ishikawa, Japan

## **Table of Contents**

<b>Abstract .....</b>	<b>I</b>
-----------------------	----------

<b>Acknowledgments .....</b>	<b>III</b>
------------------------------	------------

<b>Chapter 1: .....</b>	<b>1</b>
-------------------------	----------

<b>Introduction:.....</b>	<b>1</b>
---------------------------	----------

1.1 Historical Overview:.....	1
-------------------------------	---

1.2 Early Achievements of nc-AFM:.....	3
--	---

1.3 Present Condition of FM-AFM: .....	4
--	---

1.3.1 Atomic Manipulation at Near Contact Region:.....	5
--	---

1.3.2 Capacitive Force Interaction in Nanoscale Materials: .....	7
--	---

1.3.3 Contact Potential Difference (CPD):.....	12
--	----

1.4 Purpose of the Study: .....	16
---------------------------------	----

1.5 Two-Dimensional (2D) Materials:.....	17
--	----

1.6 Nanoscale Energy Dissipation: .....	21
---	----

1.6.1 Adhesion Hysteresis Dissipation:.....	22
---	----

1.6.2 Joule Heat Energy Dissipation: .....	24
--	----

1.7 Concluding Remarks: .....	27
-------------------------------	----

1.8 Remaining Chapter Summary:.....	27
-------------------------------------	----

<b>References:.....</b>	<b>30</b>
-------------------------	-----------

<b>Chapter 2: .....</b>	<b>35</b>
-------------------------	-----------



## **Background and Principle of AFM..... 35**

2.1 Instrumentation with Fundamental Contact AFM Mode:.....	35
2.1.1 Imaging with Contact AFM: .....	38
2.2 Noncontact AFM Mode: .....	39
2.2.1 Principles and Operation of AM-AFM: .....	40
2.2.2 Principles and Operation of FM-AFM: .....	44
2.3 Cantilever Specifications: .....	54
2.4 Additional Apparatus: .....	56
2.4.1 Optical Microscope: .....	56
2.4.2 DC Magnetron Sputter (E-1030):.....	57

## **References:..... 60**

## **Chapter 3: ..... 61**

### **Experimental Methods for Sample Preparation and**

### **Evaluation ..... 61**

3.1 Introduction.....	61
3.2 Mechanical Exfoliation: .....	64
3.2.1 Experimental Methods to Prepare Large Area High-Quality Mica Nanosheet: .....	64
3.3 Results and Discussion: .....	69
3.4 Summary: .....	78

## **References:..... 79**

<b>Chapter 4: Evaluation of Mechanical Energy Dissipation using Frequency Modulation Atomic Force Microscopy.....</b>	<b>83</b>
4.1 Introduction:.....	83
4.2 Experimental:.....	85
4.3 Results and Discussion: .....	91
4.4 Conclusions:.....	106
<b>Chapter 5: Summarization and Future Prospects.....</b>	<b>114</b>
5.1 Summary:.....	114
5.2 Future Prospect: .....	115
5.3 Probable Application: .....	116
<b>Scientific Contributions: .....</b>	<b>116</b>

# Chapter 1:

## Introduction:

To draw the crucial information of nanomaterials, surface nanoscale imaging and characterization is a prerequisite that became available after the invention of atomic force microscopy (AFM) for both conducting and nonconducting surfaces. In this chapter, we will discuss the historical overview, classification of AFM, early and recent achievements and developments, purpose of the study, and finally, the most demanded topics related to AFM.

## 1.1 Historical Overview:

After the invention of the scanning tunneling microscope (STM) [1] in 1982, immediate acceleration had been taken place in surface science related to topography showing atom-resolved images with unique properties at an atomic scale for different materials. As a result, 2-dimensional (2D) materials and thin films gradually began to reveal their three-dimensional beauty to the visible world. However, STM is only limited to conductive materials as tunneling current ( $I_t$ ) is the only signal parameter to keep the tip-sample distance constant. But for device fabrication and biological cell characterization, a similar type of scanning technique was required that can simultaneously work both for insulators, semiconductors, and on the biological samples. Upon realization, in 1986 G. Binnig et al. first introduced atomic force microscopy (AFM) [2] capable of being scanning sample surfaces through raster scanning varying from conductive to insulator materials, alternatively known as contact or static AFM system. Using this AFM, the same group managed to perform scanning on graphite samples and thereof lattice images [3]. Depending on the satisfactory results from graphite and also by introducing frictional force microscopy by Mate et al. [4] speculated that AFM can measure the atomic periodicity even under ambient conditions. Several groups then imaged various samples i.e. the lattice image of NaCl (001) in ultra-high vacuum [5], the molecular structure of the Langmuir-Blodgett (LB) film [6], lattices of DL-leucine crystal, and so on. In the meanwhile, by adding a lateral-force microscope (LFM) with AFM (AFM/LFM), Fujisawa et. al. [7] showed that lattice periodicity can be thought of as a two-dimensional phenomenon. All those measurements

established contact AFM (Fig. 1.1a) as an attractive tool to measure topography, roughness, frictional images, and atomic periodicity on several sample surfaces.

Although contact AFM primarily succeeded in imaging atomic periodicity for various sample surfaces in UHV or ambient conditions, it also initially failed to measure surface defects which is a prerequisite for understanding the surface reconstruction phenomenon. Moreover, an atomic stick-slip process [4,8] causes additional energy dissipation [9] due to friction between tip and sample. Besides, high loading force on the cantilever sometimes causes plastic deformation of the crystal surfaces [10]. Such obstacles accumulated the further development of the AFM system.

Consequently, noncontact (or dynamic) AFM (nc-AFM/d-AFM) has been realized around 1987 [11] where a cantilever along with a sharp monolithic probe ( Fig. 1.1b) is attached at the end, can oscillate at its resonance frequency ( $f_0$ ) near the sample surface. The interaction forces act between the tip and sample surface maintains a constant distance using a feedback circuit when the tip scan across the sample. Hence, nc-AFM became famous due to preserving the tip and sample surface property for a long time even for rough surfaces, and a great reduction of loading force on the cantilever.

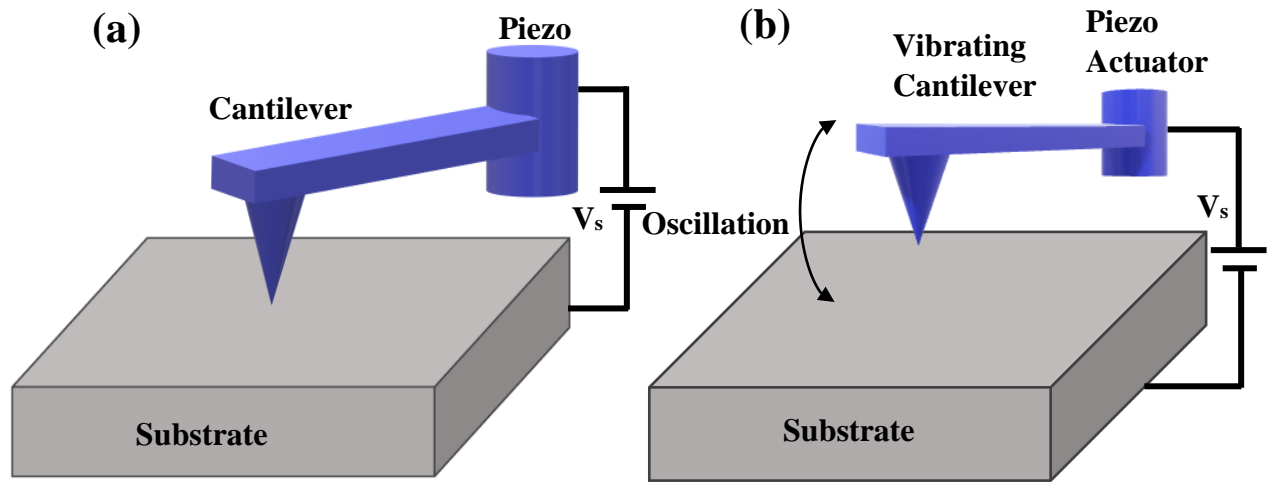


**Figure 1.1:** (a) Contact atomic force microscopy where tip scan across the sample surface under some loading force applied on the cantilever, (b) vibrating cantilever of an FM-AFM that scans across the sample surface under tip-sample force interaction phenomenon.

## 1.2 Early Achievements of nc-AFM:

From the beginning to till now, nc-AFM routinely manifests its excellent performances for several materials down to nanometer scale. By measuring the unambiguous forces acting between tip and sample, the problems mentioned before gradually started being resolved for a great reduction of lateral frictional force, defect or vacancies detection, and minimization of energy dissipation. In 1990, T.R. Albrecht et al. [12] introduced frequency modulation atomic force microscopy (FM-AFM) a special mode of nc-AFM that utilizes the resonance frequency shift ( $\Delta f$ ) of a cantilever for force/force gradient detection of a tip-sample system. Under this method, a sharp tip can sense the interaction forces acted in the tip-sample gap, thereby considered as a force sensor. Precise regulation of the force gradient then can keep the tip-sample distance constant. F. J. Giessibl [13] acquired an atomically resolved image on Si(111)-(7 $\times$ 7) reconstructed surface using FM-AFM in UHV at room temperature in 1995. Additionally, he established the idea of the tip apex change (i.e., from multi-tip to mono-tip conversion) and tip apex contamination during a large scanning area over the sample surface. Kitamura and Iwatsuki [14] also did similar imaging using the FM-AFM on the same sample, focusing on the proper adjustment of force gradient for the scanning stability and also anticipated a sensitive FM demodulator i.e. the so-called phase lock loop (PLL) for the improvement of the image contrast. Even though they used the same Si(111)-(7 $\times$ 7) reconstructed sample for imaging the surface with the newly developed FM-AFM, the images were not clear enough to compare with that of STM images, however, the great achievements were to initiate the atomic imaging with recognizing atomic defects and some future improvements by mentioning the problems related to at those FM-AFM experiments. In the same year, an atomically resolved well-contrasted image of InP (110) compound semiconductor had been published by Ueyama et al. [15] using UHV-FM-AFM at low temperatures. Within five months, Sugawara et al. [16] imaged the atomic point defects on InP (110) at room temperature using nc-AFM. They also observed the vacancies movement under tip oscillation conditions.

In 1997, finally, the true atomic resolution of Si(111)-(7 $\times$ 7) reconstructed surface had been revealed by Uchihashi et al. [17] and showed a correlation between AFM topographic images and spectroscopic behavior (i.e. force vs distance curve). Two types of topographic images (Fig. 1.2 (a) and (b)) appeared which were described by the continuity and discontinuity of force gradient curve between tip and sample as a function of distance. The corresponding rapidly changes physical

bonding to chemical bonding interactions between tip-sample refer to the discontinuity and a comparatively brighter topographic image appeared (Fig. 1.2 (b)). On the other hand, continuity means a weak van der Waals and/or electrostatic force is dominant for imaging showing less contrast (Fig. 1.2 (a)) than Fig. 1.2(b).

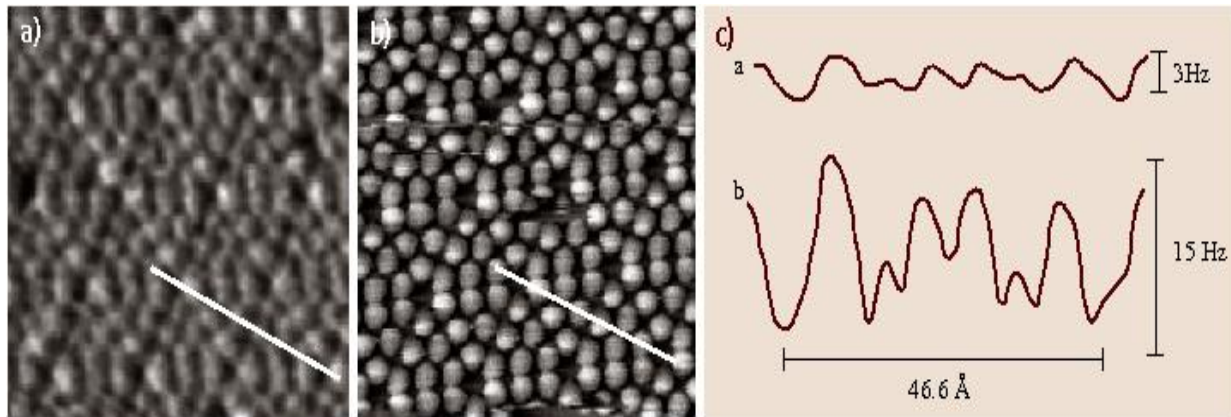


**Figure 1.2:** Nc-AFM image of Si(111)-(7×7) reconstructed surface (a) without (b) with discontinuity for a scan area of 9.9 x 9.9 nm<sup>2</sup>. The average  $\Delta f$  was -1.1 Hz for imaging. (c) corresponding line profile along 7x7 unit cell displayed in (a) and (b). Fig. adopted from [17].

Using a conductive Si cantilever ( $f = 172$  kHz,  $A = 14.8$  nm,  $Q = 38000$ ) their imaging of Si(111)-(7×7) surface revealed original atomic rearrangement under UHV condition and at the same time yielded a clear indication about the ability of FM-AFM and its upcoming bright future where the surface morphology of materials greatly depends on.

### 1.3 Present Condition of FM-AFM:

In the last three decades, AFM has already crossed its limit beyond topography and continuously used to investigate the surface nanoscale properties of various exotic materials. Accordingly, the electrical and mechanical characteristics (resistance [18], capacitance [19], tunneling current [20,21], force [22,23], energy dissipation [9,24,25], atomic manipulation [26], etc.) have been intensively investigated using FM-AFM provided specially resolved topography and crucial properties that should further take into consideration before fabricating the nanoscale devices.

Moreover, FM-AFM extends its applicability from UHV to a liquid and ambient conditions which is a basic requirement for the biological and chemical substrates [27–30]. In this section, we will shortly summarize the recent advancement, achievement, and unresolved phenomenon of well-developed FM-AFM.

### **1.3.1 Atomic Manipulation at Near Contact Region:**

The atomic manipulation concept has been introduced to modern nanodevices after the invention of STM [1]. Through STM, by using sample bias voltage, single adatoms extraction and deposition could be made shown for Si(111)-(7×7) surfaces. By using electrostatic and chemical forces along with bias voltages, a specific adatom can be removed, attached with the tip, and again be redeposited to a specified position accumulated intense engineering for atomic manipulation [31–33] at room temperature. However, this type of engineering was also required for nonconductive materials for many device fabrications offered nc-AFM to be utilized. Sugawara et al. [34] investigated atomic manipulation and artifacts on semiconductive Si(111)-(7×7) surface at low temperature. They succeeded in vertical adatoms manipulation by applying a sample bias voltage between conductive tip and sample surface for the first time using the nc-AFM technique. They analyzed the center and corner adatoms by considering others as artifacts. However, their experimental analysis also required sample bias voltage which leads to a similar type but a new experiment done by N. Oyabu et al. [26] in 2003. With a little modification of nc-AFM to near contact AFM mechanism, several short-range forces become dominant for scanning between tip apex and the sample surface. These short-range forces can be used for the soft nanoindentation process. N. Oyabu et al. showed that without using any voltage pulse or sample bias voltage soft nanoindentation process can lead to atomic manipulation which is completely a mechanical process. They choose Si(111)-(7×7) sample and observe the atomic manipulation for the center and corner atoms shown in Fig. 1.3. An adatom removal by using a soft indentation process from the corner and center (Fig 1.3 (b) and (c)) has been shown on the topographic images resulting in permanent vacancies in those relative positions. The initial positions are indicated with a circle mark. Such vacancies create meaning that at least three covalent bonds break to remove one Si adatom. Also, this soft nanoindentation can be applied to deposit adatom at the created vacancies positions shown in Fig 1.4.

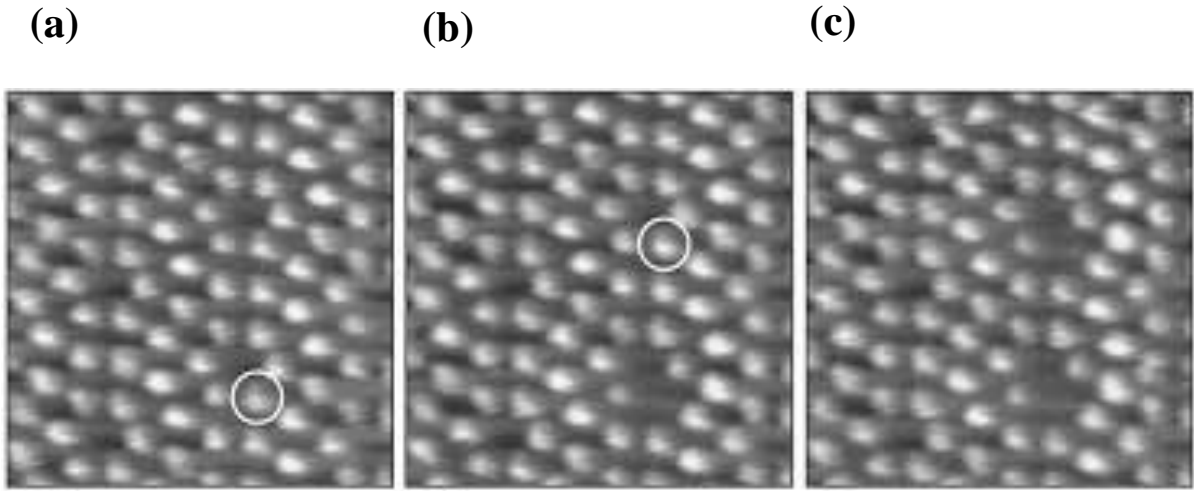


**Figure 1.3:** Two mechanical single-atom manipulation processes from (b) corner, (c) center. (a) represents the initial positions of adatoms on Si(111)-(7×7) surface. The scan area corresponds to 6.6 x 6.6 nm<sup>2</sup>. N-doped Si cantilever used the amplitude  $A = 66.5$  nm and spring constant  $k = 48$  N/m. Fig. adopted from [26].

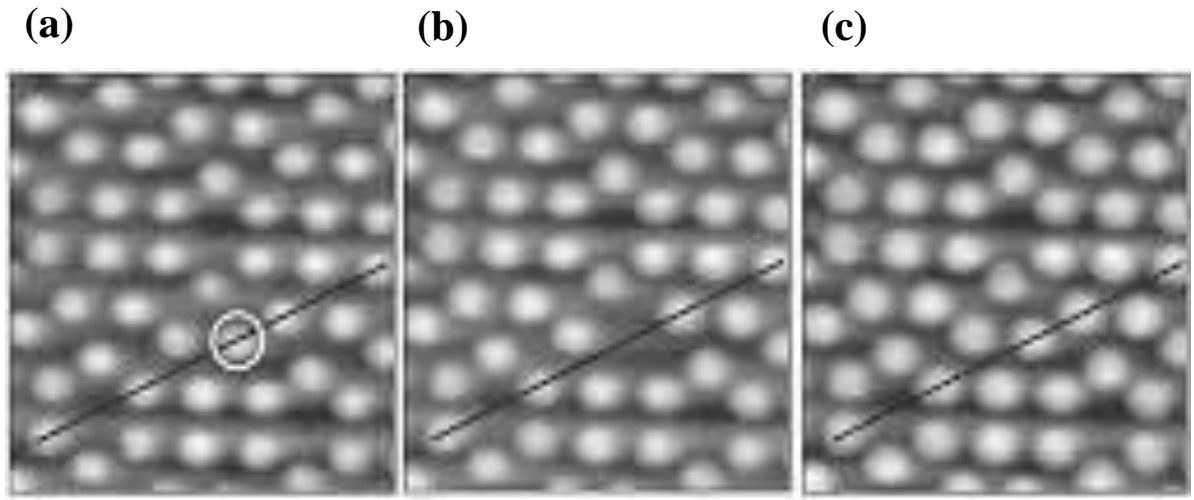


**Figure 1.4:** Soft nanoindentation used for (c) adatoms deposition, (a) marked adatoms that have been indented to create vacancies in (b). Fig. adopted from [26].

Therefore, nc-AFM shows its ability for atom manipulation process that overcome long-standing STM problem only for conductive materials. It is expected that near future various dielectric 2D materials will also be investigated using this mechanical atom manipulation technique revealing enhanced mechanical engineering with defined structures on materials surfaces at the nanoscale.



### 1.3.2 Capacitive Force Interaction in Nanoscale Materials:

When an atomically sharp tip, supported by a long cantilever vibrates near the sample surface using damped harmonic oscillation property [35], the scanning mechanism is controlled by several complex long and short-range interaction forces, categorized as long-range electrostatic force ( $F_{ele}$ ), long-range van der Waals force ( $F_{vdW}$ ), short-range chemical bonding force ( $F_{bond}$ ), short-range repulsive force ( $F_{rep}$ ), short-range adhesive force ( $F_{ads}$ ), etc. Distinguishing between these forces from one another is a quite complicated task both theoretically and experimentally. Typically, various analytical and numerical as well as indirect experimental technique (depending on  $\Delta f(d)$  curve) is used for both detection and distinction between metal/metal or metal/semiconductor tip-sample forces.

Among those methods, a frequent and versatile approach to measuring the electrostatic force ( $F_{ele}$ ) is to modulate the tip-sample force field by an ac-bias voltage ( $V_{ac}$ ). It is convenient to follow this method by assuming the tip-sample system with a parallel plate capacitor where one of the two plates has been replaced by an axially symmetric tip perpendicular to the sample surface. Then the tip will experience an electrostatic force under a bias voltage which is proportional to the capacitance gradient and the relationship can be demonstrated based on capacitor potential energy equation [36] i.e.  $U = 1/2CV^2$ . Therefore, the force becomes-

$$F_{ele} = -\frac{dU}{dr} \quad (1)$$

$$F_{ele} = \frac{1}{2} \frac{\partial C}{\partial r} V^2 + CV \frac{\partial V}{\partial r} \quad (2)$$

Where  $C$  is the capacitance and  $V$  is the applied bias voltage. By considering only the vertical ( $z$ -axis) force contribution equation becomes-

$$F_{ele} = \frac{1}{2} \frac{\partial C}{\partial z} V^2 \quad (3)$$

Under a bias voltage, this separation-dependent capacitance is always present in the tip-sample circuitry system and can affect the forces considered as capacitive coupling forces [19]. Two

dedicated spectroscopic force fields have been developed depending on this force known as electrostatic force microscopy (EFM) and Kelvin probe force microscopy (KPFM) [37], respectively. Now, let's consider that a modulation ac-bias at a frequency  $\omega_{ac}$  with a dc offset [ $V_{dc} + V_{ac} \sin(\omega_{ac}t)$ ] has been applied to the tip-sample system. Therefore, the above equation becomes –

$$F_{ele} = \frac{1}{2} \frac{\partial C}{\partial Z} [V_{dc} + V_{ac} \sin(\omega_{ac}t) - V_{CPD}]^2 \quad (4)$$

Where  $V_{CPD}$  corresponds to the contact potential difference (CPD) between tip and sample. This CPD is directly related to the work function of the tip and sample and can be written as –

$$V_{CPD} = \frac{\phi_{sample} - \phi_{tip}}{e} \quad (5)$$

By solving the equation (4), we can get the force components [37] –

$$\left. \begin{aligned} F_{dc} &= \frac{\partial C}{\partial Z} \left[ \frac{1}{2} (V_{dc} - V_{CPD})^2 + \frac{V_{ac}^2}{4} \right] \\ F_{\omega_{ac}} &= \frac{\partial C}{\partial Z} (V_{dc} - V_{CPD}) V_{ac} \sin(\omega_{ac}t) \\ F_{2\omega_{ac}} &= -\frac{\partial C}{\partial Z} \frac{V_{ac}^2}{4} \cos(2\omega_{ac}t) \end{aligned} \right\} \quad (\text{a, b, c})$$

Here,  $F_{dc}$  represents a dc force contribution influencing the topography,  $F_{\omega_{ac}}$  is the modulation bias to measure the CPD and  $F_{2\omega_{ac}}$  is used for capacitance microscopy i.e.,  $F_{ele} = F_{dc} + F_{\omega_{ac}} + F_{2\omega_{ac}}$ . Besides, capacitive force interaction between a metallic tip and sample with analytical description can be found in S. Hudlet et al [38]. Their proposed model allows us not only to measure the force determination, but also to discuss the contribution of tip apex, truncated conic-contribution, and tip-sample distance. According to their model, the force between a metallic tip and metallic surface is given by the following equation –

$$F_z = \pi\epsilon_0 \left[ \frac{R^2}{z(z+R)} \right] V^2 \quad (6)$$

where  $R$  is the tip radius and  $z$  is the tip-sample distance. Surprisingly, their proposed model and the exact one put good agreement shown in figure 1.5 (a) and (b) with a maximum error of 5% depending on the tip-sample distances.

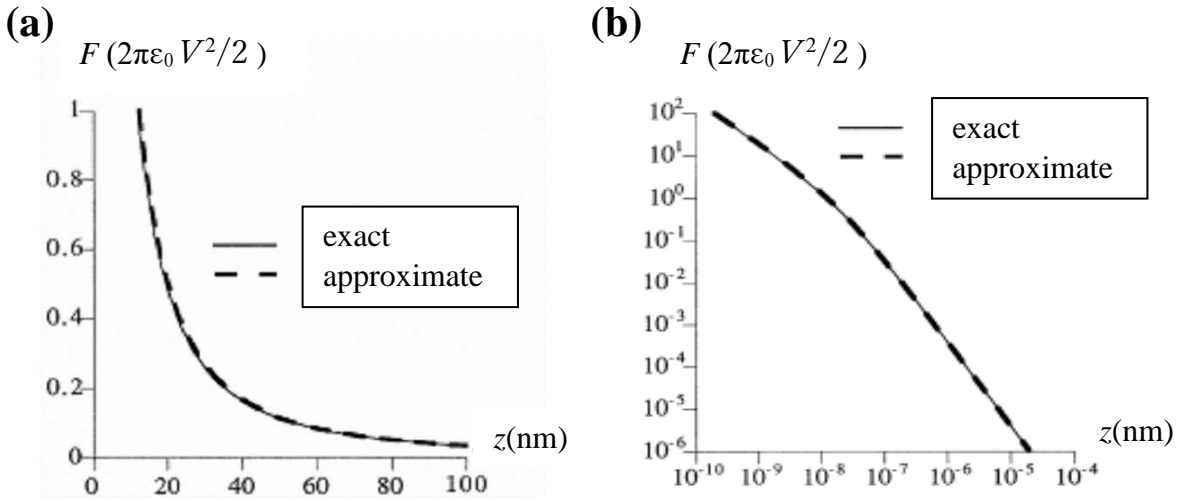


**Figure 1.5:** Variation of force with distances for exact and approximate model (a)  $0 < z < 100$  nm and (b)  $10^{-10} \text{ m} < z < 10^{-4} \text{ m}$ . Data taken from [38].

However, for metallic tip and semiconductor sample, we have taken into consideration of space charge layer (SCL) for the semiconductor surface. In the case of semiconductor surface, the force can be written as [39] –

$$F_\omega = -\frac{Q_s}{\epsilon_0} \frac{C_I C_D}{C_I + C_D} V_{ac} \sin(\omega_{ac} t) \quad (7)$$

where  $Q_s$  are the charges on the semiconductor surface,  $C_I$  and  $C_D$  are the capacitances due to the air gap and SCL, and  $\epsilon_0$  is the dielectric constant. Also, for this case variation of force is not as simple as that of metal/metal case. Therefore, the capacitance which depends on the applied bias polarity can be considered as passive and non-passive capacitance [39]. By using this capacitive model, T. Arai et. al. [18] showed a relationship between  $\Delta f$  and energy dissipation.

Recently, Umeda et al. [40] used the apex and conical contribution of the tip towards capacitance derived by Hudlet et al. [38] and also calculate the additional cantilever contribution to find the total capacitive contribution inside a liquid media. Their results showed that under low modulation frequency the cantilever deflection is mostly dominated by the surface stress whereas under high-frequency modulation electrostatic force is dominant inside polar liquid media.

Electrostatic interaction between a conductive tip and a dielectric slab has been investigated analytically and numerically by Ali Sadeghi et al. [41] and also corrected Hudlet's model for the case of a moderate tip-sample separation. Working with a dielectric sample affixed on a conductive coated layer normal (back electrode) to the tip (front electrode) is much more complicated due to the partial penetration of the electric field inside the dielectric sample (Fig. 1.6a). As there is no direct solution to this problem, we use the image charge method for a sphere and a plane and their combined effect to solve this conductive sphere-dielectric (Fig 1.6b and c) problem.

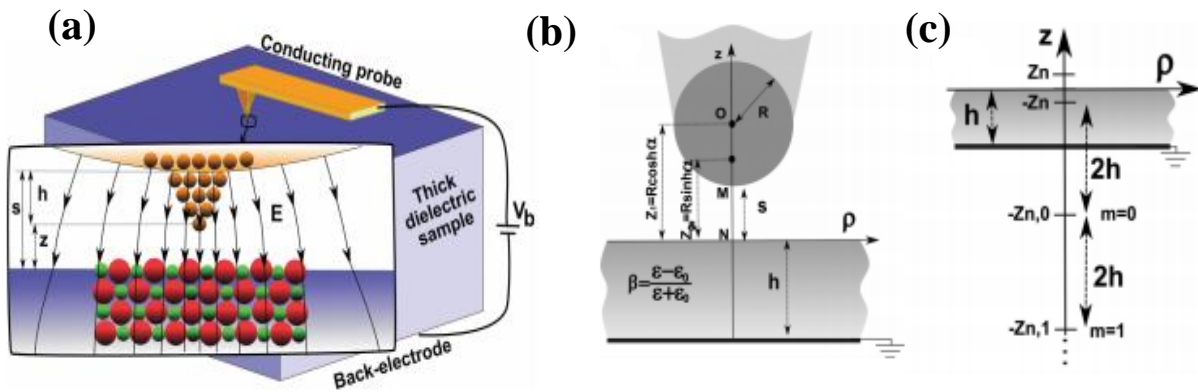


**Figure 1.6:** (a) Macroscopic and microscopic view of AFM tip pointed perpendicular to a dielectric sample [42]; (b) 2-dimensional representation of conductive spherical tip with radius  $R$ , separate by a distance  $s$  from a dielectric sample having relative permittivity  $\epsilon$  and  $\epsilon_0$ . The relative width of the

slab is h. (c) relative image charges due to a point charge at  $z_n$  along the vertical axis [41]. The images are collected from referred papers.

When a sphere is placed perpendicular to a dielectric sample (Fig 1.6b), placing a charge  $q_1 = 4\pi\epsilon_0 RV$  at  $z_1 = R + s$  (where  $R$  is the tip radius and  $s$  is the separation distance between tip and sample) will make the sphere surface equipotential at  $V$ . Due to this an image  $-\beta q_1$  at  $-z_1$  will appear inside the dielectric, eventually, modify the potential of the sphere surface. Therefore, a second charge  $q_2 = \beta q_1 R / 2z_1$  will appear at  $z_2 = z_1 - R^2 / 2z_1$  to make the sphere surface potential back to  $V$  results in the second image inside the dielectric and this chain process will be continued until  $s \rightarrow 0$ . Approximate compact expressions depend on charges inside the sphere and its image inside the dielectric slab. If the point charges inside the sphere are –

$$\begin{aligned} q_1 &= 4\pi\epsilon_0 RV & q_{n+1} &= \frac{\beta q_n R}{z_1 + z_n} \\ z_1 &= R + s & z_{n+1} &= z_1 - \frac{R^2}{z_1 + z_n} \end{aligned} \quad (8)$$

Then the images  $\{-\beta q_n, -z_n\}$  will be created inside the dielectric to satisfy the boundary condition. The second-order homogenous difference equation of (8) is there –

$$\frac{1}{q_n} = \left( \frac{2 \cosh \alpha}{\beta} \right) \left( \frac{1}{q_{n-1}} \right) - \left( \frac{1}{\beta^2} \right) \frac{1}{q_{n-2}} \quad \text{where } \cosh \alpha = 1 + s/R$$

The solution of this equation can be expressed as a linear combination of  $\exp(\pm n\alpha)$  as –

$$\begin{aligned} q_n &= q_1 \sinh \alpha \times \frac{\beta^{n-1}}{\sinh n\alpha} \\ z_n &= R \sinh \alpha \times \coth n\alpha \end{aligned} \quad (9)$$

Using these solutions an approximate capacitance term can be found by taking into consideration of the corresponding correction term for tip truncation. i.e.

$$C^{(1)} - C_{sph} \cong 2\pi\epsilon_0 R \left( \frac{\beta/(1 - \beta e^{-\alpha})}{\cosh \alpha} \right) \quad (10)$$

$$C^{(2)} - C_{sph} \cong 2\pi\epsilon_0 R \left( \frac{\beta}{\cosh \alpha} + \frac{(\beta^2/(1 - \beta e^{-\alpha}))}{4\cosh^2 \alpha - 1} \right)$$

Finally, adding a missing constant term ( $C_{sph}$ ) they showed that Hudlet's approximation is remarkably true for a moderate tip-sample separation put the corrected capacitance term as follows –

$$C - C_{sph} = 2\pi\epsilon_0 R \ln \left( 1 + \frac{R}{s} \right) \quad (11)$$

Here, equation (11) corresponds to the exact solution for a metallic tip-sample system whereas equation (10) is useful for theoretical modeling on insulating samples.

### 1.3.3 Contact Potential Difference (CPD):

In FM-AFM contact potential difference (CPD) between a conductive probe and sample is a characteristic parameter through which long-range electrostatic and van der Waals forces can be separated. As mentioned before CPD is related to the work function of tip ( $\phi_{tip}$ ) and sample ( $\phi_{sample}$ ) can be written as  $V_{CPD} = (\phi_{sample} \pm \phi_{tip})$ . The  $\pm$  sign represents whether the bias is applied to the tip or the sample. By monitoring the capacitive electrostatic force ( $F_{ele}$ ) modulated by an ac-bias having frequency ( $\omega_{ac}$ ) concurrently with a dc bias to compensate that  $F_{ele}$ , we can measure the CPD. It is a convenient way to separate the electrostatic force from van der Waals forces when the tip-sample interacts with each other through complex force interactions ( $F_{ts}$ ). A more detailed way to realize the CPD is to analyze the Fermi level of two different materials. Under close separation ( $s < R$ ), an electrical force is generated due to the difference in their corresponding Fermi levels shown in Fig. 1.7.

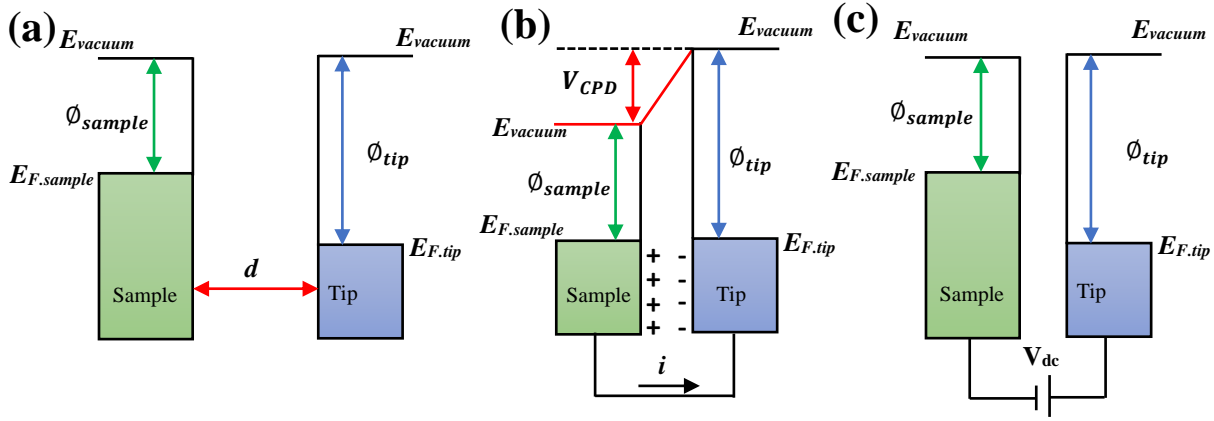


**Figure 1.7:** Energy level comparison (a) no interaction, no electrical connection; (b) tip-sample is in electrical contact; (c) dc bias compensated nullified close tip-sample separation. Fig. concepts taken from [37].

From Fig. 1.7(a), a difference in Fermi level has appeared due to the separation between tip and sample as well as no electrical back connection. However, when the tip and sample will be close enough where interaction may happen or the near-contact region where tunneling may appear, Fermi levels will be lined up at the steady-state. Under this situation by connecting the electrode using a wire, the Fermi level will be aligned with each other through electron flow shown in Fig. 1.7(b). Upon leveling the Fermi level, tip and sample surface will be charged, and an apparent  $V_{CPD}$  will form by letting a detuning at the vacuum level introducing  $V_{CPD}$ . Now if we apply a dc-bias voltage ( $V_{dc}$ ) with the same magnitude as  $V_{CPD}$  has, then this apparent  $V_{CPD}$  will be nullified, and the remaining interaction will be long-range van der Waals interaction (Fig. 1.7c). This technique is very famous and measured almost for all FM-AFM measurements and a principle key factor for KPFM. In high-resolution KPFM, local CPD or (L-CPD) has been mapped by utilizing the short-range interaction phenomenon.

Under FM-AFM measurements, the most convenient way to measure the CPD is to take the  $\Delta f$ -bias curve which is originally an FM-AFM spectroscopic measurement. A nice parabolic behavior appeared depending on the separation between tip and sample as satisfied Eq. 4a. M. Guggisberg et al. [43] measured the separation-dependent interactions and discussed the long-range electrostatic, van der Waals, and also short-range chemical interactions. Through their work, they presented a systematic way to separate the complex force interaction between tip and sample. Similarly, T. Arai

et al. [18] also measured  $\Delta f$  – sample bias simultaneously with the dissipation vs bias curve. Their results are shown in Fig. 1.8. From the maxima of this parabolic curve, we can get an idea of  $V_{CPD}$  of the specified position where the tip oscillated.

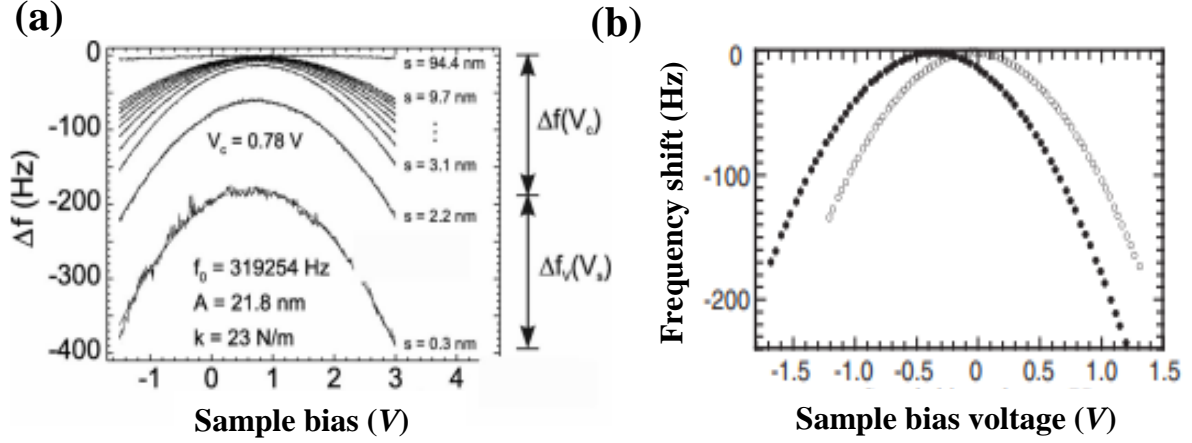


**Figure 1.8:** (a)  $\Delta f$  – sample bias curve for several distances keep a fixed CPD as  $V_{CPD} = -0.78$  V for a clean Cu (111) sample and Si cantilever; (b) similar type of CPD measurement using with/without H terminated Si tip. The measured CPD has changed from  $-0.37$  V to  $-0.05$  V after H-termination. Fig. are adopted from [43] and [18].



However, to map the CPD we need KPFM measurement. Recently, Goryl et al. studied gold (Au) nanoparticles and mapped the topography and CPD simultaneously [44,45]. They grow Au on InSb (001) surface at 400K. Their results showed that the work function of grown Au was independent of the size of the Au nanostructure.

Surface potential differences between terrace and edges of UHV-cleaved semiconductor, alkali halides, and insulating materials have been mapped indicated very good results related to charged defects that were absent at their corresponding topography [46–48]. UHV-cleaved KCl has been studied briefly shown in Fig. 1.9 (a) and (b) [49]. A proper distinction in the potential image shows 0.7 eV larger work function over the rest of the surface terrace, considered as defects.

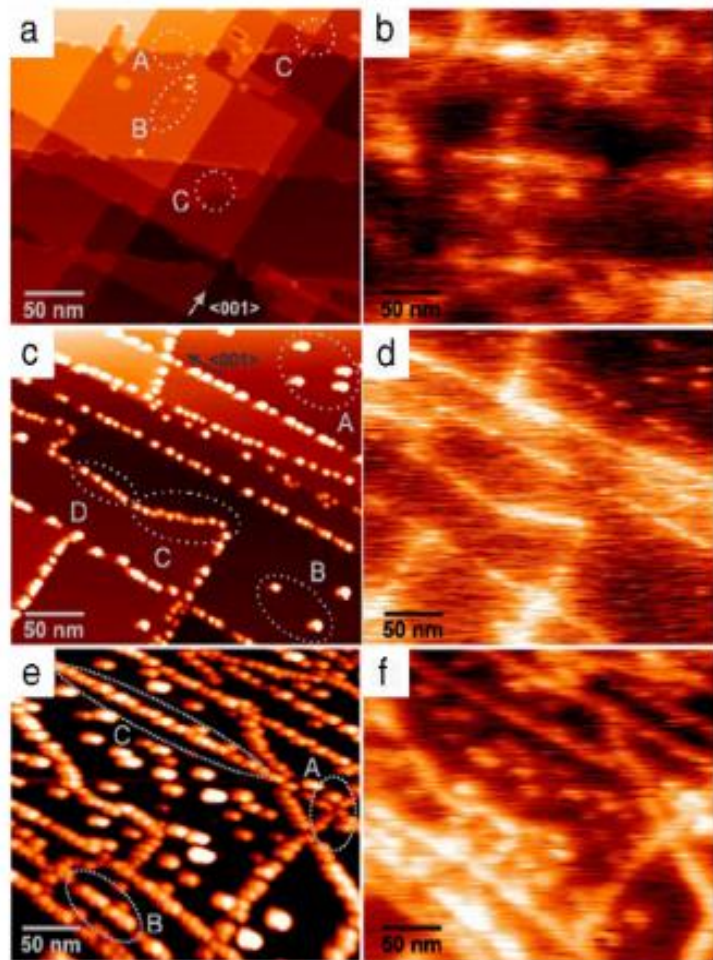


**Figure 1.9:** Simultaneous topography

(a), (c), (e), and CPD mapping (b), (d), (f) of UHV-cleaved KCl with deposited Au at different layer thickness. (a) and (d) for clean KCl (001); (c) and (d) for 0.04 ML Au-deposition at room temperature; (e) and (f) for 1.44 ML Au-deposition at 200 °C. Images taken from [49].

Fig. 1.9 (c) and 1.9 (d) represent the data for 0.04 ML Au deposition on KCl at room temperature and 1.9 (e), 1.9 (f) is for Au deposition at 200 °C. The homogeneous distribution of Au nanostructures over the terraces creates one-dimensional nanostructure growth. One significant result is that some of the Au nanostructures have a high work function than the others probably due to the charge transfer

phenomenon between defects to Au nanostructures. Therefore, KPFM CPD measurement can play an important role in nanomaterials characterization for future nanodevices.

## 1.4 Purpose of the Study:

The purpose of this present study lies in the characterization of the nanoscale mechanical and electronic properties, such as resonance frequency shift ( $\Delta f$ ) of an oscillating cantilever due to complex long- and short-range attractive tip-sample force interactions; routinely appear energy dissipation in non-contact for mechanical damping of the lever as well as the local surface electronic properties (resistance, capacitance) acts crucially between a nanotip and a substrate film in an FM-AFM system. Even though mechanical energy dissipation has been widely studied, it is neither fully understood nor fundamentally resolved demanding additional study on energy dissipation by considering the above-mentioned dynamic properties. Through our research work, we investigate the energy dissipation especially due to Joule heat and the associated resistance and capacitance functioning just underneath the oscillating probe under a sample bias voltage for a metallic tip and a metallic substrate partially covered with a dielectric flat nanosheet. With the presence of well-defined long-range electrostatic or van der Waals (vdW) interactions under biasing condition, the comprehensive  $\Delta f$ -bias curve along with simultaneous dissipation-bias curve acquired from spectroscopic window convey numerous nanoscale complicated information including energy dissipation that may vary for different materials owing to its local electronic surface properties. Therefore, to compare the differences in energy dissipation over an insulative material with respect to a conductive material, we mechanically exfoliate mica nanosheet varying from thin to thick layers and paste it on iridium (Ir)-coated n type-Si(111) substrate (Ir/Si); finally, we use a sharp conductive nanotip to complete the experimental frame for characterization. We discuss the energy dissipation experimentally for two different samples and thereof the origin of surface resistance with the help of surface charge scattering and dielectric energy loss of materials by providing a tip-sample model diagram. This is of great help to simplify the involved nanoscale phenomenon between the tip and the sample for our understanding of the properties and extending their applications.

## 1.5 Two-Dimensional (2D) Materials:

To fabricate future nanoscale electronic devices with distinctive functions, researchers are still searching for unique and most promising two-dimensional (2D) materials that can open a new arena for novel devices. The breakthrough happened after the invention of 2D graphene with a few atomic layers from a bulk graphite [50] which revealed non-identical characteristics than that of the bulk crystal. Therefore, materials that can run under some planar physical limits where remarkable electronic and mechanical properties being highlighted are defined as 2D materials. From the definition and concerning carrier concentration, it is clear that charge carriers are free to move in the  $X - Y$  plane by keeping restrictions along with its thickness. Through their unique and novel characteristics, 2D materials are still dominant over one-dimensional (1D) nanowires, zero-dimensional (0D) quantum dots (QD), and that of bulk 3D networks. Besides, active response to external stimuli, mechanical flexibility, optical transparency, etc. is noticeable features of 2D materials for electronic and optoelectronic devices. Since the continuous investigation of graphene provided unconventional features (such as large surface area [51], high Young's modulus [52], transparency [53], high thermal conductivity [54], ultra-high carrier concentration [50], Dirac cone structure [55], etc.) several 2D materials came into focus including insulators, semiconductors, and metals. Besides graphene, polymers, fibrous materials, ultra-thin glass plates, and metallic foils have also been investigated in the last decade. Among them, another briefly explored field is transition-metal dichalcogenides (TDMs) containing various 2D materials;  $\text{MoS}_2$ ,  $\text{MoSe}_2$ ,  $\text{WSe}_2$ ,  $\text{TiS}_2$ , etc. [56,57], hexagonal boron nitride (hBN) [58], metal oxides, and so on. In Fig. 1.10, a concise summary has been presented for 2D materials. Several exfoliation procedures including mechanical cleaving for layered materials [21,59,60], liquid-phase exfoliation [61], as well as chemical growth procedures, assure the availability of those 2D materials. In Fig. 1.11, mechanically exfoliated (Scotch Tape method)  $\text{MoS}_2$  varying from single to multilayer is shown which had been used field-effect transistor (FET) [60].

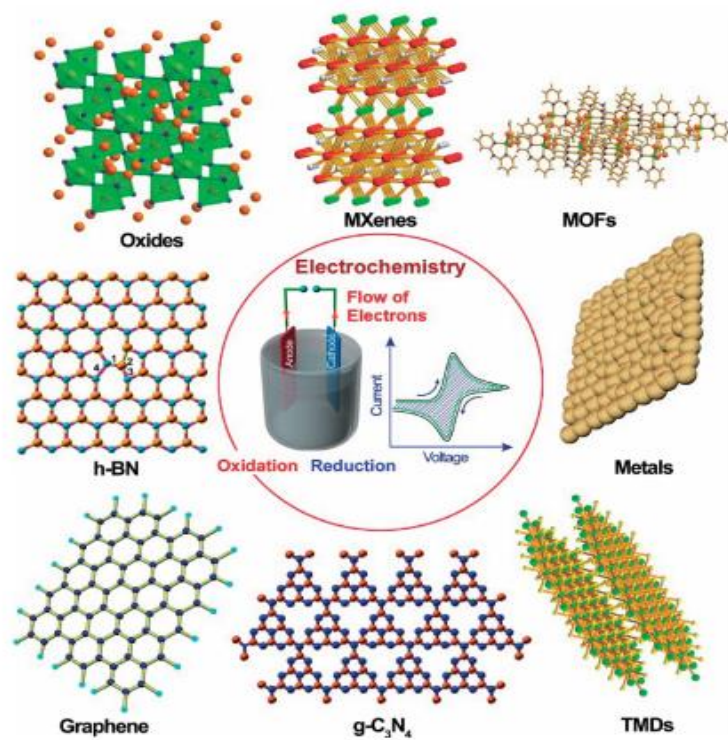


**Figure 1.10:** Schematic summary for 2D materials invented recently for future nanodevices. Image adapted from [62].

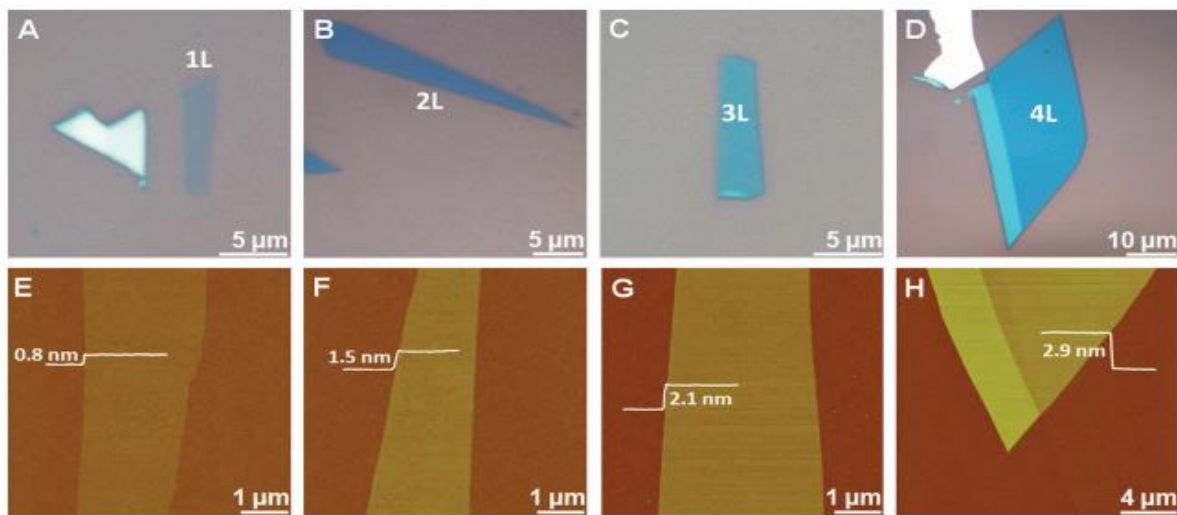


**Figure 1.11:** Mechanically exfoliated MoS<sub>2</sub> on Si/SiO<sub>2</sub> substrate. Optical image of (a) 1-layer, (b) 2-layer, (c) 3-layer, (d) 4-layer MoS<sub>2</sub>; (e-h) are the corresponding AFM images. Images taken from [60].



However, a new 2D platform that has been already taken the attention of many material scientists, thereof novelty, reliability, and precise outcomes as a result of tuned measurements is known as Micatronics [63]. The crystal structure of mica was revealed in the 1920s and was considered as layered 2D materials among phyllosilicates [64]. The unit cell representation of mica can be defined as  $X_2Y_nZ_8O_{20}(OH, F)_4$  where X stands for cations ( $K^+$ ,  $Na^+$ ,  $Ca^{2+}$ ), Y for octahedrally coordinated elements ( $Al^{3+}$ ,  $Mg^{2+}$ ,  $Fe^{2+}$ ,  $Li^+$ , etc.), and Z for tetrahedrally coordinated elements ( $Si^{4+}$ ,  $Al^{3+}$  and so on) [63]. Depending on the value of the base parameter  $n$ ; mica can be classified as muscovite ( $n = 4$ , dioctahedral) and phlogopite, biotite, zinnwaldite, etc. ( $n = 6$ , trioctahedral). Widely used 2D nanosheet of mica is commonly termed muscovite  $[KAl_2(Si_3Al)O_{10}(OH)_2]$ , biotite  $[K(Mg, Fe)_3(AlSi_3O_{10})(F, OH)_2]$ , and phlogopite  $[KMg_3(AlSi_3O_{10})(OH)_2]$ . As we already mentioned mica

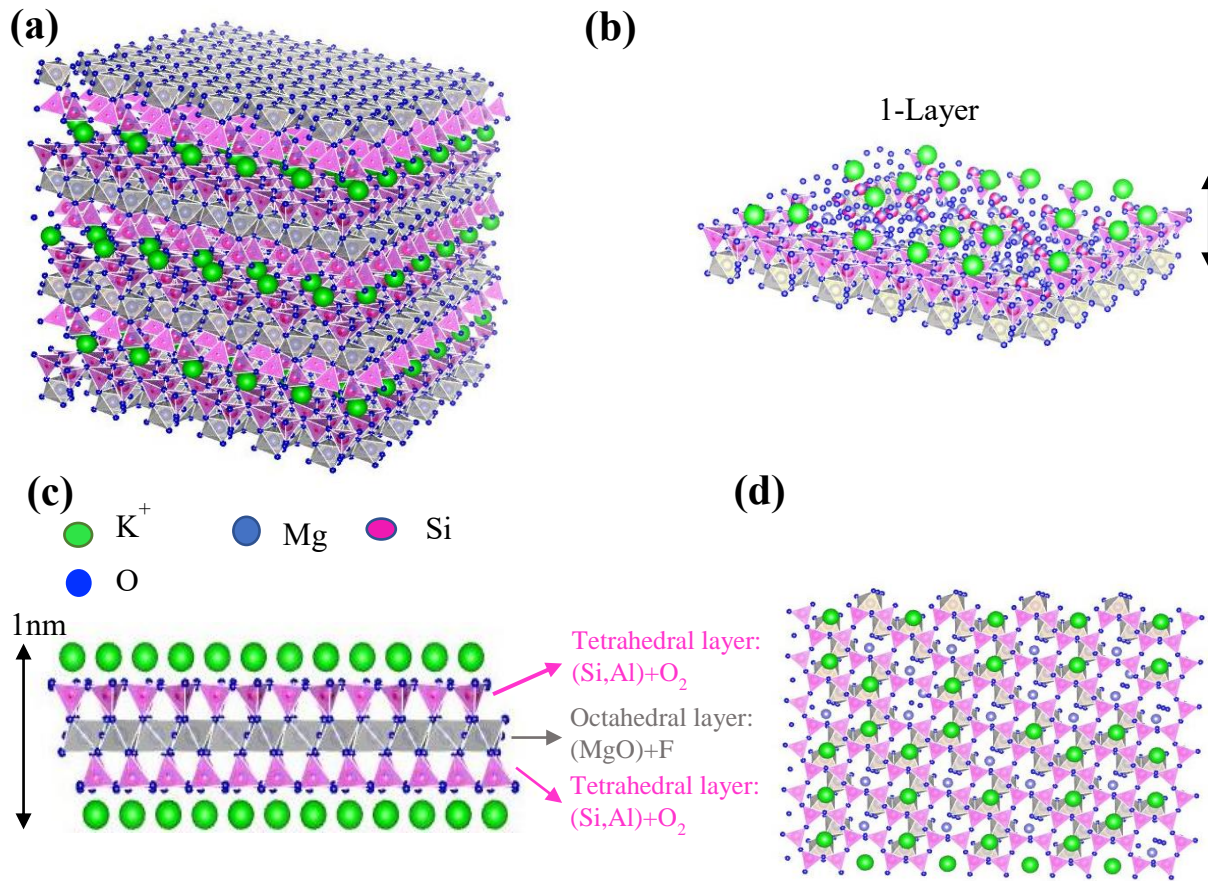


**Figure 1.12:** Crystal structure of phlogopite mica (a) 3D bulk view; (b) 3D 1-layer (1nm) nanosheet showing the only disturbed equally distributed  $K^+$  layer after cleavage; (c) side view of the sandwich layer,  $(Si, Al)O_2 / (MgO) + F / (Si, Al)O_2$ ; (d) top view (001) plane after exfoliation. Mica-3D representation has been performed by Author.

is a layered material, therefore, one layer ( $\sim 1$  nm) of mica nanosheet consists of two tetrahedra (T) sheets on either side of an octahedral (O) sheet through making a sandwich layer. In Fig. 1.12 (a) and (b), a three-dimensional representation of bulk and 1-layer has been represented. The interlayer  $K^+$  is indicated as green color which is used to make a bond between two T-O-T layers. Figure 1.12 (d) shows the basal (001) cleaved plane of the phlogopite mica surface with a hexagonal array pattern of  $SiO_4$  atoms. Cleaving along this basal plane or simply by breaking the vdW allow us to make large flat nanosheet of mica as a 2D materials with an equal number of  $K^+$  ion on both sides. Besides the following characteristics also make mica a potential independent field.

- i) 2D structure: Owing to its strong intra-layer and weak interlayer interaction, exfoliation can be possible that make mica a promising 2D material.
- ii) Transparency: Ultra-high transparency under ultraviolet-visible range exists for mica up to  $\sim 100\mu m$ , an important feature to make optoelectronic devices.
- iii) Elasticity: Due to high Young's modulus ( $Y \sim 200$  Gpa) mica is good to use as a dielectric material in highly demanding mechanical applications [65].
- iv) Flexibility: As reported the bending radius of  $\sim 100$  nm thick is 0.03 cm, mica still preserves its 2D properties under bending conditions [66].
- v) Chemically inert: The chemical inertness of mica is due to the absence of the dangling bond on the surface of the nanosheet. Besides, the nontoxic behavior is useful for biological nano-instrumentation.
- vi) Thermally conductive: Flexible device can accelerate heat energy dissipation on mica surface.
- vii) Electrical insulator: Recent use of mica as a substrate as well as a gate dielectric [66] in flexible devices make mica an electrical insulator. Besides, thin layer-by-layer conductivity has been reported by M.R. Islam et. al [21].

- viii) Thermal resistivity: The melting point of mica is varying from 1150 K – 1300 K [67] which models mica as high thermal resistive 2D material for nanodevices.
- ix) Availability: Mica is inexpensive and abundant in the earth's crust. Therefore, it is demandable at a low cost and friendly to the environment.
- x) Large atomic flat surface: Using mechanical exfoliation, it is possible to prepare an anatomically large flat terrace of mica [21], suitable to investigate under AFM, STM, or TEM.
- xi) Non-magnetic: Earth crust mica typically shows non-magnetic behavior where a very weak anisotropic ferromagnetism is possible by doping through Fe.
- xii) Biocompatibility and light-weight: Mica has a great influence on biological application [68] (artificial skin, muscles, prosthetic limbs, soft and humanoid robots, smart and electrical clothing, etc.).

Therefore, all those above properties conclude phlogopite mica a distinctive 2D material comparable to the other 2D materials introduced initially in this paragraph as well as in figure 10. Although it is extremely hard to exfoliate a thin layer (~10 nm) to ultra-thin (~1 nm) by using any hand-made mechanical exfoliation technique, featured characteristics that have already been confirmed, and discussed above reveal the successful platform of Micatronics.

## **1.6 Nanoscale Energy Dissipation:**

Macroscopic or atomic scale dissipation is an interesting phenomenon associated with the modern AFM system. While the conventional frictional stick-slip process is well-characterized as energy dissipation for contact AFM system [4,8], dissipation related to FM-AFM method neither fully understood nor identical is one of the newest featured topics related to the nc-AFM at present. In the contact AFM system, due to the development of a lateral force between the AFM tip and surface atoms during scanning, the tip sticks to the atomic sites and then slips to the relaxed position by spreading out energy spontaneously which is revealed as dissipation. A lateral force with a magnitude of 0.5 nN had been reported for alkali halide by E. Gnecco et al. [69]. Similar to the contact AFM

method, dissipation is also present in the newly developed FM-AFM technique which can be inferred from the spectroscopic analysis i.e., the excitation signal–distance curve with the  $\Delta f$ –distance curve simultaneously with dissipation mapping at a nearest tip-sample separation [9,24]. By analyzing the amount of energy needed to keep the vibrating amplitude constant of an FM-AFM cantilever, one can easily get information about the external atomic or macroscopic dissipation [13,15,18,70,71]. Note that, commercially available high-frequency monolithic force sensors allow us to neglect the intrinsic dissipation of the cantilever. However, FM-AFM dissipation has been classified into many categories such as adhesion hysteresis, Brownian particle dissipation mechanism, velocity-dependent dissipation, Joule heat energy dissipation, dissipation due to lattice vibration, and atomic instabilities, etc. [72]. Among those dissipations, Joule heat and adhesion type hysteresis dissipation is well understood and experimentally verified. Therefore, we will try to focus on nanoscale energy dissipation which may fall into those two categories.

### 1.6.1 Adhesion Hysteresis Dissipation:

One of the well-explained dissipation mechanisms related to dynamic AFM systems is the adhesion hysteresis dissipation which can be utilized from the conventional force-distance curve using AFM spectroscopic window [73–75]. The  $F_{ts}$  – distance curve shows two different characteristics path (Fig. 1.13) followed by the tip similar but not exactly matched with each other, is typically called adhesion hysteresis dissipation. According to Yoshizawa et al. [75], three special conditions should be considered to explain the mechanism consistent with experimental results. At first, the deformation time ( $\tau_D$ ) has to be approximately equal to the tip motion time ( $\tau_T$ ). Depending on the magnitude of this timescale, three possible cases exists i.e. –

- $\tau_D \gg \tau_T$  meaning that a solid-like tip-sample system; able to provide small hysteresis.
- $\tau_D \cong \tau_T$  meaning that hysteresis is dominant.
- $\tau_D \ll \tau_T$  meaning that a liquid-like tip-sample system; able to provide small hysteresis.



The second condition is related to the scanning stability i.e. the tip and sample surface should have the ability and proper time to go back to their original configuration after each oscillation cycle. The third condition is that the deformation would be local which will convey the atomic information.

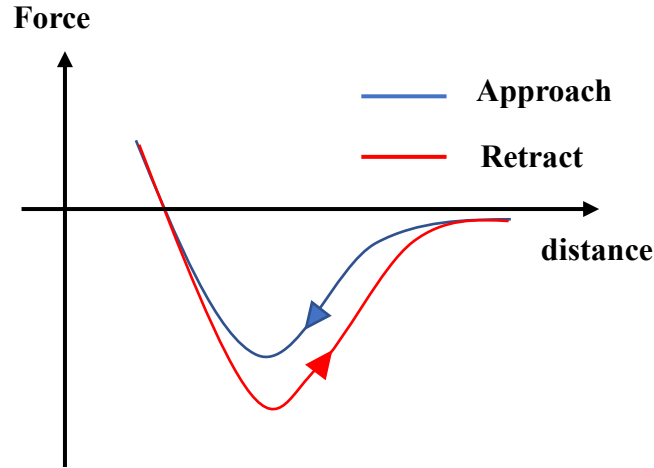


**Figure 1.13:** Schematic of adhesion hysteresis. The approach and retract force curve followed two different paths showing adhesion hysteresis dissipation mechanism.

If the tip-sample interaction is large enough or the distances even closer where real atomic contact between tip and sample may possible and if the sample surfaces consist of many atoms, the actual real adhesion hysteresis dissipation takes place shown in Fig. 1.13. However, such dissipation is known as macroscopic dissipation and does not reflect any atomic-scale phenomenon. But for a finite separation distance between tip and sample, reduced deformation of the tip allows us to measure force interaction only for the front atom of the tip and very few atoms on the sample side. This event results in dissipation in atomic-scale and provides nanoscale dissipation information. To visualize the dissipation phenomenon, we can consider the surface potential energy ( $E$ ) between tip and sample as a function of atomic positions ( $q$ ) for a finite set of tip positions ( $S$ ) [72]. If two local minima (A and B) exist in  $q$  and  $E$  then by considering the barrier heights ( $\Delta_{A \rightarrow B}$  and  $\Delta_{B \rightarrow A}$ ) we can summarize dissipation as follows (Fig. 14 a and b): In Fig. 1.14 (a), the barrier  $\Delta_{A \rightarrow B}$  is reducing with the decreasing distances between tip and sample and at the closest contact the atom can slide to second potential minima B from A. The energy will be lost as a phonon. Upon retraction, the barrier B is higher than A and the atom cannot return to its original position. Therefore, in this dissipation process,

some structural irreversible changes happen during scanning. This phenomenon is also mentioned by C. Loppacher et al. [71]. However, for the second mechanism shown in Fig. 1.14 (b), barrier  $\Delta_{B \rightarrow A}$  at some distant distance becomes smaller than A allowing atom to come back or slide to its original state. In this case, some changes occur but the tip can regain its original structure without disturbing the tip-sample structure meaning that the process is reversible.

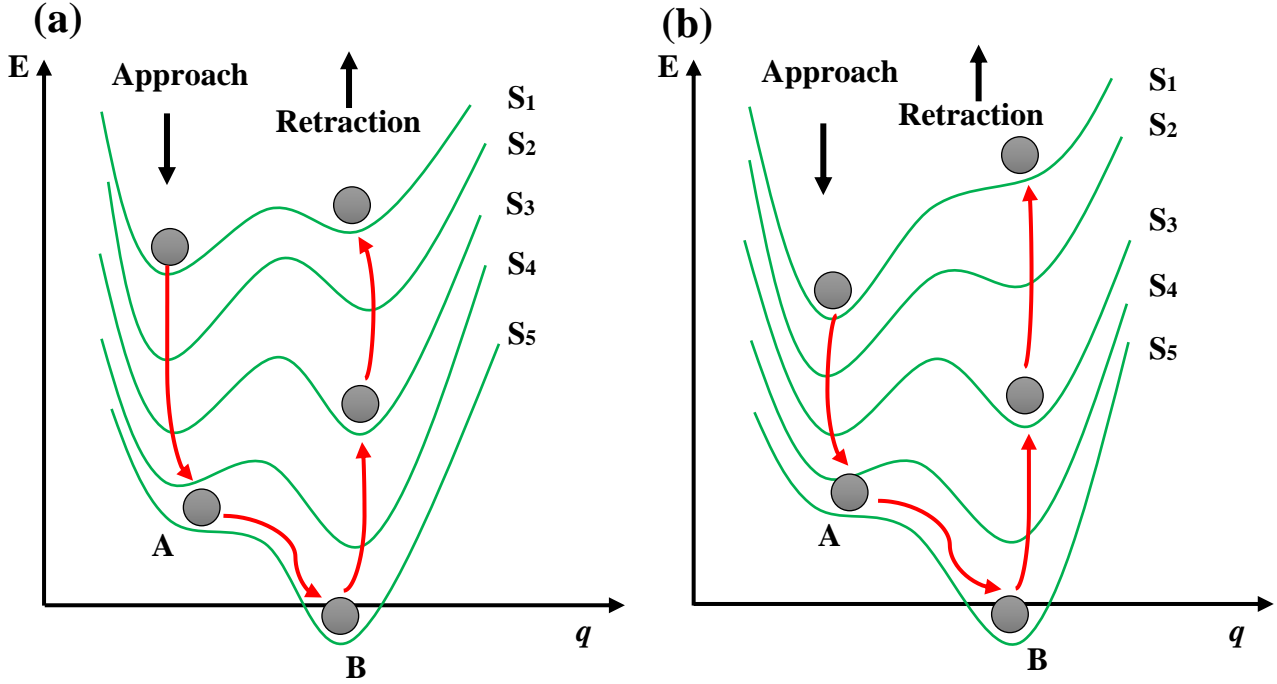


**Figure 1.14:** For tip positions defined by  $S_1$ ,  $S_2$ ,  $S_3$ ,  $S_4$ , and  $S_5$  the approach and retract curve variation of surface potential energy  $E(q)$  (a) structurally irreversible (b) reversible process. A and B are the two local minima concerning  $q$  in the energy. Image concept taken from [72].

### 1.6.2 Joule Heat Energy Dissipation:

After the invention of the FM-AFM technique [12], it is proven that the conservative and nonconservative interaction between tip and sample can be measured simultaneously [9,24,70]. By using a phase lock loop amplifier (PLL) which maintain  $90^\circ$ -phase difference between the excitation force ( $F_{exc}$ ) and vibration force ( $F_{ts}$ ), resonance of the cantilever being assured. Any change in the resonance frequency due to  $F_{ts}$  from a preset value will be considered as a detuning ( $\Delta f$ ) of the cantilever. To keep the vibration amplitude constant of the detuned cantilever, the excitation force ( $F_{exc}$ ) will be increased or decreased through which dissipation can be imaged. The first electric field

mediated energy dissipation was investigated by Denk and Pohl [76]. They showed that under a bias voltage and depending on the local conductivity of the surface elements the tip-sample interaction may create energy dissipation. Under a sample/tip bias, the displacement current can be induced by an oscillating lever, try to pass through the tip-sample resistive region cause Joule heat energy dissipation. It became possible due to high  $Q$  and low intrinsic dissipation of a cantilever inside an ultra-high vacuum. They also indicated that the amount of dissipation can be extracted by monitoring the mechanical  $Q$  of the cantilever. After that many research has been done related to Joule dissipation showing the dependency on the passive components (resistance, capacitance), dopant concentration, carrier mobility, etc [18,77,78]. Using electrical dissipation event, T. D. Stowe et al. first mapped the dopant concentration on the Si surface [77], where using their customized tip-sample model (slightly different from ordinary nc-AFM), they concluded an elementary relationship between the electrical damping with dopant concentration as well as carrier mobility. Their test system consists of a p/p<sup>+</sup> Si-grating with a boron implant concentration of  $10^{15} \text{ cm}^{-2}$  and a single-crystal Si cantilever. A distinct contrast for the p-doped side appeared at the dissipation image shown in Fig. 1.15 (a). From the distance- and voltage-dependent dissipation curve (Fig. 1.15b), damping on the order of  $0.2 \text{ pN}\cdot\text{s/m}$  was obtained at a tip-sample separation distance of  $150 \text{ nm}$ , followed by a  $V_s^2$  behavior up to a voltage of  $\pm 4 \text{ V}$ .

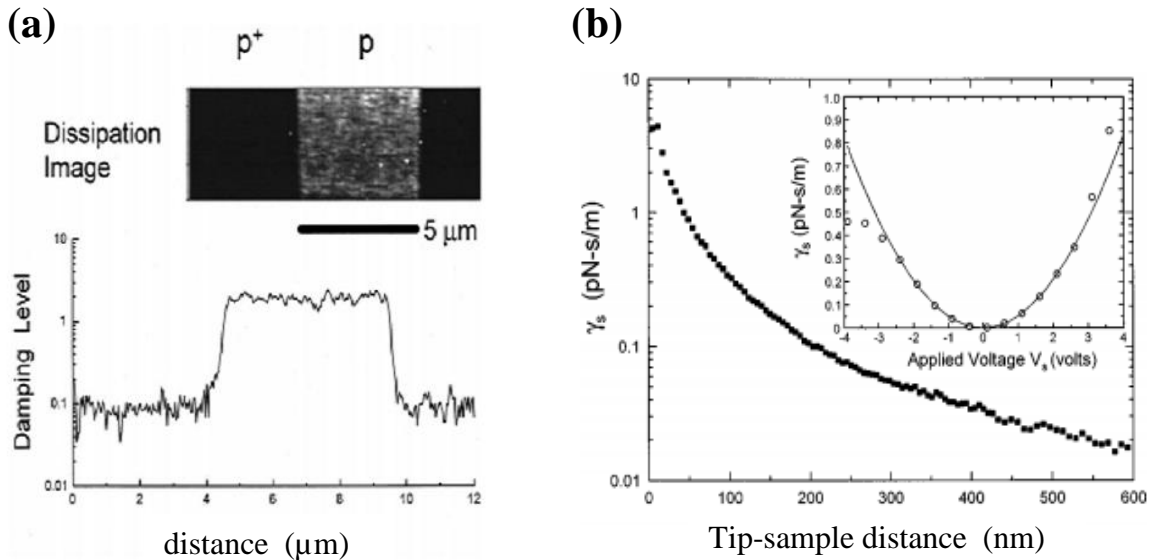


**Figure 1.15:** (a) Dissipation mapping on a p/p<sup>+</sup> Si grating with a tip-sample distance of  $\sim 10$  nm and a sample bias voltage of  $V_s = 0.7$  V. The vibrational amplitude used for imaging was  $A \sim 20$  nm. (b) Damping vs distance curve shows an increment in dissipation of  $\sim 0.2$  pN s/m at a distance of 150 nm; followed by a conventional parabolic behavior under biasing condition (inset). Fig. adapted from [77].

On the other hand, a proportional relationship between cantilever dissipation and resonance frequency shift  $\Delta f$  has been examined by T. Arai *et al.* recently on p-Si (111) surface with the help of clean Si and hydrogen (H)-terminated Si tip [18]. Their result shows that, after terminating clean Si tip with atomic H, the increased resistivity due to H-termination added extra dissipation than that of clean Si-tip under closest separation between tip and sample shown in Fig. 1.16 (a) and (b). Besides, a proportional relationship is also found from their  $\Delta f$ -, and dissipation-distance curve. Their calculated resistance for the clean Si tip and H-terminated tip is  $1.3 \text{ G}\Omega$  and  $12 \text{ G}\Omega$ , respectively, which is responsible for Joule dissipation. The total  $\Delta f$  has been divided into  $\Delta f_{ele}$  and  $\Delta f_{vdW}$  corresponds to long-range electrostatic and van der Waals (vdW) force contribution. The  $\Delta f_{vdW}$  has been calculated after compensating the electrostatic potential using CPD voltage for the Si surface under a fixed bias voltage. Finally,  $\Delta f_{vdW}$  has been subtracted from  $\Delta f$  to get the  $\Delta f_{ele}$ . Although similar behavior is reflected for all  $\Delta f$ ,  $\Delta f_{ele}$ ,  $\Delta f_{vdW}$  vs distance curve (Fig. 1.16) resulted in same tip radius, the only difference appeared in  $V_{CPD}$  due to H-termination. In summary, the Joule dissipation was dominant for the tip and sample surface resistance and that of H-termination.

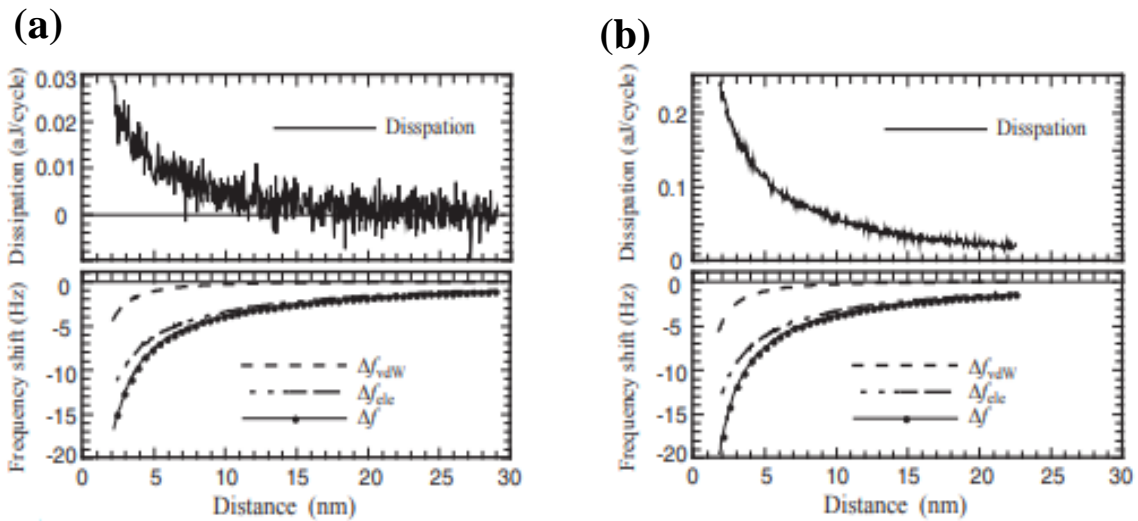


**Figure 1.16:** Plots of  $\Delta f$  – distance and *Dissipation* – distance curve; (a) clean Si tip and (b) H-terminated Si tip. The essential parameter's value used for spectroscopic data acquisition are:  $V_s = -1.56$  V,  $f_0 = 254.2$  kHz,  $k = 21$  N/m, and  $A = 31.5$  nm. Data taken from [18].

## 1.7 Concluding Remarks:

The breakthrough in the scanning probe microscopy (SPM) field happened after the invention of FM-AFM to measure the surface properties in the field of materials science, polymer science as well as molecular biology. The last three decades are considered not only the development area of the FM-AFM system, but various experimental results have also revealed the successful application of FM-AFM. Beyond imaging, surface electrical and mechanical characteristics are measured continuously for 2D thin film, 1D nanowire, or 0D quantum dots. Tunneling current, energy dissipation, and surface potential mapping become available which added extra features for future nanotechnology. Through this chapter, we have studied the revolution of AFM and FM-AFM, the previous and the most recent development by analyzing some published articles. Our concentration was lied down on 2D materials characterized by FM-AFM, the capacitance between tip and sample, contact potential difference (CPD) due to electrostatic interaction, and atomic manipulation technique as those are the most recent hot topics related to FM-AFM as well as the terms related to our present work. We put some simplified discussion through which we can understand those phenomena and relative issues for a further talk in the future.

## 1.8 Remaining Chapter Summary:

Through this thesis work, we will try to characterize the nano electrical properties of a 2D material, for example, force interactions and energy dissipation that acts between the tiny separation of a tip and a sample of an FM-AFM system. We will use artificially synthesized phlogopite mica as a 2D film which is affixed on Ir coated n-type Si (111) substrate mechanically as our main sample and a Pt–Ir coated force sensor. As a motivation of our work, chapter 1 has provided sufficient historical background, most highlighted topics able to perform through FM-AFM, and the future unsettled phenomenon. Based on our understandings from previous literature, our whole experimental works and results will be divided into the following chapters:

**Chapter 2: Background and Principle of AFM:** In this chapter, the main instrumentation of AFM including contact AFM, intermittent contact AFM, and noncontact AFM have been described. Even though the main work has entirely been performed based on frequency modulation technique (FM-AFM), a special type of non-contact AFM, other methods were studied for the purpose of understanding the facts and figures of AFM which may create new ideas for future experiments. Additionally, some minor instruments that were used for sample preparation also be discussed shortly.

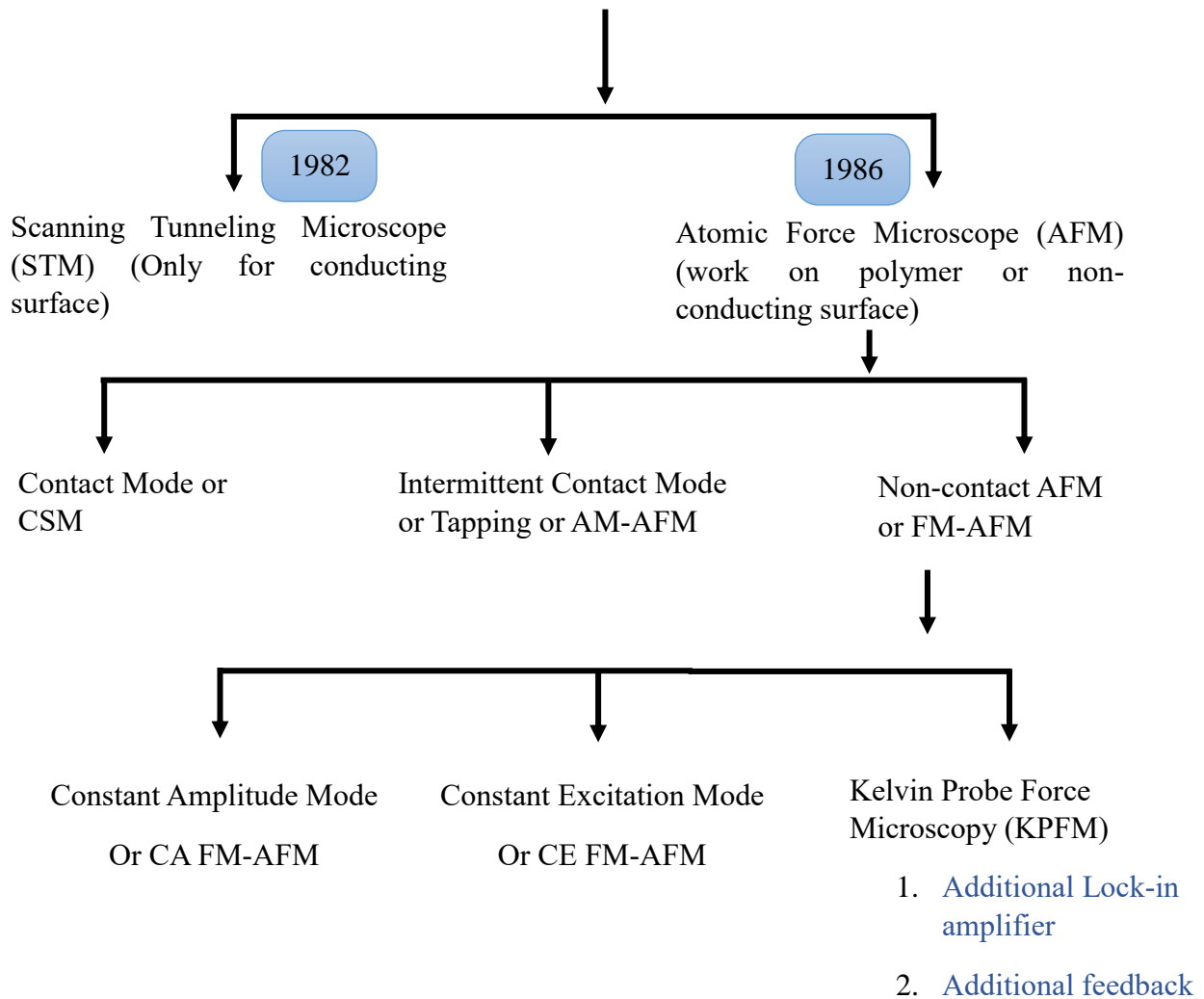
**Chapter 3: Experimental Methods for Sample Preparation and Evaluation:** In this chapter, the newly developed mechanical exfoliation technique to prepare a large 2D mica flat sample has been described comprehensively. The typical microscopy images of the exfoliated nanosheet along with the scanned atomic structure of the mica surface, elemental analysis, and carbon (C) contamination have also been discussed.

**Chapter 4: Evaluation of Mechanical Energy Dissipation Using Frequency Modulation Atomic Force Microscopy:** In this chapter, our currently performed experimental work related to mechanical energy dissipation due to long-range attractive electrostatic interactions under a fixed bias voltage as well as the corresponding surface resistances acting between the metallic tip and metallic sample partly covered with varying dielectric materials using FM-AFM methods have been presented and discussed.

**Chapter 5: Summarization and Future Prospects:** In this chapter, the whole work has been summarized, and possible future insights are described.

## Summarization of SPM

### Scanning Probe Microscope (SPM) - Early 80's



## References:

- [1] G. Binnig, H. Rohrer, Ch. Gerber, E. Weibel, Phys. Rev. 49 (1975) 57–60.
- [2] G. Binnig, C.F. Quate, Ch. Gerber, Phys. Rev. Lett. 56 (1996) 930–933.
- [3] C.F. Quate, T.R. Albrecht, Surf. Sci. 190 (1987) 1–6.
- [4] C.M. Mate, G.M. McClelland, R. Erlandsson, S. Chiang, Phys. Rev. Lett. 59 (1987) 1942–1945.
- [5] G. Meyer, N.M. Amer, Appl. Phys. Lett. 56 (1990) 2100–2101.
- [6] L. Sumio, Nature 354 (1991) 56–58.
- [7] S. Fujisawa, Y. Sugawara, S. Ito, S. Mishima, T. Okada, S. Morita, Nanotechnology 4 (1993) 138–142.
- [8] R. Bennewitz, T. Gyalog, M. Guggisberg, M. Bamberlin, E. Meyer, H.J. Güntherodt, Phys. Rev. B Phys. 60 (1999) R11301–R11304.
- [9] C. Loppacher, R. Bennewitz, O. Pfeiffer, M. Guggisberg, M. Bamberlin, S. Schär, V. Barwich, A. Baratoff, E. Meyer, Phys. Rev. B 62 (2000) 13674–13679.
- [10] R. Lüthi, J. Vac. Sci. Technol. B 14 (1996) 1280–1284.
- [11] Y. Martin, C.C. Williams, H.K. Wickramasinghe, J. Appl. Phys. 61 (1987) 4723–4729.
- [12] T.R. Albrecht, P. Grütter, D. Horne, D. Rugar, J. Appl. Phys. 69 (1991) 668–673.
- [13] F.J. Giessibl, Science 267 (1995) 68–71.
- [14] K. Shin-Ichi, M. Iwatsuki, Jpn. J. Appl. Phys. 34 (1995) L145–L148.
- [15] H. Ueyama, M. Ohta, Y. Sugawara, S. Morita, Jpn. J. Appl. Phys. 34 (1995) L1086–L1088.
- [16] Y. Sugawara, M. Ohta, H. Ueyama, S. Morita, Science 270 (1995) 1646–1648.
- [17] T. Uchihashi, Y. Sugawara, T. Tsukamoto, M. Ohta, S. Morita, M. Suzuki, Phys. Rev. B 56 (1997) 9834–9840.
- [18] T. Arai, D. Kura, R. Inamura, M. Tomitori, Jpn. J. Appl. Phys. 57 (2018) 08NB04-1–6.
- [19] Y. Martin, D.W. Abraham, H.K. Wickramasinghe, Appl. Phys. Lett. 52 (1988) 1103–1105.



- [20] L. Jiang, J. Weber, F.M. Puglisi, P. Pavan, L. Larcher, W. Frammelsberger, G. Benstetter, M. Lanza, *Materials* 12 (2019) 1–10.
- [21] M.R. Islam, M. Tomitori, *Appl. Surf. Sci.* 532 (2020) 147388–147394.
- [22] M.P. Boneschanscher, J. Van Der Lit, Z. Sun, I. Swart, P. Liljeroth, D. Vanmaekelbergh, *ACS Nano* 6 (2012) 10216–10221.
- [23] S. Patil, A. V. Kulkarni, C.V. Dharmadhikari, *J. Appl. Phys.* 88 (2000) 6940–6942.
- [24] B. Gotsmann, C. Seidel, B. Anczykowski, H. Fuchs, *Phys. Rev. B* 60 (1999) 11051–11061.
- [25] A.A. Farrell, T. Fukuma, T. Uchihashi, E.R. Kay, G. Bottari, D.A. Leigh, H. Yamada, S.P. Jarvis, *Phys. Rev. B* 72 (2005) 1–6.
- [26] N. Oyabu, Ó. Custance, I. Yi, Y. Sugawara, S. Morita, *Phys. Rev. Lett.* 90 (2003) 176102–176106.
- [27] T. Okajima, H. Tokumoto, *Jpn. J. Appl. Phys.* 43 (2004) 4634–4638.
- [28] M. Kageshima, H. Jensenius, M. Dienwiebel, Y. Nakayama, H. Tokumoto, S.P. Jarvis, T.H. Oosterkamp, *Appl. Surf. Sci.* 188 (2002) 440–444.
- [29] H. Sekiguchi, T. Okajima, H. Arakawa, *Appl. Surf. Sci.* 210 (2003) 61–67.
- [30] S.P. Jarvis, T. Uchihashi, T. Ishida, H. Tokumoto, Y. Nakayama, *J. Phys. Chem. B* 104 (2000) 6093–6094.
- [31] H. Uchida, D. Huang, F. Grey, M. Aono, *Phys. Rev. Lett.* 70 (1992) 2040–2043.
- [32] I. Lyo, P. Avouris, *Science* 253 (1991) 173–175.
- [33] A. Kobayashi, F. Grey, R.S. Williams, M. Aono, *Science* 259 (1993) 1724–1726.
- [34] Y. Sugawara, Y. Sano, N. Suehira, S. Morita, *Appl. Surf. Sci.* 188 (2002) 285–291.
- [35] D.S. Wastl, A.J. Weymouth, F.J. Giessibl, *Phys. Rev. B* 87 (2013) 1–10.
- [36] J.M.R. Weaver, D.W. Abraham, *J. Vac. Sci. Technol. B* 9 (1991) 1559–1561.
- [37] S.S. and T. Glatzel, *Kelvin Probe Force Microscopy* (2018).
- [38] S. Hudlet, M. Saint Jean, C. Guthmann, J. Berger, *Eur. Phys. J. B* 2 (1998) 5–10.

- [39] S. Hudlet, M. Saint Jean, B. Roulet, J. Berger, C. Guthmann, J. Phys. I 4 (1994) 1725–1742.
- [40] K.I. Umeda, K. Kobayashi, N. Oyabu, Y. Hirata, K. Matsushige, H. Yamada, J. Appl. Phys. 113 (2013) 154311–154322.
- [41] A. Sadeghi, A. Baratoff, S. Goedecker, Phys. Rev. B 88 (2013) 1–8.
- [42] A. Sadeghi, A. Baratoff, S.A. Ghasemi, S. Goedecker, T. Glatzel, S. Kawai, E. Meyer, Phys. Rev. B 86 (2012) 075407–075427.
- [43] M. Guggisberg, M. Bammerlin, C. Loppacher, O. Pfeiffer, A. Abdurixit, V. Barwich, R. Bennewitz, A. Baratoff, E. Meyer, H. Güntherodt, Phys. Rev. B 61 (2000) 11151–11155.
- [44] M. Goryl, J.J. Kolodziej, F. Krok, P. Piatkowski, B. Such, M. Szymonski, Microelectron. Eng. 81 (2005) 394–399.
- [45] F. Krok, K. Sajewicz, J. Konior, M. Goryl, P. Piatkowski, M. Szymonski, Phys. Rev. B 77 (2008) 1–9.
- [46] C. Barth, C.R. Henry, Nanotechnology 17 (2006) S155–S161.
- [47] C. Sommerhalter, T. Glatzel, T.W. Matthes, A. Jäger-Waldau, M.C. Lux-Steiner, Appl. Surf. Sci. 157 (2000) 263–268.
- [48] T. Glatzel, S. Sadewasser, R. Shikler, Y. Rosenwaks, M.C. Lux-Steiner, Mater. Sci. Eng. B Solid-State Mater. Adv. Technol. 102 (2003) 138–142.
- [49] C. Barth, C.R. Henry, Appl. Phys. Lett. 89 (2006) 2–5.
- [50] I.V. Grigorieva, A.A. Firsov, K. S. Novoselov, A. K. Geim, S. V. Morozov, D. Jiang, Y. Zhang, S. V. Dubonos, Science 306 (2016) 666–669.
- [51] M.D. Stoller, S. Park, Y. Zhu, J. An, R.S. Ruoff, Nano Lett. 8 (2008) 6–10.
- [52] C. Lee, X. Wei, J.W. Kysar, J. Hone, Science 321 (2008) 385–388.
- [53] R.R. Nair, P. Blake, A.N. Grigorenko, K.S. Novoselov, T.J. Booth, T. Stauber, N.M.R. Peres, A.K. Geim, Science 320 (2008) 1308.
- [54] A.A. Balandin, S. Ghosh, W. Bao, I. Calizo, D. Teweldebrhan, F. Miao, C.N. Lau, Nano Lett. 8 (2008) 902–907.

- [55] L.A. Ponomarenko, R. V. Gorbachev, G.L. Yu, D.C. Elias, R. Jalil, A.A. Patel, A. Mishchenko, A.S. Mayorov, C.R. Woods, J.R. Wallbank, M. Mucha-Kruczynski, B.A. Piot, M. Potemski, I. V. Grigorieva, K.S. Novoselov, F. Guinea, V.I. Fal'Ko, A.K. Geim, *Nature* 497 (2013) 594–597.
- [56] X. Huang, Z. Zeng, H. Zhang, *Chem. Soc. Rev.* 42 (2013) 1934–1946.
- [57] H. Zhang, *ACS Nano* 9 (2015) 9451–9469.
- [58] C. Zhi, Y. Bando, C. Tang, H. Kuwahara, D. Golberg, *Adv. Mater.* 21 (2009) 2889–2893.
- [59] K.S. Novoselov, D. Jiang, F. Schedin, T.J. Booth, V. V. Khotkevich, S. V. Morozov, A.K. Geim, *Proc. Natl. Acad. Sci.* 102 (2005) 10451–10453.
- [60] H. Li, Z. Yin, Q. He, H. Li, X. Huang, G. Lu, D.W.H. Fam, A.I.Y. Tok, Q. Zhang, H. Zhang, *Small* 8 (2012) 63–67.
- [61] J.N. Coleman, M. Lotya, A. O'Neill, S.D. Bergin, P.J. King, U. Khan, K. Young, A. Gaucher, S. De, R.J. Smith, I. V. Shvets, S.K. Arora, G. Stanton, H.Y. Kim, K. Lee, G.T. Kim, G.S. Duesberg, T. Hallam, J.J. Boland, J.J. Wang, J.F. Donegan, J.C. Grunlan, G. Moriarty, A. Shmeliov, R.J. Nicholls, J.M. Perkins, E.M. Grieveson, K. Theuvsen, D.W. McComb, P.D. Nellist, V. Nicolosi, *Science* 331 (2011) 568–571.
- [62] A.H. Khan, S. Ghosh, B. Pradhan, A. Dalui, L.K. Shrestha, S. Acharya, K. Ariga, *Bull. Chem. Soc. Jpn.* 90 (2017) 627–648.
- [63] Y. Bitla, Y.H. Chu, *FlatChem* 3 (2017) 26–42.
- [64] R.M. Hazen, C.W. Burnham, *Amer. Mineral.* 58 (1973) 889–900.
- [65] A. Castellanos-Gomez, M. Poot, A. Amor-Amorós, G.A. Steele, H.S.J. van der Zant, N. Agrait, G. Rubio-Bollinger, *Nano Res.* 5 (2012) 550–557.
- [66] Y. He, H. Dong, Q. Meng, L. Jiang, W. Shao, L. He, W. Hu, *Adv. Mater.* 23 (2011) 5502–5507.
- [67] S.G. Barlow, D.A.C. Manning, *Br. Ceram. Trans.* 98 (1999) 122–126.
- [68] D. McCoul, W. Hu, M. Gao, V. Mehta, Q. Pei, *Adv. Electron. Mater.* 2 (2016) 1–51.
- [69] E. Gneco, R. Bennewitz, T. Gyalog, C. Loppacher, M. Bamberlin, E. Meyer, H.J.

Güntherodt, Phys. Rev. Lett. 84 (2000) 1172–1175.

- [70] B. Gotsmann, W. Allers, H. Hölscher, U.D. Schwarz, R. Wiesendanger, H. Fuchs, Phys. Rev. B 64 (2001) 1–6.
- [71] C. Loppacher, M. Bammerlin, M. Guggisberg, S. Schär, R. Bennewitz, A. Baratoff, E. Meyer, H.J. Güntherodt, Phys. Rev. B 62 (2000) 16944–16949.
- [72] E. Meyer, S. Morita, R. Wiesendanger, Noncontact Atomic Force Microscopy (2002).
- [73] G. Cross, A. Schirmeisen, A. Stalder, P. Grütter, M. Tschudy, U. Dürig, Phys. Rev. Lett. 80 (1998) 4685–4688.
- [74] U. Dürig, H.R. Steinauer, N. Blanc, J. Appl. Phys. 82 (1997) 3641–3651.
- [75] H. Yoshizawa, Y.L. Chen, J. Israelachvili, J. Phys. Chem. 97 (1993) 4128–4140.
- [76] W. Denk, D.W. Pohl, Appl. Phys. Lett. 59 (1991) 2171–2173.
- [77] T.D. Stowe, T.W. Kenny, D.J. Thomson, D. Rugar, Appl. Phys. Lett. 75 (1999) 2785–2787.
- [78] T. Fukuma, K. Umeda, K. Kobayashi, H. Yamada, K. Matsushige, Jpn. J. Appl. Phys. 41 (2002) 4903–4907.

## Chapter 2:

### Background and Principle of AFM

The invention of AFM [1] (with the integration of STM and stylus profilometer (SP)) widened the field of interest from conductor to insulator. The first idea was inaugurated by observing the complex and significant interaction forces that have taken place simultaneously with the tunneling current in an STM experiment [2]. Therefore, based on these interaction forces between a sharp tip and sample, AFM can resemble the three-dimensional mapping of the surfaces of different materials. AFM can work on several modes typically termed as contact/static AFM and non-contact/dynamic AFM. Unlike STM, in the tunneling region, the potential energy between tip and sample depending on the modes of operation causes a vertical force ( $F_{ts} = -\partial V_{ts}/\partial z$ ) as well as a force gradient ( $k_{ts} = -\partial F_{ts}/\partial z$ ) considered as the prime signal parameter for imaging on the sample surfaces [3]. The force/force gradient is reflected as a cantilever deflection measured by the detector. In this chapter, we will introduce our AFM apparatus, shortly discuss contact AFM followed by a brief discussion focused on non-contact AFM (nc-AFM).

#### 2.1 Instrumentation with Fundamental Contact AFM Mode:

In the contact mode operation, we engage the sample stage (with various samples) slowly towards the tip until the repulsion between tip and sample becomes dominant. Under a defined repulsive force interaction when the detector reads the deflection of the cantilever at zero (0V) concerning the initial setpoint (typically  $-0.25$  V) the approaching will be stopped immediately. In this operation, the forces are converted to cantilever deflection i.e.  $q_{def} = F_{ts}/k$ . This present research project has been run through an AFM system modeled as 5500 AFM/SPM, Agilent Technologies, Inc. provided by Santa Clara, CA, USA. The experiment was conducted in the air with a controlled environmental chamber at room temperature. The apparatus that came along with this AFM setup has been displayed in Fig. 2.1. The AFM consists of PicoScan™ 2500 controller (Fig. 2.1a), several specialized magnetic AMF stages with a controlled environmental glass chamber (Fig. 2.1b), a video imaging camera, and the isolation shield (Fig. 2.1c). Using this contact AFM system,

we can measure the topography, amplitude, friction, and current images simultaneously with the PicoScan 5.3.2 software pre-installed in a dedicated computer (Fig. 1a).

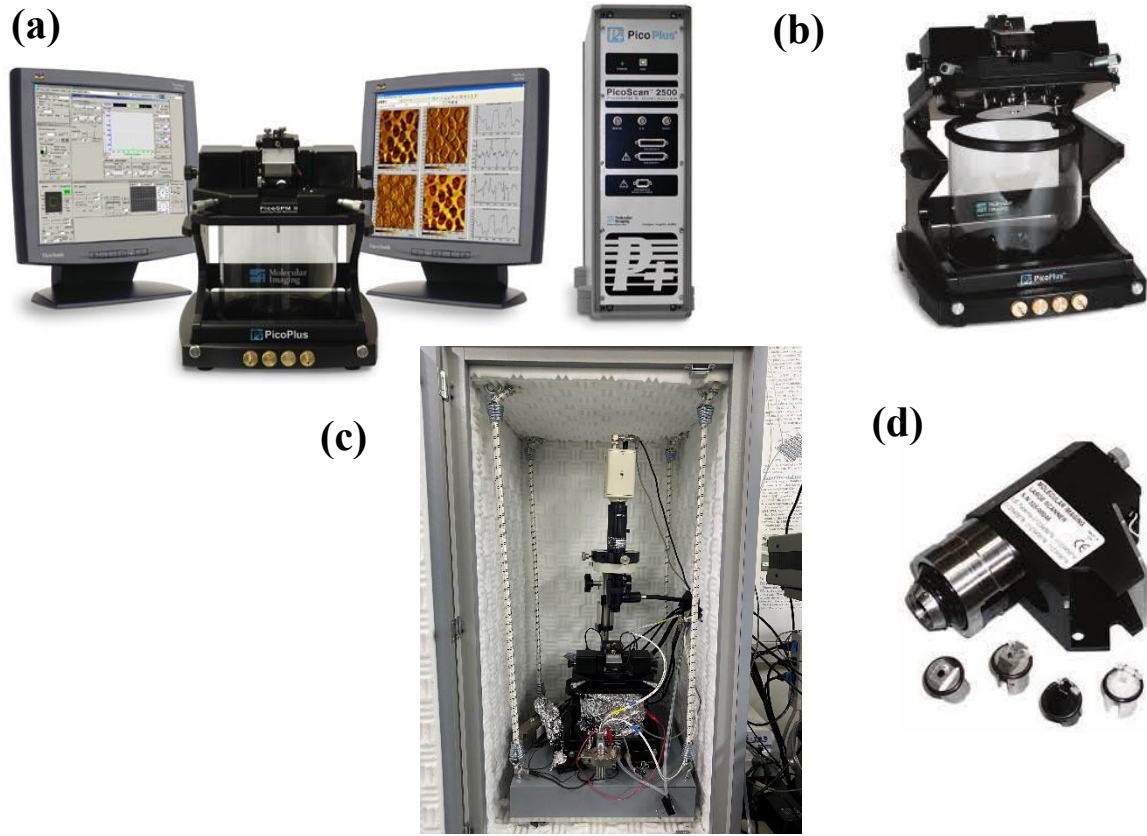


**Figure 2.1:** PicoPlus SPM original apparatus of 5500 AFM/SPM consists of (a) PicoScan™ 2500 controller, dedicated computer with pre-installed software; (b) controlled environmental glass chamber; (c) video imaging camera with isolation chamber; (d) AFM scanner with different types of noses.

A schematic diagram of contact AFM has been represented in Fig. 2.2. The working principle is as follows; A cantilever (spring constant typically,  $k = 0.01\text{--}5\text{ N/m}$  and resonance frequency at least  $f_0 = 2\text{ kHz}$ ) having a sharp tip at its end scan across the sample surface [4]. Due to the surface roughness, the laser reflected from the backside of the cantilever is deflected from the setpoint which is monitored by a phase-sensitive photodiode (PSPD). Hence, the imaging can be done through the raster scanning between tip and sample. Although the contact AFM was initially considered a perfect imaging tool for insulators or other types of substrate materials, soon it also confined to hard materials

due to the two-dimensional stick-slip process and the relative energy dissipation event. The high loading force on the cantilever may damage the biological sample (for example living cell, DNA, etc.) and soft polymers. For those necessities as well as to resolve the high loading force and large energy dissipation phenomenon, a dynamic AFM system has been developed for imaging and sample characterization.

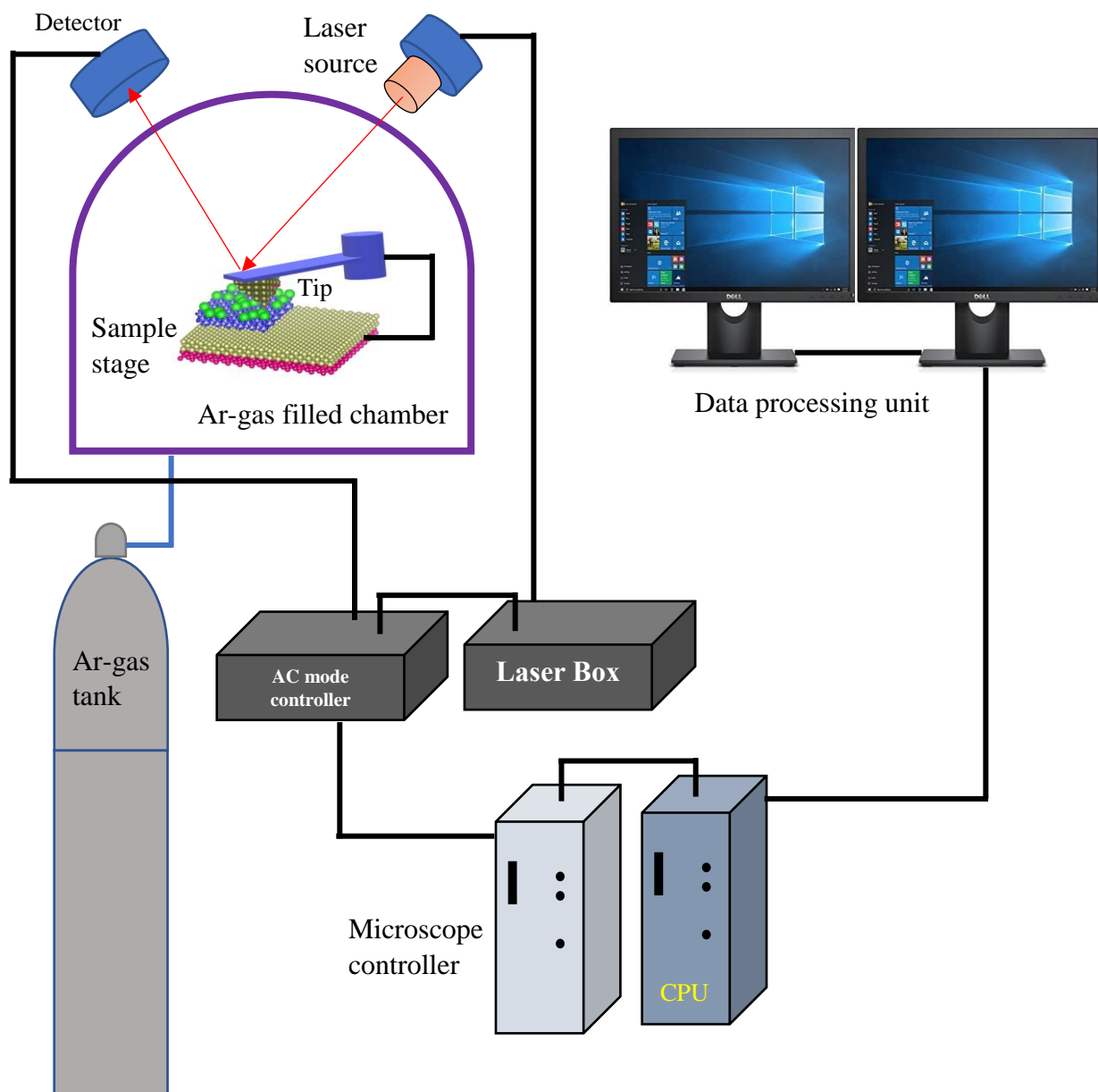


**Figure 2.2:** A schematic diagram of AFM (5500 AFM/SPM, Agilent Technologies) operated in contact AFM mode. An AFM instrument generates topographic images by moving a small cantilever

over the surface of a sample. A sharp tip is attached to the end of the cantilever that contact with the sample surface reflecting a laser beam from the backside of the cantilever is detected by a photodetector.

### 2.1.1 Imaging with Contact AFM:

Using the above-mentioned procedure, we imaged a test grating to check the system functionality, image stability, and scanner calibration shown in Fig. 2.3. A diffraction grating typically consists of a large number of parallel grooves also called slits with a finite groove spacing (called pitch) between them. We used the PNP-TR-Au ( $f_0 = 67$  kHz,  $k = 0.32$   $\text{Nm}^{-1}$ , double side Au coated) tip for scanning using the large scanner (max. area  $80 \times 80$   $\mu\text{m}^2$ ) of our AFM system. Our  $11 \times 11$   $\mu\text{m}^2$  scanning area consists of  $\sim 9$  parallel grooves with pitches of  $0.2$   $\mu\text{m}$  and height of  $\sim 160$  nm shown in Fig. 2.3 (a) and (b). Height has been measured across the green horizontal line (Fig. 2.3a). Figure 2.3 (c) shows the commercially available gratings which always use for scanner calibration. A 3D slits and pitches of the corresponding grating are shown in Fig. 2.3 (d).

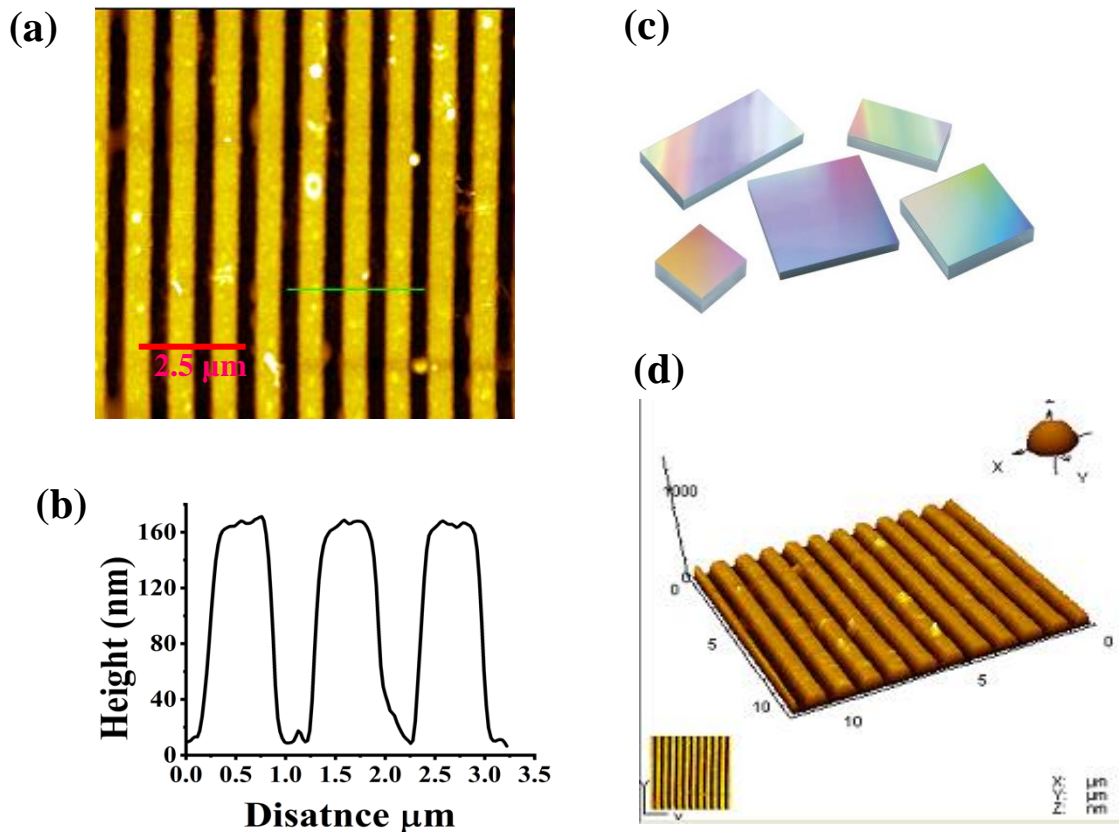




**Figure 2.3:** Test measurement using contact AFM method: (a) Top view of test grating with an  $11 \times 11 \mu\text{m}^2$  scan area, (b) height of the groove shows a pitch distance of  $0.2 \mu\text{m}$ , (c) commercially available experimental gratings, (d) 3D representation of test grating.

## 2.2 Noncontact AFM Mode:

Noncontact/dynamic AFM (nc-AFM/d-AFM) was developed soon after the invention of AFM, an alternative advanced imaging technique where both tip and sample surface being preserved for a long period due to noncontact imaging behavior. In this method, a vibrating cantilever with a sharp tip having high eigenfrequency ( $f_0$ ) and spring constant ( $k$ ) can oscillate at its resonance frequency near the sample surface, capable of being provided the atom resolved images without touching the sample surfaces, hence the name nc-AFM/ d-AFM is satisfied. Any change in the cantilever vibration can be monitored by tracking its resonance frequency shift, vibrational amplitude change, or phase shift under tip-sample interactions. Depending on the instrumentation when nc-AFM is employed in an experiment, two typical special modes are used known as amplitude-modulation (Fig. 2.4a) atomic force microscopy (AM-AFM) and frequency-modulation (Fig. 2.4b) atomic force microscopy (FM-AFM) [5,6]. Our present AFM system (5500 AFM/SPM) is fit for both AM-AFM and FM-AFM modes. The AM-AFM or acoustic AFM mode was a built-in option in our AFM system while we customized our AFM by adding a phase-lock-loop (PLL) (or frequency demodulator) to work with FM-AFM mode. Therefore, both AM-AFM and FM-AFM will be discussed briefly by referring to it as principal instrumentation for this present research project as well as the corresponding fundamental knowledge to operate any nc-AFM.

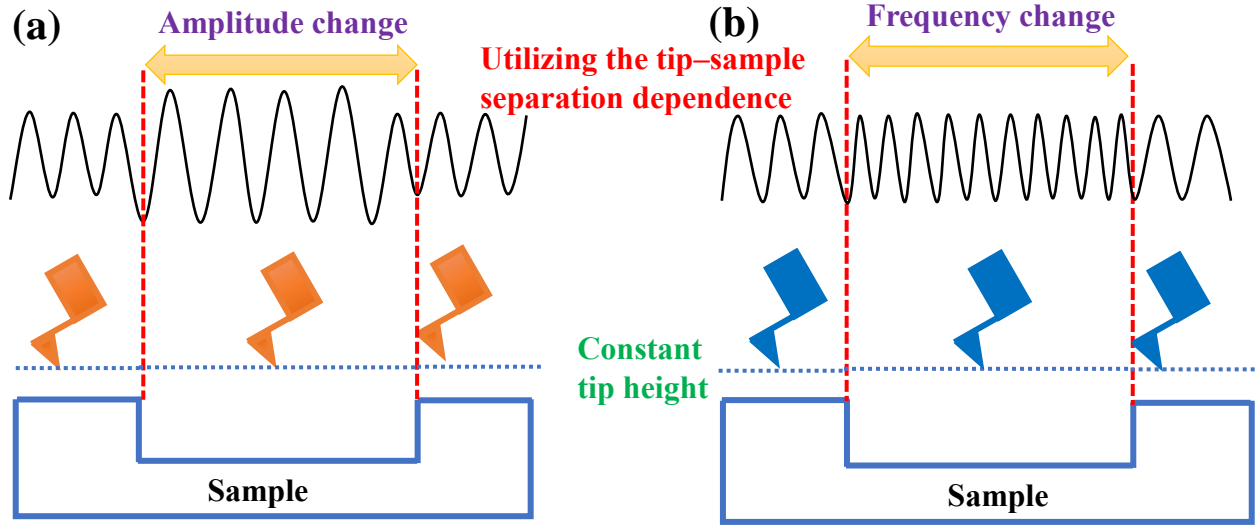


**Figure 2.4:** Schematics of two separate nc-AFM working modes; (a) AM-AFM uses oscillation amplitude as feedback; (b) FM-AFM uses the frequency shift of the cantilever as feedback. In both cases, the distance between tip and sample maintains constant depending on force interactions.

### 2.2.1 Principles and Operation of AM-AFM:

Based on the analytical model proposed by Martin et al. [7] where oscillation amplitude was changed due to the force gradient ( $k_{ts}$ ) acting between tip and sample for a small vibrational amplitude cantilever, Zhong et al. [8] used the amplitude change as a feedback parameter to keep the tip-sample distance constant. Moreover, they suggested using a large oscillation amplitude and a stiff cantilever for the stability criterion of the measurement. In an AM-AFM measurement, a microcantilever excitation can be made through an acoustic or magnetic excitation scheme. By applying an ac-voltage to the piezo-actuator, it is possible to vibrate the cantilever almost or near to its resonance frequency ( $f$ ). On the other hand, a magnetic coil and lever are used to produce resonance in magnetic mode. In the static equilibrium position under tip-sample interaction ( $F_{ts}$ ), the bending of the cantilever can be described by the following equation –

$$F_{ts} = -k_{eff}\Delta L \quad (12)$$

where  $\Delta L$  is the static offset as indicated in the Fig. 2.5 and  $k_{eff}$  is the effective spring constant.

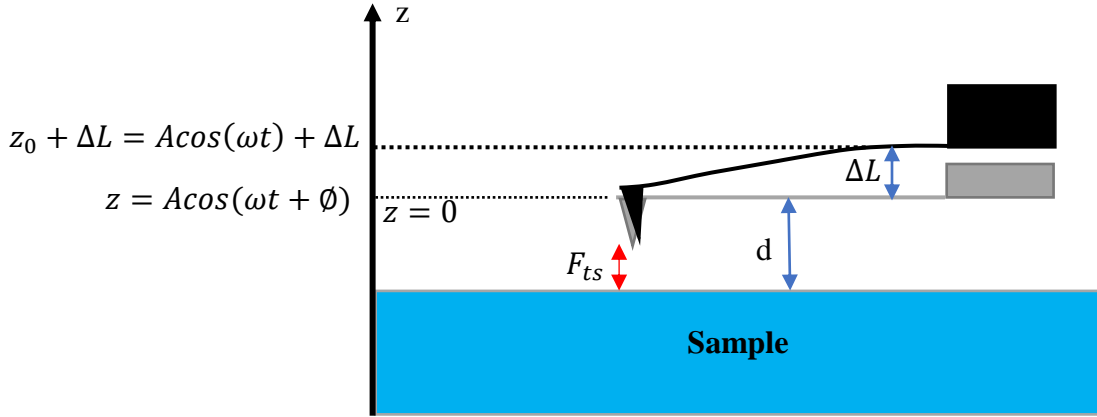


**Figure 2.5:** Schematic of tip-sample interaction. The gray cantilever represents the position when the sample far away results in no interaction between tip and sample. However, under force interaction at close separation, the cantilever attracts towards the sample. Therefore, to keep the distance similar as before the piezo moves in the opposite direction left a bending phenomenon (offset) shown by the black cantilever.

Now, let us consider that an excitation/drive ac-signal i.e.  $z_{drive} = A_{drive} \cos(\omega_{drive}t)$  having fixed oscillation amplitude  $A_{drive}$  and frequency  $\omega_{drive}$  has been applied to the base of the cantilever which results in an oscillation defined by  $z = A \cos(\omega_{drive}t + \phi)$  at its equilibrium position. By considering the probe as a point mass, the equation of motion for the driven damped lever can be described using second-order differential equation –

$$m\ddot{z} + \frac{m\omega_0}{Q}\dot{z} + k_{eff}(z - z_{drive}) = 0 \quad (13)$$

where  $m, Q, \omega_0, k_{eff}$  are the effective mass, quality factor, angular frequency, and the effective spring constant of the cantilever, respectively. We removed the tip-sample interaction ( $F_{ts}$ ) from the above equation as it is already canceled by tip bending (Eq. 1) under active interaction. As the spring

constant ( $k$ ) has been replaced by the effective spring constant ( $k_{eff}$ ) which includes the tip-sample force effect ( $F_{ts}$ ), the resonance frequency shift will be given by –

$$\Delta\omega = \omega'_0 - \omega_0 = \omega_0 \frac{k'}{2k} = -\frac{\omega_0}{2k} \frac{\partial F_{ts}}{\partial z} = -\frac{\omega_0}{2k} k_{ts} \quad (14)$$

Where  $k$  and  $k'$  are the spring constant of a spring and small force gradient due to interaction for a real spring-mass oscillation system and  $\omega'_0$  is the resonance frequency shift under effective spring constant  $k_{eff}$ . The meaning of the above equation is that the frequency shift of a cantilever is proportional to the gradient ( $k_{ts}$ ) of the tip-sample force. A schematic of AM-AFM is shown in Fig. 2.6. Initially, an excitation signal (with angular frequency  $\omega$ ) is provided for the excitation of the cantilever having a high resonance frequency. Typically, a dither piezo is used for the excitation of the electric actuator. When this piezo element shakes the base of the cantilever with a frequency higher than the resonance frequency ( $f$ ) of the cantilever, the resulting oscillation occurs a large resonance amplitude ( $A$ ) of the cantilever. Now, if we engage the tip and sample to each other, the resulting force interaction ( $F_{ts}$ ) will change the resonance frequency of the cantilever which follows an additional change in the resonance amplitude shown in Fig. 2.4 (a). The cantilever will be deflected and the change will be detected through the PSPD. The signal is then fed into a preamplifier and converted to a voltage signal ( $V_{ac}$ ) with the same magnitude as the cantilever deflection. A lock-in amplifier is then measured the amplitude ( $A$ ) and phase ( $\phi$ ) of the ac-signal and provided a dc output ( $V_{dc}$ ) corresponding to the same magnitude of the ac input. This quasi-dc signal is used for the z-feedback controller. Relative comparison between measured amplitude from the cantilever deflection and the setpoint amplitude, the new position of the cantilever will be set by z-feedback circuit. Thus, by controlling the z-controller, the height or the roughness, as well as the real topography of the targeted sample, is sensed and imaged.

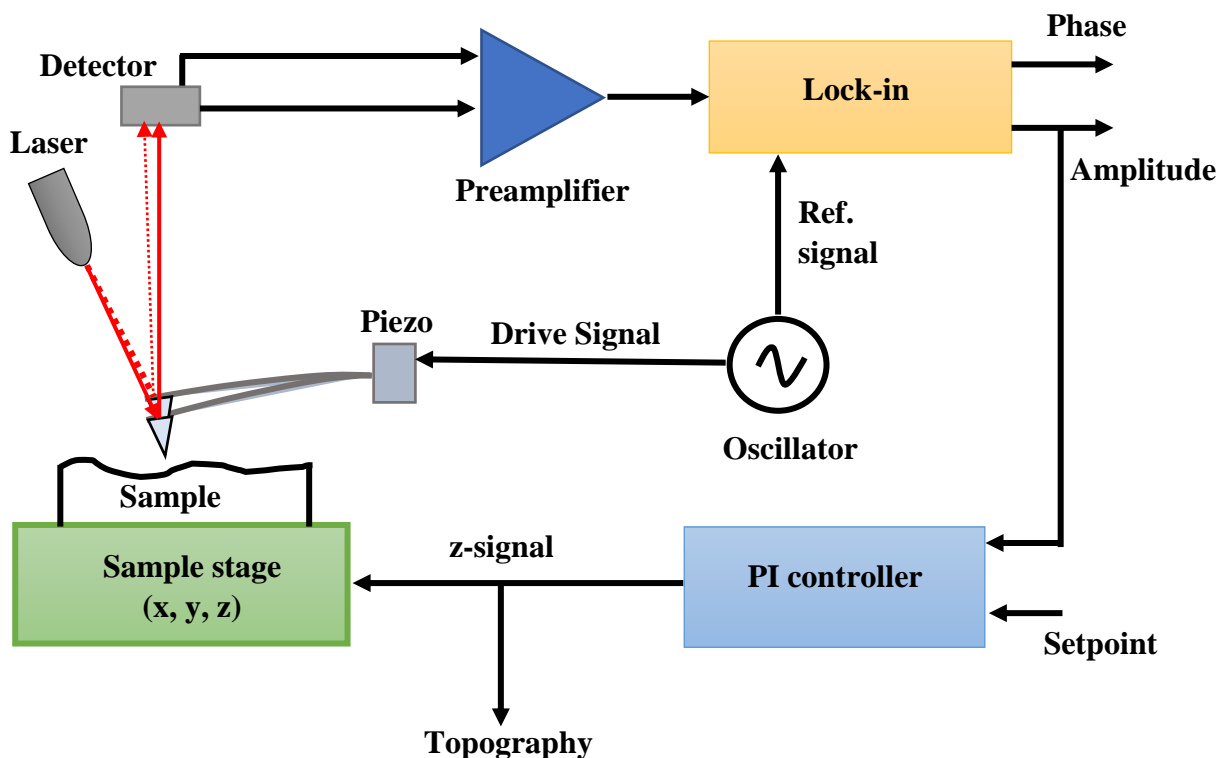


**Figure 2.6:** AM-AFM experimental setup where the detected signal has been modified by a lock-in amplifier and a PI-controller for z-feedback. A force sensor having a high frequency ( $f$ ) and stiff spring constant ( $k$ ) is used for those experiments.

### 2.2.1.1 Imaging with AM-AFM:

Investigation and image acquisition of surfaces by the AM-AFM method have been considered a great achievement at recent scanning field technology especially for biological samples, for example, DNA, proteins, and polymers which need to preserve their environment completely both in the vacuum or in the air, not only because of their special method of working but also guaranteed that it will not damage the surface at their molecular level. Using the above-mentioned AM-AFM setup, we imaged commercially available linear DNA (plasmid pGem7zf+) molecules (3000 b.p.) which are deposited onto freshly cleaved mica with varying humidity at the time of the experiment was

approximately 35-50% shown by Fig 2.7 (a). Approx. 2nm height has also been found from our imaged topography as well known for DNA helix. The brighter spot that appeared on the DNA sample probably due to airborne dust as this sample is too old. Additionally, we also imaged a different sample i.e. GaAs(111)B surfaces (Fig. 2.7b) prepared by molecular beam epitaxy (MBE) on a GaAs substrate. Our results show a pyramid-like shape with an average roughness of  $\sim 40$  nm. However, clear bright distinctive features appeared for two different surfaces. We used an nc-AFM Si cantilever (OMCL-AC160TS-R3, OLYMPUS, Japan) having  $f_0 = 308$  kHz,  $k = 26$  Nm $^{-1}$ ,  $A = 22$  nm for imaging. All measurements were done in an Ag-gas-supplied controlled chamber.

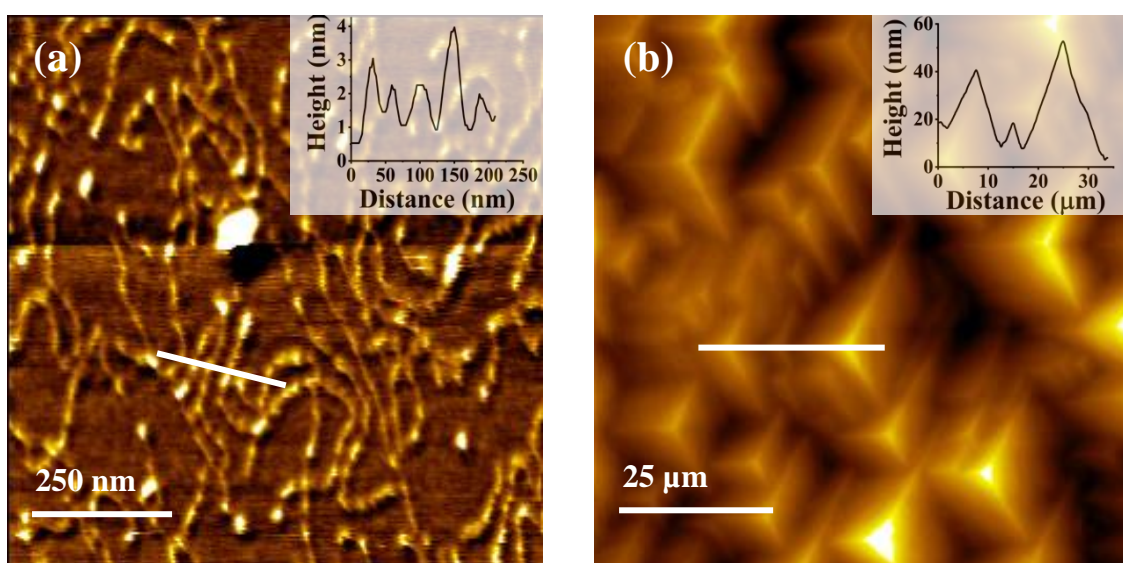


**Figure 2.7:** AM-AFM image of (a) DNA (plasmid pGem7zf+) molecules deposited on mica. The height of the DNA has been measured to  $\sim 2$  nm; (b) GaAs(111)B on GaAs substrate deposited by MBE. The average roughness of the reflected pyramids is  $\sim 40$  nm.

### 2.2.2 Principles and Operation of FM-AFM:

Although by using the periodic motion of the cantilever at resonance the AM-AFM technique resolved the tip degradation process and jump into contact (JIC) instability, application of this method is not suitable in UHV due to the increment in mechanical quality factor (or  $Q$ -value) which possesses restriction on the available bandwidth of the system. Often, the  $Q$  value of a vibrating cantilever

(having  $f_0 \sim 200 - 400$  kHz) in an ultra-high vacuum ( $\sim 50\ 000$ ) enhances 500 times than in air ( $\sim 100$ ) [2]. The minimum detectable frequency shift of AM-AFM is given by [5] –

$$\delta(\Delta f) = \sqrt{\frac{f_0 k_B T B}{4\pi k Q \langle z_{osc}^2 \rangle}} \quad (15)$$

Where  $\langle z_{osc}^2 \rangle$  is the mean square oscillation amplitude,  $k_B T$  is the thermal energy,  $f_0$  is the eigenfrequency,  $k$  is the stiffness of the cantilever, and  $B$  is the maximum available bandwidth.  $B$  also defines the pixels per second (i.e.,  $128 \times 128$ ,  $256 \times 256$ , or  $1024 \times 1024$ , etc.) for an area to be recorded. As the  $Q$  value enhances in the UHV, the sensitivity also increases 20 – 25 times inside the UHV [6]. However, the amplitude response of AM-AFM inside the UHV occurs very slowly which limits AM-AFM not to use in UHV. The time constant for AM-AFM is –

$$\tau = \frac{2Q}{f_0} \quad (16)$$

Which shows a linear relationship between the time scale of the amplitude change and the  $Q$  value. Therefore, AM-AFM is not suitable for vacuum applications.

An alternative technique introduced by T.R. Albrecht et. al. [9] known as frequency modulation atomic force microscopy (FM-AFM) shown in Fig. 4 (b) solves this problem where direct monitoring the frequency shift ( $\Delta f$ ) of a cantilever allows us to measure the variation of the force gradient ( $k_{ts}$ ) between the tip and sample. In FM-AFM, the cantilever act as a frequency-determining component of a constant amplitude oscillator at resonance. When this cantilever vibrates at its resonance frequency ( $f$ ) near a sample surface, a sudden change in the force gradient ( $k_{ts}$ ) shifts the resonant frequency which is detected by a frequency (FM) demodulator tracking system. By using a positive feedback system, the cantilever is kept at its resonance oscillation. Also, an automatic gain control (AGC) circuit maintains the vibration amplitude constant of the cantilever set by the user. A bandpass filter removes the unwanted signal noise and a phase lock loop (PLL) maintains the constant phase ( $\sim 90^\circ$ ) between the excitation signal and cantilever deflection which ensures resonance of the cantilever. During FM-AFM scanning, the tip-sample distance is varied to keep a constant change in

$\Delta f$  of the cantilever. Therefore, this method is also regarded as a mapping of constant frequency shift ( $\Delta f$ ) of the cantilever over the sample surface.

### 2.2.2.1 Fundamental Explanation and Relation between $\Delta f$ and Force Interaction ( $F_{ts}$ ):

In the FM-AFM method, the interaction forces ( $F_{ts}$ ) can be calculated through the observation of resonance frequency shift ( $\Delta f$ ) of the cantilever which is an indirect procedure compared to that of the STM method. Therefore, complexity appears not only for the conversion of  $\Delta f$  to  $F_{ts}$  but also for the separation of several long-range (electrostatic force, van der Waals force, etc.) and short-range (chemical bonding force, short-range adhesive force, etc.) forces. One prime point about FM-AFM is that by using a large oscillation amplitude cantilever near the sample surface the interaction range [10] between tip and sample becomes relatively lower than that of the typical amplitude range. Hence, the cantilever encounters the force interaction ( $F_{ts}$ ) for a very small part of its oscillation period and thereby changes its resonance frequency. For experimentalists, it is extremely necessary to understand the relationship between  $\Delta f$  and forces for a proper explanation. Although the tip-sample interaction phenomenon is entirely a three-dimensional problem as well as depends on several parameters, to reduce the complexity, we will limit the tip as a point mass spring which is a vertical oscillator to the sample [11]. Therefore, the equation of motion can be expressed as –

$$m\ddot{z} + \frac{m\omega_0}{Q}\dot{z} + kz = F_{ts} + F_{exc} \quad (17)$$

where  $F_{exc} = F_0 \cos(\omega t)$  is the excitation signal for the cantilever support and the other parameters are similar to the AM-AFM method. Eq. (6) is exactly same as the Eq. (2) except for the excitation function ( $F_{exc}$ ). The differences between the excitation signal ( $F_{exc}$ ) of AM-AFM and FM-AFM is that for FM-AFM the  $F_{exc}$  is not a pure harmonic signal rather it is a modified controlled signal from an oscillator control amplifier that ensures a constant vibration amplitude oscillator. When the tip and sample will be engaged to each other various long- and short-range forces will act between the tip-sample gap. We use Lennard-Jones type interaction potential for short-range forces which states attractive force at a moderate distance, pass through a minimum, and then zero for large tip-sample separation distances. The Lennard-Jones potential is given by [12] –



$$U_{L-J} = -4\epsilon \left[ \left( \frac{\sigma_0}{r} \right)^6 - \left( \frac{\sigma_0}{r} \right)^{12} \right] \quad (18)$$

where  $\sigma_0$  is the characteristic length of a power-law function and  $r$  is the separation distance between tip and sample. Also, the near-contact repulsion regime can be defined by Pauli exclusion by taking into consideration of electron cloud between tip and sample, ranging from 0.5 nm [13]. Another short-range attraction phenomenon is appeared due to the van der Waals (vdW) interaction forces for a spherical tip having radius  $R$  positioned perpendicular to an infinite flat plane [12]. This force is always common and can be varied along with electromagnetic field fluctuation. The van der Waals interaction can be presented as [5,12] –

$$F_{vdW} = -\frac{AR}{6r^2} \quad (19)$$

where  $A$  is the Hamaker constant, and  $r$  is the closest separation between spherical tip and sample. If the distance between tip and sample is smaller than the intermolecular distance, then  $F_{vdW}$  can be regarded as an adhesion-type ( $F_{adh}$ ) force. However, the certain, well-defined and identical long-range force acting between tip-sample systems under a bias voltage is the electrostatic force ( $F_{ele}$ ) which can be easily understood from the concept of a parallel plate capacitor. Thus, using the energy value of a capacitor the electrostatic force can be written as –

$$F_{ele} = \frac{1}{2} \frac{\partial C}{\partial z} [V_{dc} + V_{ac} \sin(\omega_{ac}t) - V_{CPD}]^2 \quad (20)$$

where  $\partial C/\partial z$  is the capacitance gradient,  $V_{CPD}$  is the contact potential difference and  $V_{dc}$  is the dc-bias voltage. The ac-voltage  $V_{ac} \sin(\omega_{ac}t)$  at frequency  $\omega_{ac}$  has been used to modulate the field allows us to separate the  $F_{ele}$  from other force contributions. In summary, the total force ( $F_{tot}$ ) can be thought of as the summation of long-range electrostatic force, van der Waals force, and the short-range chemical bonding force or  $F_{tot} = F_{ele} + F_{vdW} + F_{chem}$ .

As discussed, these forces are responsible for the resonance frequency shift ( $\Delta f$ ) of the cantilever. For small-amplitude cantilever  $\Delta f$  is related to force through the following equation [5,9]

$$\Delta f = -\frac{f_0}{2k} \frac{\partial F_{ts}}{\partial z} \quad (21)$$

where  $\partial F_{ts}/\partial z$  is the force gradient which can lower the spring constant  $k$  i.e.  $k = k_{eff} + \partial F_{ts}/\partial z$  with  $k_{eff}$  is the effective spring constant. But for large oscillation amplitude, the above equation is not satisfied, and we have to take into account of classical perturbation theorem of a harmonic oscillator. Based on perturbation theorem, the relation between  $\Delta f$  and the average  $F_{ts}$  for a full cycle can be given by [14] (Hamilton-Jacobi formalism) –

$$\Delta f(d, k, A_0, f_0) = -\frac{f_0}{kA_0^2} \frac{1}{T_0} \int_0^{T_0} F_{ts}(d + A_0 + A_0 \cos(\omega t)) A_0 \cos(\omega t) dt \quad (22)$$

where  $\Delta f$  depends on closest separation distance ( $d$ ), spring constant ( $k$ ), cantilever oscillation amplitude ( $A_0$ ), and the free resonance ( $f_0$ ). Additionally, the  $Q$ -value of the cantilever as well as the applied bias  $V_{dc}$  are equally important for FM-AFM imaging and characterization. Variation in imaging may appear due to various alignment procedures of several parameters introduced above and for different cantilever and shape of the tip head. However, the featured identical characteristics (atomic arrangement, defects, manipulated surfaces, etc.) remain the same.

### 2.2.2.2 Experimental Operation:

We used PicoScan 5500 AFM/SPM, Agilent Technologies, customized and modified into our lab able to work under FM-AFM mode. Fig. 2.8 shows a schematic diagram of our FM-AFM setup. A high-frequency oscillating cantilever oscillates near the sample surface. Due to the interaction forces, the frequency shift appeared which is detected by the PSPD. Two separate control units named as frequency control unit and amplitude control unit simultaneously detect the tip oscillation and ensure constant vibration amplitude ( $A$ ) and frequency shift ( $\Delta f$ ) of the cantilever. A preamplifier amplified the detected signal and then allows it to enter into the PLL or the frequency modulation circuit. After controlled modification, one of its components appeared as topography and another part is used to control z-feedback (Fig. 2.8). In the real situation, we introduced a phase lock loop amplifier (PLL) provided by Nanosurf into our original AFM setup which simultaneously detects the  $\Delta f$  change and provides the additional excitation signal ( $F_{exc}$ ) to control the vibration amplitude ( $A$ ) constant. A home-built feedback amplifier was used to measure the difference between setpoint

frequency and the frequency changes due to interaction forces. We also used several programable filters to ensure the lowest noise at the measurement time. The data acquisition was taken inside into a chamber where a continuous supply of dry Ar gas (99.999%) ensured the minimum humidity and contaminants inside the chamber. The whole microscope along with the chamber kept inside an isolation chamber supported by a spring to ensure the optimum vibration induced to the AFM due to other heavy apparatus (SAM, FEM/FIM) or several pumps ran inside the lab or even the earth vibration.

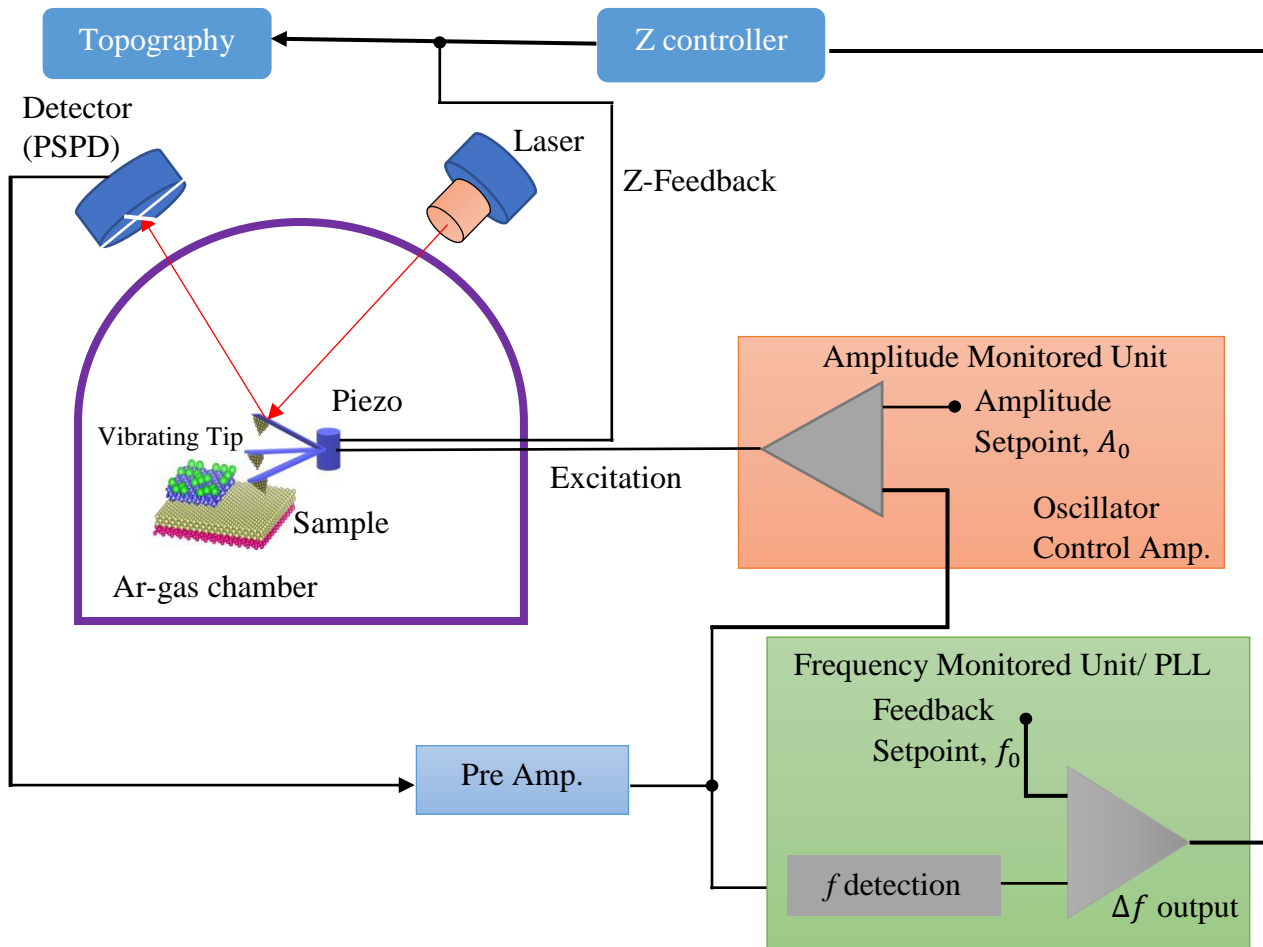


**Figure 2.8:** Schematic diagram of FM-AFM technique consists of two separate feedback units. One is an amplitude monitored unit and the other is the frequency monitored unit. Although the laser and photodetector in this block diagram are outside the environmental chamber, in real instrumentation all components (i.e., laser, detector, sample stage, scanner, and the microcantilever) are inside the chamber. As FM-AFM depends on several variable parameters discussed in the context, exact results

and imaging contrast entirely depend on the proper tuning of the FM-AFM. Of course, the unavoidable thermal drift should be considered after the measurement.

### 2.2.2.3 Conservative and Dissipative Interactions Measured by FM-AFM:

Since there exists an acute difference between AM-AFM and FM-AFM, two separate modes of nc-AFM require complete understanding which lies behind the proper knowledge of an externally driven and a self-driven oscillator which is a prime factor for both technical modes [15]. Even though both AM-AFM and FM-AFM share the same cantilever, the excitation signal ( $F_{exc}$ ) is different for both cases. For AM-AFM the excitation signal ( $F_{exc}$ ) is a purely harmonic ac-signal (with a fixed amplitude  $A_{exc}$  and frequency  $\omega_0$ ) commonly known as an externally driven cantilever whereas modified ac-signal with variable gain ( $g$ ) is used for FM-AFM or is the typical self-driven cantilever. This modification for self-driven cantilever has been done through a positive feedback system that ensures constant resonance of the oscillator [15]. In other words, in an FM-AFM mode, the excitation amplitude ( $A_{exc}$ ) of an ac-signal may vary to keep the vibrating amplitude ( $A$ ) constant [16]. Recalling the equation of motion under the active feedbacking system (Eq. 17) which is slightly different from Eq. (13), can be written as –

$$m\ddot{z}(t) + \frac{m\omega_0}{Q}\dot{z}(t) + kz(t) = F_{ts}(t) + gkz(t - t_0) \quad (23)$$

Where all the parameters carry the same meaning to that of Eq. (17) except the gain factor ( $g$ ) and the retarded time ( $t - t_0$ ) that has been introduced by an automatic gain control (AGC) unit. In Fig. 2.9, a positive feedback assembly with an AGC unit has been displayed [9].

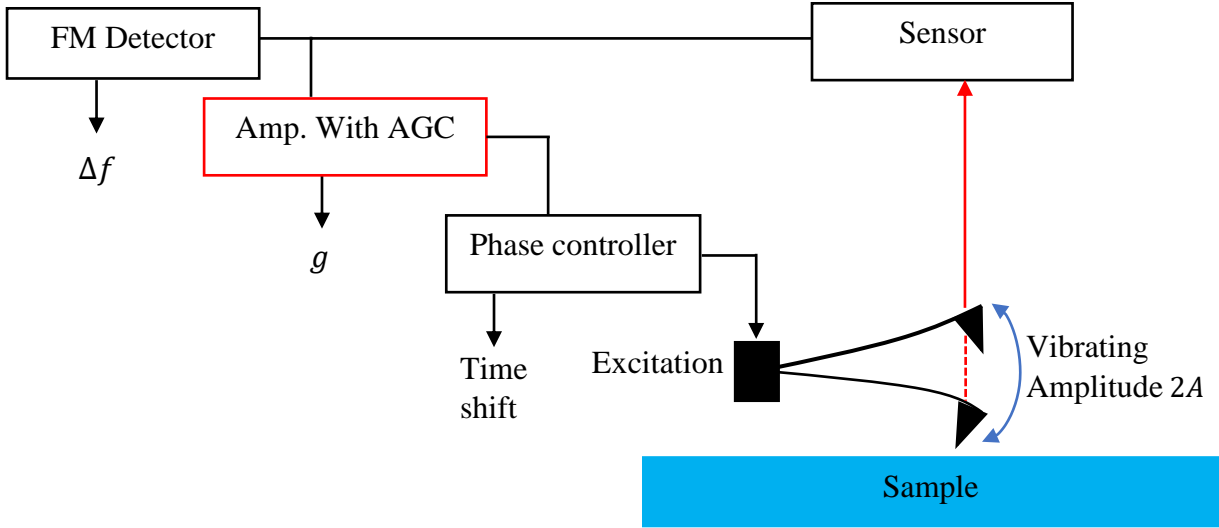


**Figure 2.9:** Block diagram of constant amplitude FMAFM using a positive feedback circuit.

Another important feature of FM-AFM is that it can measure the energy dissipation simultaneously with the frequency shift ( $\Delta f$ ) of the cantilever. From the behavior of a self-driven oscillator when it is far from sample i.e.,  $F_{ts} = 0$  in Eq. (12), oscillatory solution such as  $z(t) = z_0 + A \cos(2\pi f t)$  is permissible. By putting this solution into Eq. (12) and assuming the time ( $t_0$ ) shift set to negative

$$t_0 = \frac{T_0}{4}, \frac{3T_0}{4}, \frac{5T_0}{4}, \dots \dots \dots \quad (24)$$

$$= 90^\circ, 270^\circ, 450^\circ, \dots \dots \dots$$

(where  $T_0 = 1/f_0$  is the free oscillation period) we find that the cantilever exactly oscillates at its eigenfrequency ( $f_0$ ) and the gain factor ( $g$ ) depends only on the  $Q$  value of the cantilever. This exceptional bright characteristic allows us to find what will happen if the time (or phase) shift ( $t_0$ ) slightly deviates from those appropriate values or what else happens under tip-sample interaction ( $F_{ts}$ ). Consequently, under tip-sample interaction phenomenon the set value of  $t_0$  will be detuned from Eq. (13) which will affect the resonance frequency ( $\Delta f$ ) and the gain factor ( $g$ ) of the cantilever, also shown by several numerical simulations [16,17]. However, a brief analysis finds the FM-AFM experimental results follows mainly the  $F_{ts}$  and slightly on time shift ( $t_0$ ) [15]. In this scenario,  $\Delta f$  and  $g$  can be given by –

$$\Delta f \cong -\frac{f_0^2}{Ak} \int_0^{1/f_0} F_{ts}(t) \cos(2\pi f_0 t) dt \quad (25)$$

$$|g| \cong \frac{1}{Q} + \frac{2f_0}{Ak} \int_0^{1/f_0} F_{ts}(t) \sin(2\pi f_0 t) dt \quad (26)$$

This two-equation is the representation of conservative and dissipative force interactions that simultaneously occurred in an FM-AFM experiment. Since any exceptional assumptions did not consider for these equations which concludes the validity to use these for all types of interactions as long as the oscillation of the cantilever remains sinusoidal. In terms of the Furrier series for a periodically oscillating force ( $F_{ts}$ ) [11], Eq. (15) is a quadrature component of Eq. (14). Therefore, in summary, an FM-AFM can measure the conservative and dissipation interactions of a tip-sample system by in-phase and 90° out-of-phase detection technique.

#### 2.2.2.4 Imaging with our FM-AFM setup:

Therefore, after gathering adequate and proper knowledge, we used our customized FM-AFM setup briefly described above for imaging and surface characterization. As this research project is purely related to some modification of FM-AFM as well as characterization of 2D materials related to FM-AFM, more recorded data with constructive discussion will be presented in the next chapter. Here, we will focus only on the imaging that was taken by our FM-AFM. For that purpose, we used mica (phlogopite) affixed Ir-coated Si substrate as a test sample, equally be used as the main sample for the other electrical and mechanical surface characterization. In Fig. 2.10 (a), we took an image of a mica nanosheet that has been pasted on an Ir coated Si substrate. We found the height of the thin mica nanosheet to be 4nm, 5nm, and 6nm (Fig. 2.10b and c) corresponding to 4– layer, 5– layer, and 6– layer, respectively. We followed an exfoliation procedure that will be briefly discussed in chapter 3. The data was taken for  $10 \times 10 \mu\text{m}^2$  using  $512 \times 512$  points/line. The imaging was done for Si cantilever coated with Ir ( $f_0 = 323 \text{ kHz}$ ,  $k = 26 \text{ Nm}^{-1}$ ,  $A = 33 \text{ nm}$ ) with a constant detuning of  $\Delta f = -60 \text{ Hz}$ . Point dust that appeared on the mica is probably due to air cleaving property.

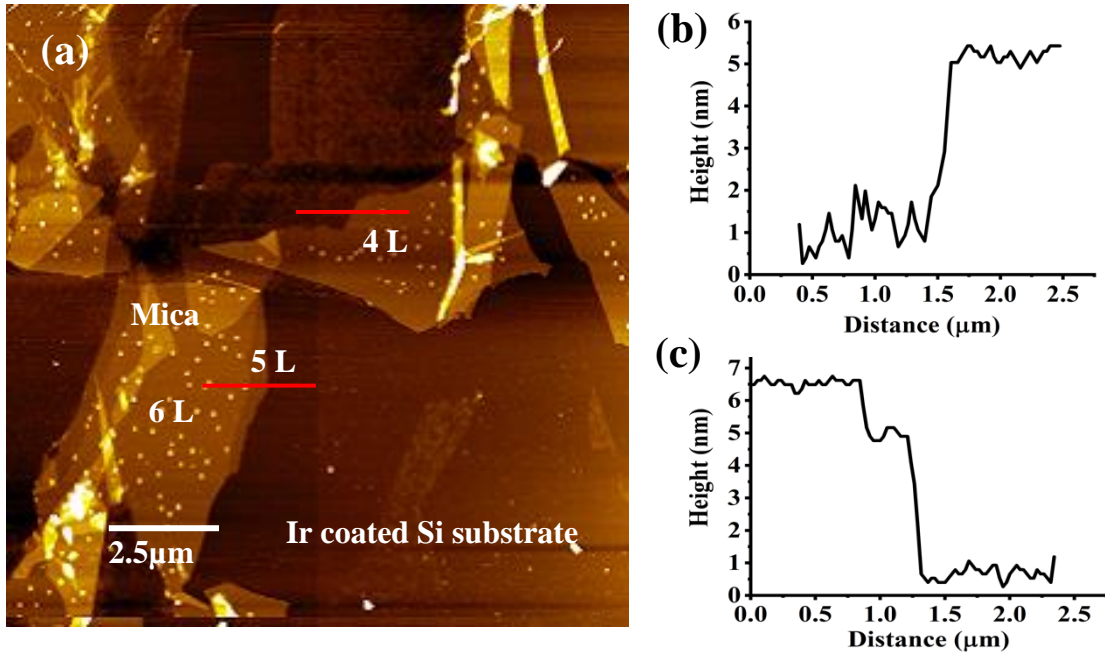


**Figure 2.10:** (a) Mechanically exfoliated mica nanosheet affixed on Ir-coated Si substrate. The corresponding mica height (b) 4-layer (or 4L in topography); (c) 5- and 6-layer (or 5 L and 6 L) measured across the red line profile. The resonance frequency shift  $\Delta f = -60$  Hz.

Using another set of Si cantilever ( $f_0 = 300$  kHz,  $k = 42$  Nm $^{-1}$ ,  $A = 22$  nm, OMCL-AC160TS-C2/C3, OLYMPUS, Japan) we also imaged mica affixed Ir-coated Si substrate and check the reproducibility of our technique which is shown 2.11 (a). Simultaneous, dissipation mapping is also shown in 2.11(b). From the topography 9 L, 10 L (sandwiched layer), and 11L have been confirmed as well as an inverted dissipation image possibly due to cross-talk of tip motion mentioned previously in [18,19]. However, we used our UV Ozon cleaner (NL-UV253, Filgen, Inc., Nagoya, Japan) to clean the sample after preparation which results in a clean surface confirmed from the topography.

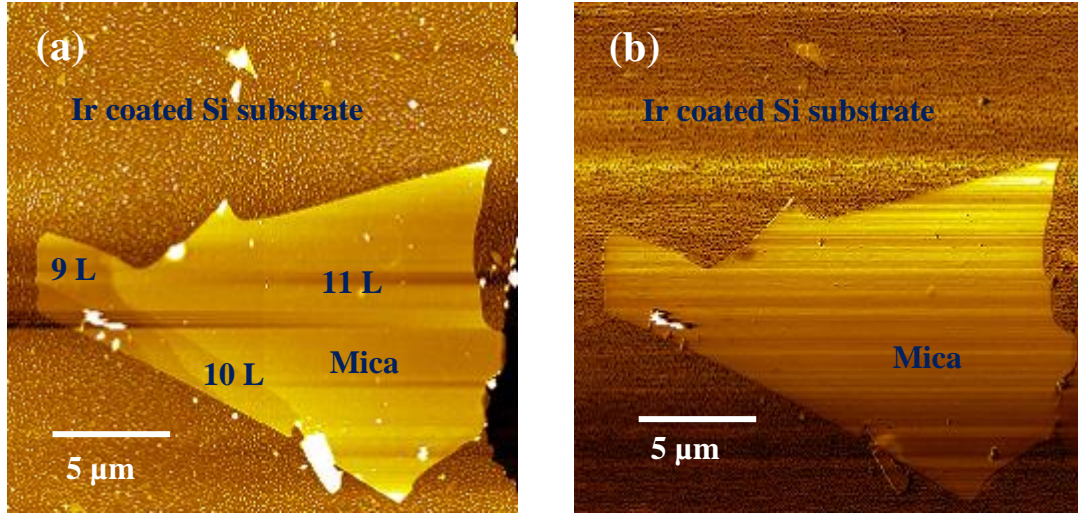


**Figure 2.11:** (a) Simultaneous measurement of 9L, 10L, and 11L mica nanosheet (a) topography; (b) dissipation. The scanning area was  $20 \times 20 \mu\text{m}^2$  and performed with a Si tip with  $\Delta f = -45 \text{ Hz}$ . Inverted dissipation is due to the cross-talk of the tip motion.

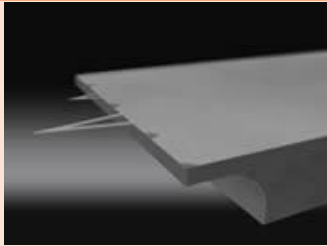
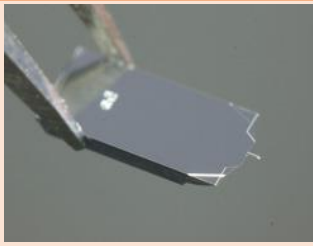
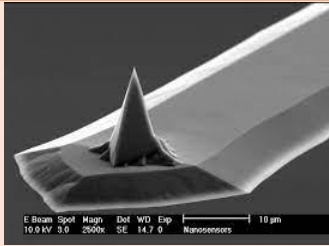
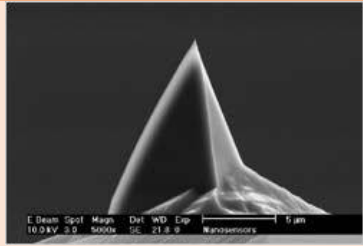
In summary, we found the imaging contrast and the tip-induced damping or the artifacts strongly depend on the shape of the cantilever as well as the tuning of the PLL with the varying targeted  $\Delta f$ . It is recommended that performing several electrical and mechanical characterization would be more accurate under the same target  $\Delta f$  and the same cantilever.

## 2.3 Cantilever Specifications:

As mentioned previously that the image acquisition and several nanomechanical characterizations of the sample surface strongly depend on the shape of the tip and the cantilever materials. In other words, the tip along with the cantilever is the core heart of any AFM measurements. The prime features that should take into consideration before purchasing any commercial cantilevers are the cantilever materials (conductive/ non-conductive), tip radius ( $r_{\text{tip}}$ ), stiffness ( $k$ ), mechanical quality factor ( $Q$  value), eigenfrequency ( $f_0$ ), hardness and thermal stability  $\partial f_0 / \partial T$ . Depending on the mode of operation (contact, tapping, or non-contact) various precise monolithic cantilevers are available commercially. We frequently used four types of cantilevers for taking data which are categorized as (i) PNP-TR-Au (contact mode); (ii) OMCL-AC160TS-R3 (tapping mode), (iii) PtIr-NCH, and (iv) PtSi-NCH (non-contact mode). All of those show almost equal results for our measurements taken at different times. Their features have been summarized in the following table –



**Table 2.1:** The following table consists of cantilevers specifications and its manufacturer. Photos are directly taken from OLYMPUS and NANOSENSORS's official web pages:

Cantilever Model	PNP-TR-Au	OMCL-AC160TS-R3	PtSi-NCH	PtIr-NCH
Operation Mode	Contact	Tapping	Non-contact	Non-contact (EFM)
Tip	Gold-coated (~35nm) Pyrex Nitride	Silicon Tetrahedral Tip	Platinum Silicide	Platinum Iridium
Stiffness ( $k$ )	0.32 N/m 0.08 N/m	20–26 N/m	40–42 N/m	10–130 N/m
Eigenfrequency ( $f_0$ )	67 kHz 17 kHz	300 kHz (Typically)	288 kHz (Typically)	265 kHz (Typically)
$Q$ -value (in air)	—	300–350	340–380	400–600
Manufacturer	NANOSENSORS	OLYMPUS	NANOSENSORS	NANOSENSORS
Image				

Additionally, using different types of cantilevers simultaneously allowed us to find out the best performance cantilever. According to our experiences, we found both the conductive PtSi and PtIr-NCH probe (highlighted in the table) is the best for conducting an FM-AFM experiment.

## 2.4 Additional Apparatus:

### 2.4.1 Optical Microscope:

We frequently used an optical microscope for sample preparation and purity check of the substrate. As we followed the exfoliation process for sample preparation, using a highly precision optical microscope allowed us to see the initial deposition of the sample on the substrate. Therefore, we used Axis Pro-2 optical microscope [20] provided by Nikon, Japan which is typically a micromanipulation system shown in Fig. 2.12. It is a combination of a well-organized light microscope and highly appropriate manipulation tools.



**Figure 2.12:** Axis Pro-2 manipulator assembled with a dedicated pre-installed computer for accurate manipulation [20].

Using this Axis Pro-2 user can easily manipulate small particles ( $\mu\text{m}$ -size) from one sample to another sample within a very short time ( $\sim$ few minutes). The whole system is operated by a dedicated computer where Axis Pro-2 software has been installed. Using this software, we can make a  $0.91\times - 10\times$  optical zoom to observe very little ( $\text{nm}$ -size) area. Our Axis Pro-2 is also equipped with Nikon

ECLIPSE 3X2 stage which allows us easy handling both manually and digitally for manipulation as well as imaging. A 46.2mm optical zoom lens was used for imaging.

### **2.4.2 DC Magnetron Sputter (E-1030):**

The DC magnetron Sputter (E-1030, HITACHI-High tech., Japan) is a sample coating instrument, typically used for coating substrate with various types of metal, for example, Pt, Au, Ir, Pt-Pd, Au-Pd, etc. to investigate samples under atomic force microscopy (AFM), scanning electron microscopy (SEM), or scanning Auger microscopy (SAM) setup. This sputtering method not only assures conductive sample surface after coating but also provides charge neutrality which is a prerequisite before introducing the sample inside the above-mentioned microscopy technique. The thickness of the coated can be controlled from few nanometers to tens of nanometer depending on the instruction's manual provided by the company (See Table 2.2 and 2.3). Besides, E-1030 also uses a magnetron electrode meaning that a negatively biased target, integrated with a magnetic field to generate a perpendicular magnetic field concerning the electric field of the target. This magnetic field ensures plasma in a more restricted position and makes the deposition more uniform on the substrate. In Fig. 2.13 (a) a top view schematic is shown. The main unit is assembled with an Ar-gas supply tank and an oil pump to create a vacuum. In the middle of the main unit, there is a sample stage and on the top of the stage, a target exists. Under high electric potential difference between a substrate (positive bias) and the target (negative bias), highly accelerated Ar-plasma can dislodge the atom from the target and deposits it on the substrate. The E-1030 DC sputter that exists in our lab used for several purposes is shown in Fig. 2.13 (b). Two other available options are also present i.e. (i) etching, and (ii) hydrophilizing. The sputtering, etching, and hydrophilizing operation, time, target height, current, and Ar gas pressure have been summarized in Tables 2.2 and 2.3.

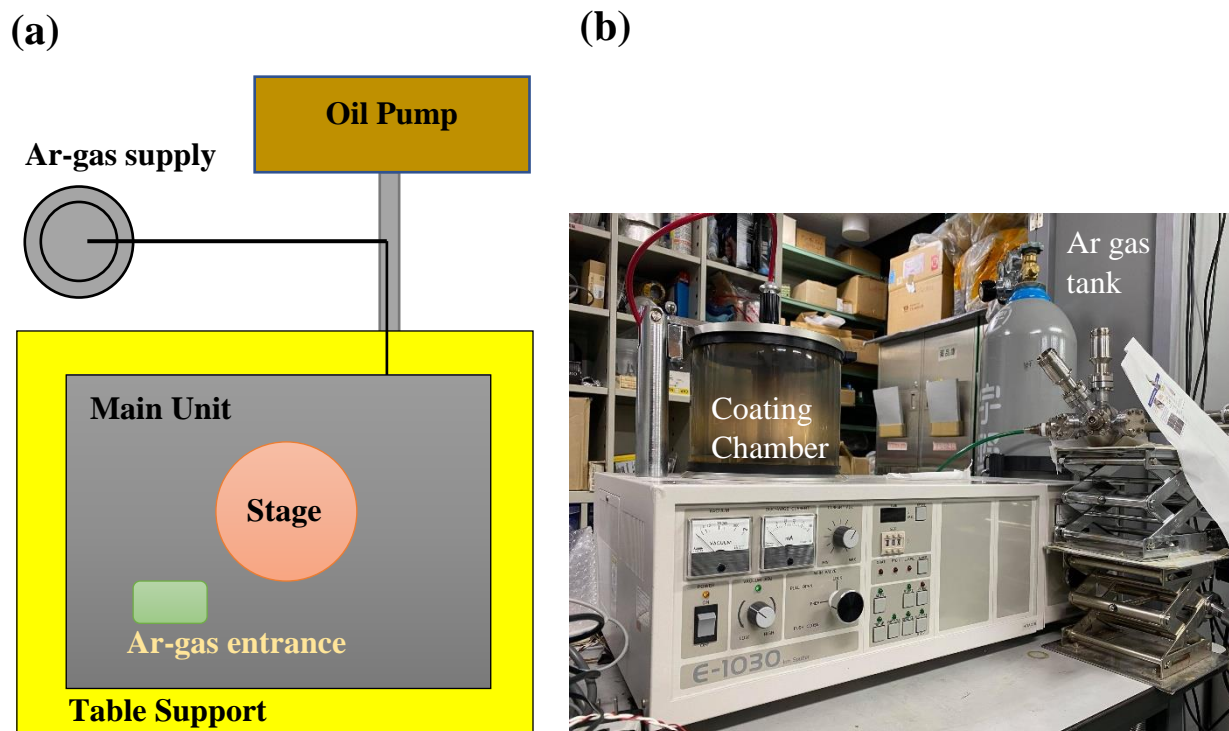


**Figure 2.13:** (a) Schematic diagram of E-1030; (b) Commercially available model (E-1030), directly taken from our experimental lab.

**Table 2.2:** Three especial operational modes that E-1030 can perform for sample preparation:

Operation	DC/AC	Mode	Target Height (mm)	Current (mA)	Time (typical) sec	Ar-gas Pressure (Pa)
Sputter	-	Coat	30	15	See table 2.3	6
Etching	DC	Etch	30	15	100	6
Hydrophilizing	AC	Etch	20	5	30-80	6

**Table 2.3:** Sputtering deposition rate (nm/min) of E-1030:

<b>Target</b>	<b>Sputter Rate (nm/min)</b>
<b>Pt-Pd</b>	<b>6.0</b>
<b>Pt</b>	<b>6.0</b>
<b>Au</b>	<b>11.5</b>
<b>Ir</b>	<b>12.0</b>
<b>Au-Pd</b>	<b>8.8</b>

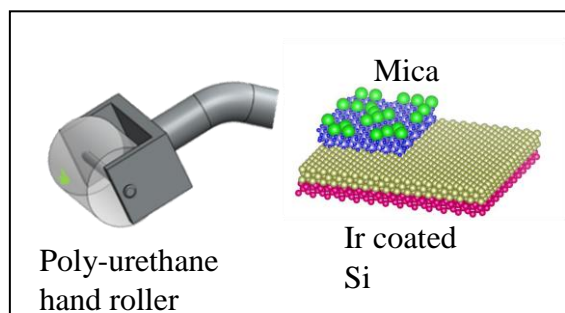
## References:

- [1] G.Binnig, C.F. Quate, Ch. Gerber, *Phys. Rev. Lett.* 56 (1996) 930–933.
- [2] F.J. Giessibl, *Rev. Mod. Phys.* 75 (2003) 949–983.
- [3] F.J. Giessibl, *Appl. Phys. Lett.* 78 (2001) 123–125.
- [4] E. Meyer, S. Morita, R. Wiesendanger, *Noncontact Atomic Force Microscopy* (2002).
- [5] R. García, R. Pérez, *Surf. Sci. Rep.* 47 (2002) 197–301.
- [6] W. Melitz, J. Shen, A.C. Kummel, S. Lee, *Surf. Sci. Rep.* 66 (2011) 1–27.
- [7] Y. Martin, C.C. Williams, H.K. Wickramasinghe, *J. Appl. Phys.* 61 (1987) 4723–4729.
- [8] Q. Zhong, D. Inniss, K. Kjoller, V.B. Elings, *Surf. Sci. Lett.* 290 (1993) L688–L692.
- [9] T.R. Albrecht, P. Grütter, D. Horne, D. Rugar, *J. Appl. Phys.* 69 (1991) 668–673.
- [10] U. Dürig, H.R. Steinauer, N. Blanc, *J. Appl. Phys.* 82 (1997) 3641–3651.
- [11] S. Sadewasser, T. Glatzel, *Kelvin Probe Force Microscopy* (2018).
- [12] J.N. Israelachvili, *Intermolecular and Surface Forces* (1954).
- [13] I. Štich, J. Tóvik, R. Pérez, K. Terakura, S.H. Ke, *Prog. Surf. Sci.* 64 (2000) 179–191.
- [14] F.J. Giessibl, *Phys. Rev. B* 56 (1997) 16010–16015.
- [15] B. Gotsmann, W. Allers, H. Hölscher, U.D. Schwarz, R. Wiesendanger, H. Fuchs, *Phys. Rev. B* 64 (2001) 075402–075408.
- [16] B. Gotsmann, C. Seidel, B. Anczykowski, H. Fuchs, *Phys. Rev. B* 60 (1999) 11051–11061.
- [17] B. Gotsmann, B. Anczykowski, C. Seidel, H. Fuchs, *Appl. Surf. Sci.* 140 (1999) 314–319.
- [18] T. Arai, R. Inamura, D. Kura, M. Tomitori, *Phys. Rev. B* 97 (2018) 115428–115434.
- [19] C. Loppacher, R. Bennewitz, O. Pfeiffer, M. Guggisberg, M. Bammerlin, S. Schär, V. Barwich, A. Baratoff, E. Meyer, *Phys. Rev. B* 62 (2000) 13674–13679.
- [20] <https://mountainphotonics.de/products/mis-axis-pro/?lang=en>.

## Chapter 3:

### Experimental Methods for Sample Preparation and Evaluation

Our earth is naturally abundant with numbers of layered materials which have been investigated for more than 100 years for searching the potential one along with its extraordinary properties down to small scale as well as its proper application to our modern electronic devices [1,2]. Using some limited but appropriate techniques, these layered materials can be sliced down to two-dimensional (2D) thin sheets typically called 2D materials/ 2D nanosheets under some minimum applicable physical limits [3]. In this chapter, we will represent an exfoliation technique and transfer process through which we made an atomically thin mica nanosheet and pasted it on Iridium (Ir) coated Si substrate (Ir/Si). We used artificially synthesized phlogopite mica ( $\text{KMg}_3\text{AlSi}_3\text{O}_{10}\text{F}_2$ ), another prominent 2D material, which shows cleaving property and is commonly used as a substrate material (both muscovite and phlogopite) for many fundamental experiments [4,5].



### 3.1 Introduction

After revealing the unusual unique properties of 2D thin nanosheets varying from that of bulk crystals, sequential research has been done over the last few years to utilize the intense and potential electrical and mechanical characteristics of 2D nanosheets [3]. Besides, recently invented additional quantum features related to the dimensionality of 2D materials [6–9], for example, 2D superconductivity, quantum transportation [10–13], magnetism, high carrier mobility [14], etc. have expanded the field of interest. The primary application and acceleration of this field became initiated after the invention of graphene which is typically a single hexagonal array of carbon atoms isolated from that of bulk graphite [14,15]. Graphene serves as a basic building block of carbon-related materials i.e., the well-known three-dimensional (3D) graphite, one-dimensional (1D) nanotubes, and

zero-dimensional (0D) fullerene [16]. Moreover, it was the first ultra-thinned 2D nanosheet that provided a novel transition for materials and devices from microscale to atomic-scale and related physics responsible for distinct electrical [17,18], mechanical [19], optical [20], and sensing properties [21] to understand the phenomenon exhaustively. Therefore, within a very short period, various electronic and optoelectronic devices considered graphene as an effective performer to fabricate a high-frequency transistor [22,23], active solar cells [24–26], logic gates [27], and CMOS devices [28]. Since 2D graphene (monolayer to several layers) established itself as a successful candidate, continuum research finds other effective and distinctive 2D materials such as MoS<sub>2</sub> [29], MoSe<sub>2</sub> [30], WS<sub>2</sub> [31], WSe<sub>2</sub> [32], h-BN [33], polymers, fibrous materials, thin glass plates, metallic foil, black phosphorous, and so on [34]. Among those 2D materials MoS<sub>2</sub>, MoSe<sub>2</sub>, WS<sub>2</sub>, and WSe<sub>2</sub> are also known as transition-metal dichalcogenides or TMDs materials.

However, a newly emergent another fascinating 2D material from the phyllosilicate subgroup called Mica could be compatible with the above-mentioned 2D materials. Mica is established as a layered silicate compound with properties varying from conductor to semiconduction depending on the thickness [5], it is used as an insulating material in the industry, home appliances (hot plates, toasters, and irons, etc.), and a dielectric in a capacitor, and so many. Besides, ground mica is also used for roofing, waterproof fabrics, and various agricultural products [34]. From this point of view, the importance of mica is enormous which can be expanded into the nanoscale. Consequently, a large number of the present research is now focused on mica regarded as 2D substrate materials as well as the thin dielectric layer that can play an important role for modern electronic devices. Even though the structural analysis was reported in the 1920s [35], very few details about the behavior of mica down to nanoscale are known at present. Depending on the unit cell formula i.e.  $X_2Y_nZ_8O_{20}(OH, F)_4$  where X represents cations ( $K^+$ ,  $Na^+$ ,  $Ca^+$ ), Y represents octahedral elements ( $Al^{3+}$ ,  $Mg^{2+}$ ,  $Fe^{2+}$ ,  $Li^+$ , ...) and Z represents the tetrahedral elements ( $Si^{4+}$ ,  $Al^{3+}$ , ...), mica further can be categorized as muscovite [ $KAl_2(Si_3Al)O_{10}(OH)_2$ ], phlogopite [ $KMg_3AlSi_3O_{10}F_2$ ], biotite [ $K(Mg, Fe)_3(AlSi_3O_{10})(F, OH)_2$ ], etc [34].

As this present research is related to artificially synthesized phlogopite mica, therefore, we will briefly discuss the featured characteristics and exfoliation process of phlogopite mica. Moreover, phlogopite is one of the cleavable mica with a bandgap of ~9 eV and a perfectly cleavable (001) basal plane. Also, the operating temperature of artificially synthesized pure phlogopite (~1000 °C) is higher than that of widely used muscovite mica (~500 °C). Figure 3.1 (a) and (b) show the side view and top



view of atomic phlogopite mica. The  $K^+$  ion (purple solid sphere in Fig. 3.1 b) is confined in between the hexagonal array pattern of  $SiO_4$  atoms after exfoliation. The basic building block i.e., the tetrahedral layer (T-layer)  $[(Si, Al) + O_2]$  and octahedral layer (O-layer)  $[(MgO) + F]$  make T-O-T sandwiched layer which is connected with another T-O-T layer to make bulk mica through interlayer ( $K^+$ ) cations. This weak bonded  $K^+$  layer is considered as the cleavable plane and allows us to make ultra-thin mica 2D nanosheet.

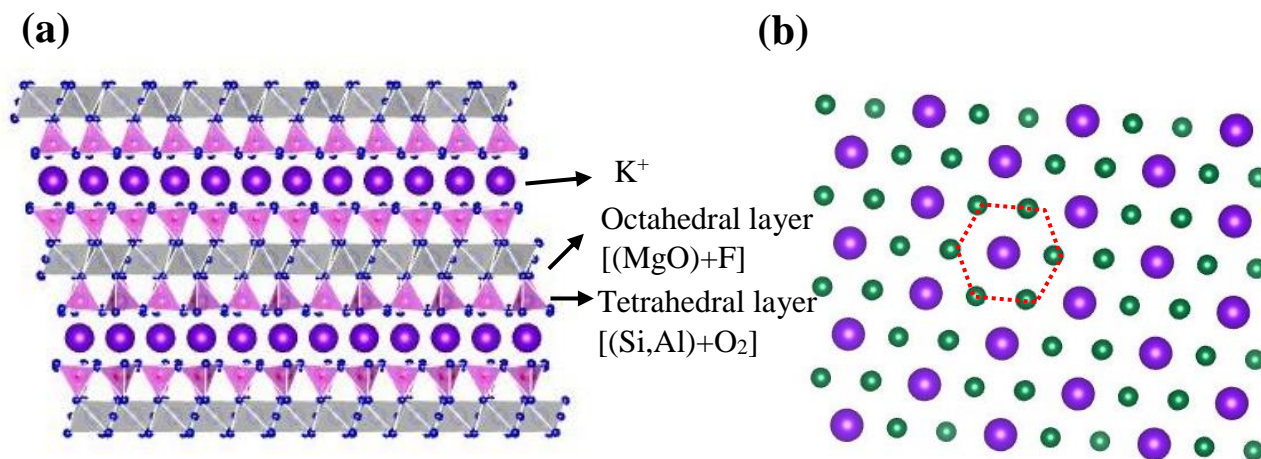


**Figure 3.1:** Atomic structure of phlogopite mica (a) side view; (b) top view. The tetrahedral layer  $[(Si, Al)+O_2]$  and octahedral layer  $[(MgO)+F]$  are shown by pink and gray polygon, respectively, considered as the main structural frame of mica.

However, the application of this mica nanosheet entirely depends on its successful exfoliation process and exfoliated area. Various conventional methods have been applied for receiving defect less, and high atomically flat large areas of mica. In the next section, we will represent a newly developed exfoliation process for artificially synthesized phlogopite through which a clean and large area of mica nanosheet can be prepared.

## 3.2 Mechanical Exfoliation:

It has been found that only specifying absolute layered bulk materials has no meaning without knowing its proper exfoliation and/or growth process to make an ultra-thin layer for device fabrication. As a result, the useable identical physical properties of 2D materials largely depend on their synthesis and growth process. From time to time, even if it is possible to make ultra-thin 2D nanosheets using conventional techniques, features that we need (uniformity, flexibility, tunable bandgap, etc.) always ends up with extreme challenges using those techniques. Although using the crystal growth technique, it is possible to make a large-area single crystal of some 2D materials (for example, graphene and h-BN), however, scalable growth is still an obstacle for us [36], especially for the heterostructure 2D materials. Note that, some scalable growth techniques, for example, atomic layer deposition and chemical vapor deposition (CVD) have been employed to produce large-area TMDs materials ( $\text{MoS}_2$  [37,38],  $\text{WS}_2$  [39]), and others [40] on different substrates, but the CVD optimized growth approaches often been proven to be a time-consuming process since abrupt occurrences such as the formation of defects [41] and grain boundaries happened simultaneously with the growth process.

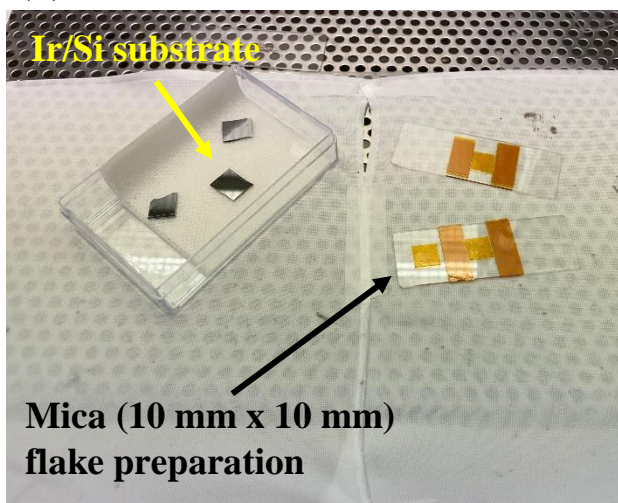
For more than the last 15 years, the mechanical exfoliation process takes the attention for making thin to thick 2D layered materials with the marginal area [42]. Even though these 2D nanosheets with exfoliation techniques inevitably show randomness with dimensionality and structure, some notable intrinsic properties (superconductivity [43], Hall effect [18], massless Dirac Fermions [17]) play a significant role which is absent in CVD or other growth techniques. Therefore, to prepare any 2D flat sheet from their mother crystal with varying thickness, the mechanical exfoliation process is suitable beyond any other growth or deposition process.

### 3.2.1 Experimental Methods to Prepare Large Area High-Quality Mica Nanosheet:

With the comparison to that of conventional scotch tape method widely used for the exfoliation process of graphene and other 2D materials, we adopted an exfoliation process with a tool named as polyurethane hand roller for preparing mica nanosheet from bulk mica and then affixed it onto the Ir/Si substrate. A commercially available clean polyurethane hand roller (Semiconductive gel roller, EX215-AS, EXSEAL Co., Ltd., Mino, Japan) with a diameter of 20 mm is used for the exfoliation

process which is originally recognized as a dust removal instrument from flat surfaces in semiconductor processes without having residues. One of the easily observable advantages of using a polyurethane hand roller is that it provides a similar type of viscosity to that of poly-dimethyl siloxane (PDMS) or scotch tape with a lower level of residues. Experimental procedures of the mechanical exfoliation process and affixing techniques are shown in Fig. 3.2 (a – g). At first, we attached our bulk clean mica flake to a glass slide (Fig. 3.2a) using adhesive scotch tape (polyimide film, both side Silicon adhesive, heat resistant tape). Additionally, we cut the n-type Si (111) (resistivity 0.4 – 0.9  $\Omega\cdot\text{cm}$ ) wafer to make Si substrate to our preferred shape and coated it with Ir using DC magnetron sputtering machine. In Fig. 3.2 (b) the commercial polyurethane hand roller (diameter 20 mm) is displayed. Our exfoliation technique is shown in Fig. 3.2 (c) where we roll the roller once at a time with moderate force on it over the top surface of the bulk mica to thinly exfoliate the surface. Therefore, due to the adhesive property of the roller as well as the cleaving property ([001] basal plane) of mica, some broken exfoliated mica sheets were attached (Fig. 3.2d) to the surface of the roller. At the same time, we carefully used a very little amount of water (spray type) (Fig. 3.2e) to weaken the adhesion property between mica and roller. Consequently, the roller was rolled over the Ir/Si substrate to transfer the mica broken sheets to the targeted area on the substrate shown in Fig. 3.2 (f). The curvature of the roller allows us to easily separate the thin mica sheets from both the bulk mica surface and to shift them onto the Ir/Si substrate. At this stage, we heated the sample at 200°C for 30 minutes in the air using a conventional ceramic hotplate to remove water molecules from the sample surface. Before performing all of the above-mentioned procedures, the SiO<sub>2</sub>/Si substrate was cleaned ultrasonically in acetone, and mill-Q water. Moreover, to confirm a clean sample ozone cleaning was carried out to remove hydrocarbon adsorbates from the surface. Using the poly-urethane hand roller technique, we prepared a mica nanosheet varying from thick to ultra-thin layer. Similar results are also shown by our previous study [5]. We also assumed half of the K<sup>+</sup> atom random distribution after cleaving on the exfoliated mica nanosheets, while the other half is on the counter surface of the mica crystal. We confirmed our exfoliation results with the help of optical microscopy (Axis pro) and AFM showed satisfactory results which will be discussed in the results and discussion section. We found up to 15-layer of mica nanosheets are visible under an optical microscope and lower than this we need AFM investigation.

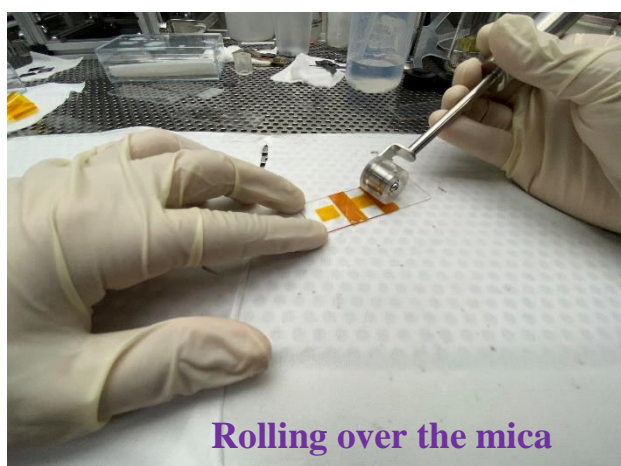
(a)



(b)



(c)



(d)





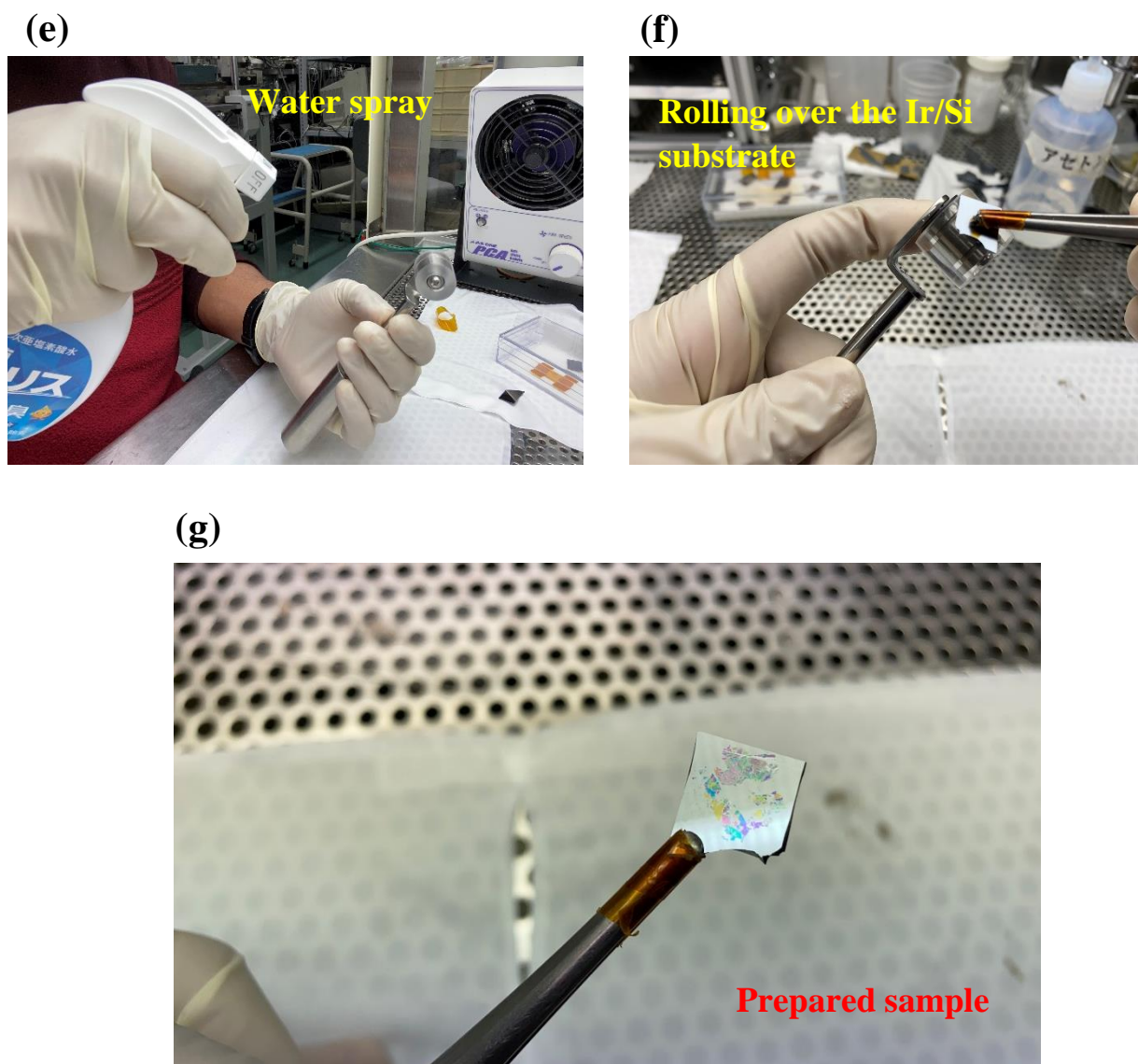


**Figure 3.2:** Mechanical exfoliation using polyurethane hand roller technique. All of the stages were performed in our lab environment with humidity ranging from 30-50%. Sequential processes: (a) prepared Ir/Si substrate for AFM holder and customized glass plate holding mica sheet for rolling, (b) polyurethane roller with preferable length and diameter, (c) real-time rolling, (d) careful observation of broken mica flake on the roller, (e) using water to lower the adhesion, (f) roll over the substrate, (g) prepared sample. Finally, before AFM measurement, additional heat treatment was performed using a ceramic hot plate.

The atomically exfoliated 3D mica nanosheet with an equal number of  $K^+$  ion distribution is shown in Fig. 3.3. Two tetrahedral layers (T-layer)  $[(Si, Al)+O_2]$  with an octahedral layer (O-layer)  $[(MgO)+F]$  in between makes a T-O-T sandwiched layer which is connected with another T-O-T layer to complete a bulk mica through interlayer ( $K^+$ ) cations. The  $K^+$  layer is considered as the (001) cleavable basal plane and allows us to make ultra-thin mica shown in Fig. 3.3.

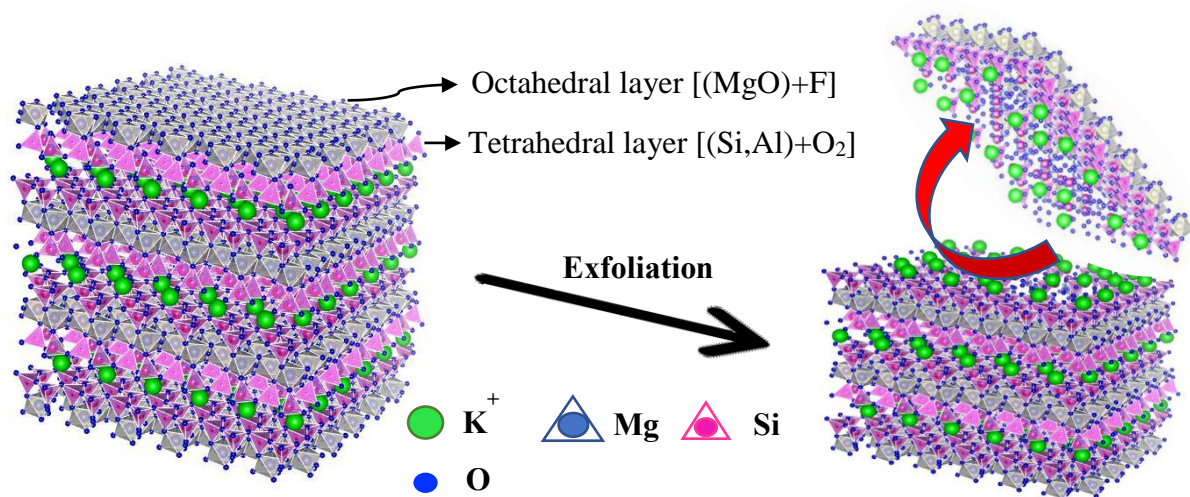


**Figure 3.3:** The atomistic 3D representation of exfoliation process of phlogopite mica using our polyurethane hand roller. The two T-O-T layers are interconnected with the  $K^+$  layer, equally considered as the cleaving plane. 1-layer of cleaved nanosheet is detached from bulk in above.

To prepare the iridium coated Si substrate (Ir/Si), we used native oxidized n-type Si (111) (resistivity  $0.4 - 0.9 \Omega \cdot \text{cm}$ ) wafer coated iridium (Ir) at a thickness of  $\sim 12$  nm deposited by DC magnetron sputtering. A schematic sputtering process is shown in Fig. 3.4. DC magnetron sputtering coat was conducted in a vacuum chamber with an Ar-gas (99.999%) pressure of 6 Pa at a discharge current of 15 mA with a DC power supply.

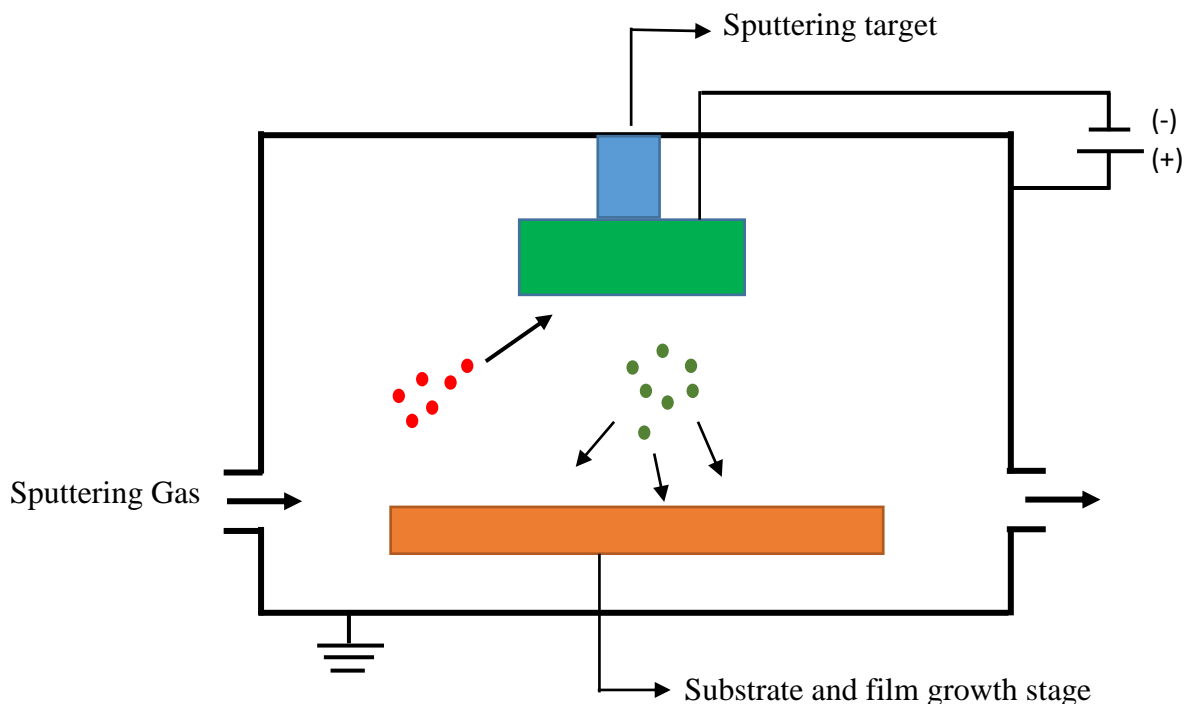


**Figure 3.4:** A schematic diagram of DC magnetron sputtering.

### 3.3 Results and Discussion:

After preparation, we first observed our sample under an optical microscope as we mentioned before that using a high-resolution optical microscope it is possible to see  $\sim 15$  nm of flat mica nanosheet on Ir/Si substrate. More than 100 nm thick mica flake even reflects different colors which are visible through our naked eyes as shown in Fig 3.2 (g). However, some optical microscopy images are presented in Fig. 3.5 where different layer thickness mica has pasted on Ir/Si substrate. We used Axis pro which has been described in chapter two (section 2.4). Through this optical microscope, we were able to observe up to  $\sim 20$  nm thick and large mica flake shown in Fig. 3.5 (a) and (d). It is also reported by one of our previous groups that mica thin nanosheet down to 1-layer is possible to observe under the optical microscope which depends on the substrate material [44]. However, for our Ir/Si

substrate, it is hardly possible to see mica nanosheets lower than 20 nm. As a result, we engaged our AFM system to analyze thin mica nanosheets.

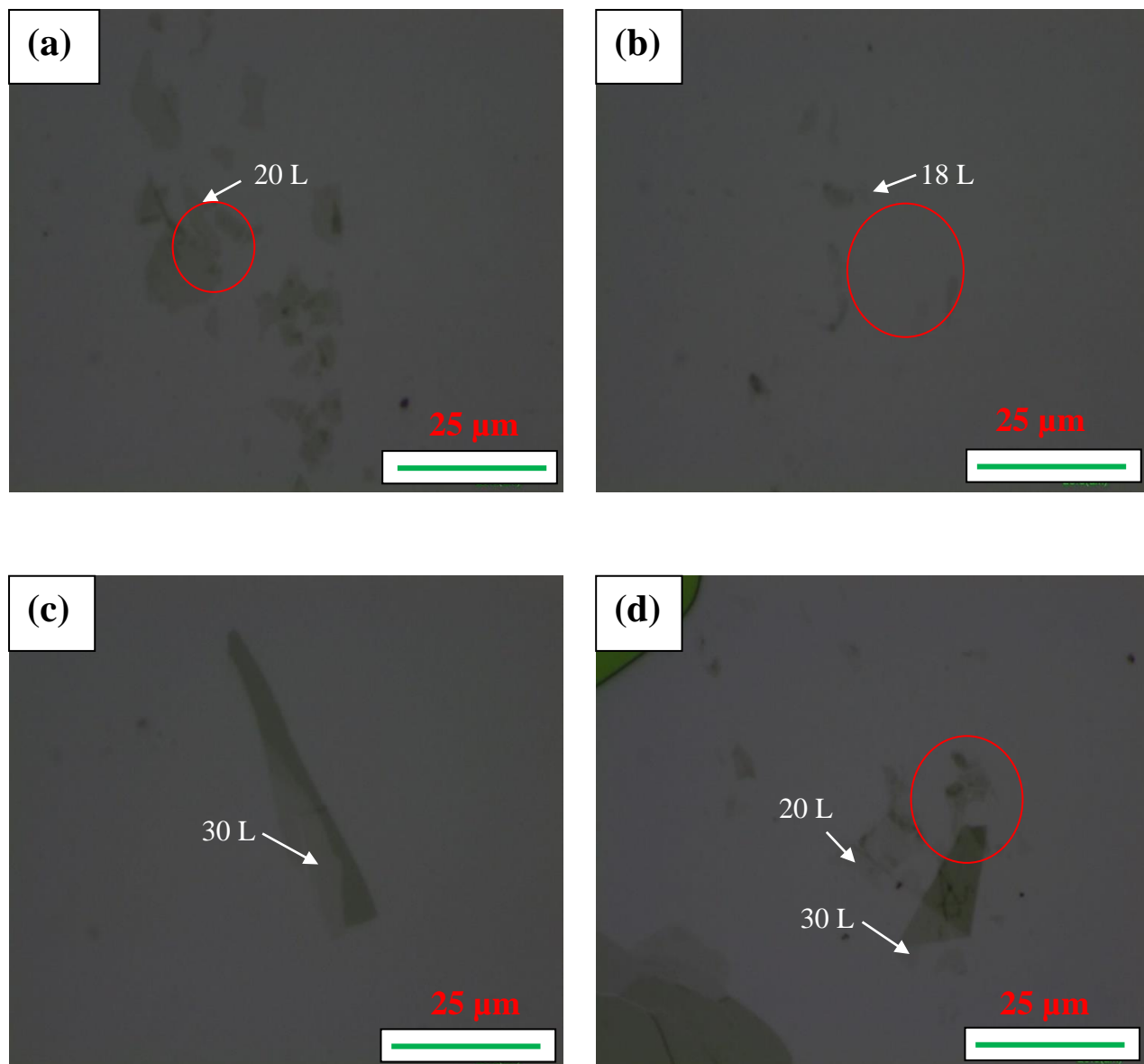
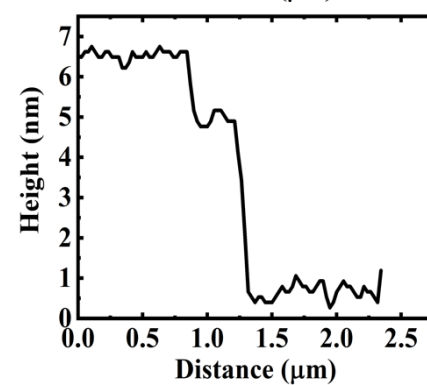
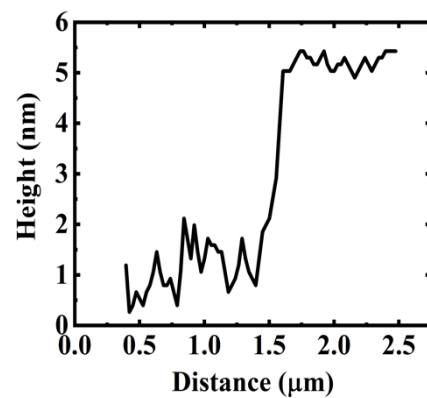
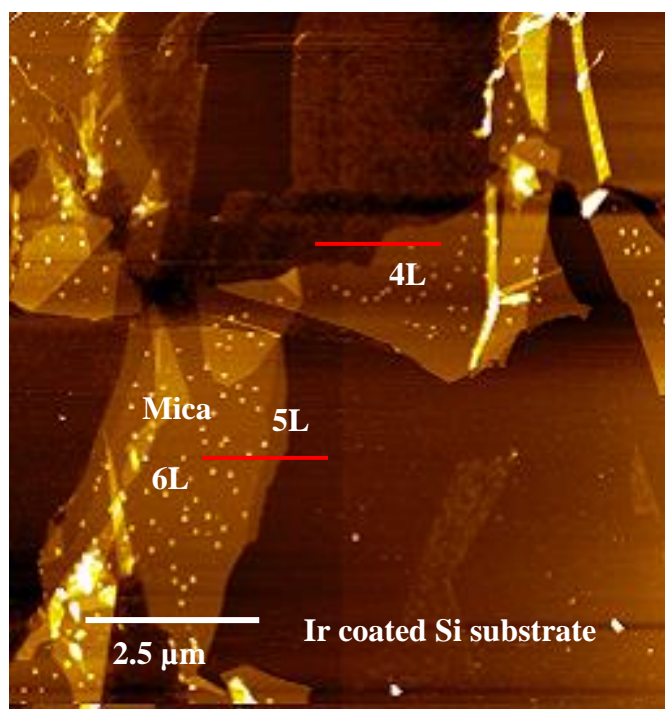


**Figure 3.5:** Optical microscopy images provided the initial mica nanosheet deposition on Ir/Si substrate. The color differences indicate the thickness of the mica layer. Almost no contrast appeared for nanosheets having height  $< \sim 20$  nm for the Ir/Si substrate. For this case, (a) shows 20 nm or 20-layer of thick mica sheet; (b) 18-layer, (c) 30-layer, and (d) 20- and 30-layer was observed. Think layer of mica nanosheet is also found on the red marked area through AFM measurement, however, no contrast is found here.

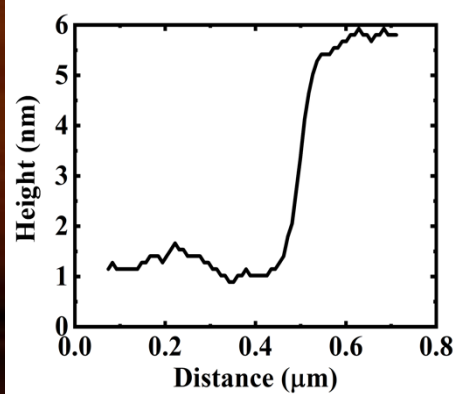
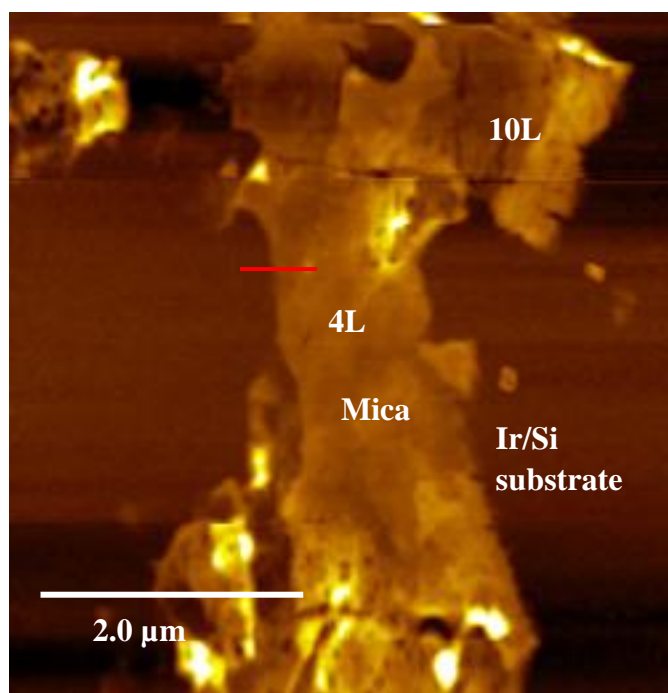


Even though the above optical images only show thick mica sheets varying from 20-layer to 30-layer, the red marked circle area contains thin mica nanosheets which have been confirmed through AFM images. In Fig. 3.6 (a) – (d), several layers of mica nanosheet varying from thin to thick layer is shown taken by contact AFM system. The initial morphology of the sample surface and the height of any thin 2D materials can be independently measured by AFM. Therefore, before performing any characterization using the frequency modulated (FM-AFM) ncAFM mode, we measured the height of the mica using contact AFM or intermittent contact mode which is relatively less time-consuming than an FM-AFM system. The height has been measured across the line profile that passes through both mica and Ir/Si substrate shown on each AFM image (Fig. 3.6 (a) – (d)). For images, (a) and (b) the line profile curves corresponding to mica height with respect to bare Ir/Si have been placed on the right side of the images, and for (c) and (d), it is on the below of the images. The minimum height between Ir/Si substrate and the mica has been measured to 4 nm, 5 nm and 6 nm shown in Fig. 3.6 (a) and (b) corresponding to 4-layer (4L), 5-layer (5L), and 6-layer (6L) of its unit thickness ( $\sim 1$  nm). Although the dimensions of thin layer mica nanosheets fabricated by other conventional mechanical processes, for example, Scotch tape method, are usually not much larger than  $1\text{ }\mu\text{m} \times 1\text{ }\mu\text{m}$ , however, we were able to prepare 4-layer mica nanosheets with dimensions of  $\sim 5\text{ }\mu\text{m} \times 5\text{ }\mu\text{m}$  (Fig. 3.6a) with a scanning area of  $\sim 10 \times 10\text{ }\mu\text{m}^2$  and  $\sim 2\text{ }\mu\text{m} \times 2\text{ }\mu\text{m}$  (Fig. 3.6b) for  $4.5 \times 4.5\text{ }\mu\text{m}^2$  using our polyurethane roller method (Fig. 3.2 (a)–(g)). The 6L of mica has also a dimension of  $\sim 5\text{ }\mu\text{m} \times 5\text{ }\mu\text{m}$  shown in Fig. 3.6 (a). The point-like dots that appeared on mica in Fig. 3.6 (a) is possibly due to the contamination of hydrocarbons as we exfoliated mica in the air. Also, from Fig. 3.6 (b) – (d) relatively clean and flat surface of mica has been found without any water ripple or less contamination layer. From Fig. 3.6 (c) and (d), the thicker 10-layer and 15-layer mica sheets have been observed with dimensions of  $\sim 10\text{ }\mu\text{m} \times 10\text{ }\mu\text{m}$  confirmed by  $\sim 40 \times 40\text{ }\mu\text{m}^2$  and  $\sim 30 \times 30\text{ }\mu\text{m}^2$  scanning area, respectively.

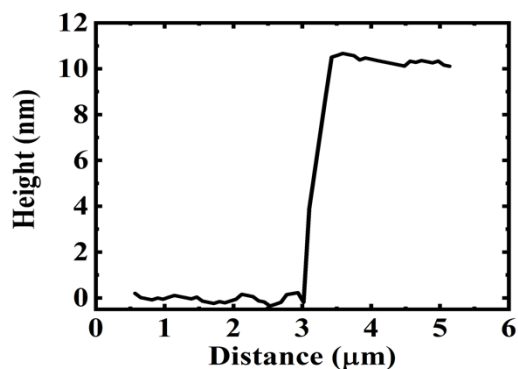
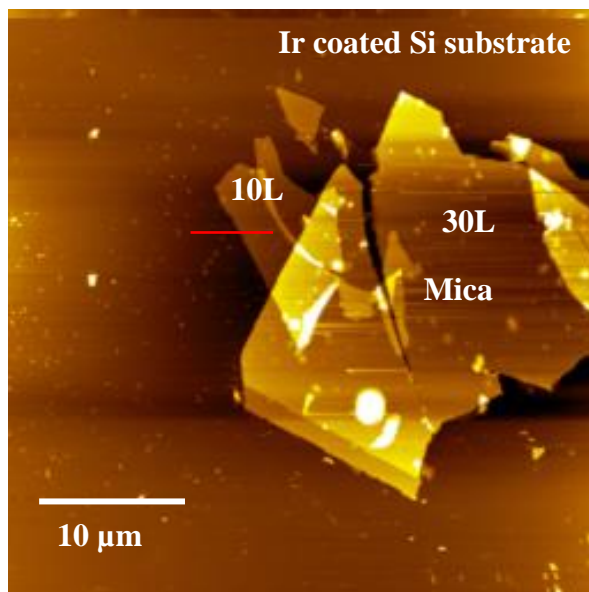
(a)



(b)



(c)



(d)

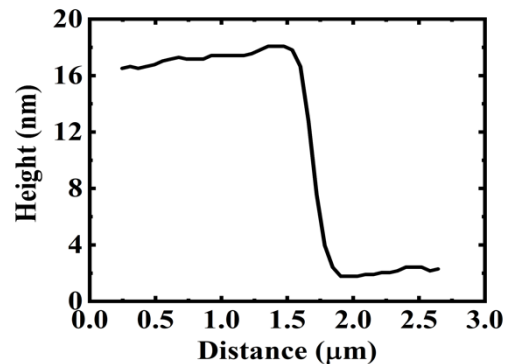
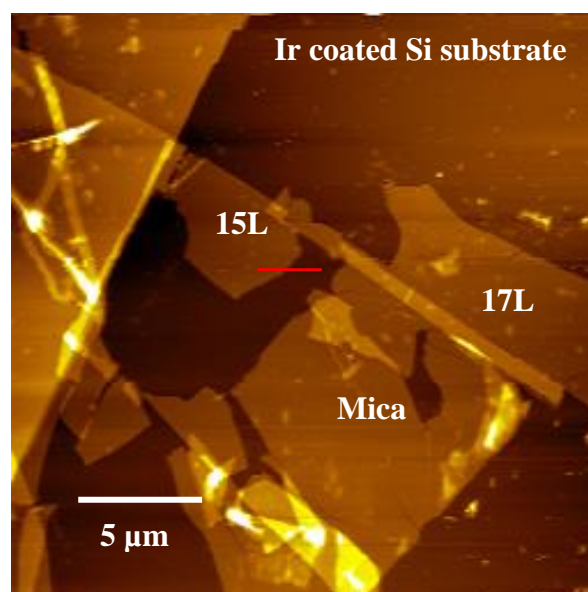


**Figure 3.6:** AFM images of mica nanosheets exfoliated down to (a) 4 nm, 5 nm, and 6 nm; (b) 4 nm; (c) 10 nm; (d) 15 nm thickness, pasted on the Ir/Si substrates. The typical cross-sectional line is shown with a red line and the corresponding height is shown on the right side of (a) and (b); on the bottom of (c) and (d). The numerals with the character “L” indicate the thickness of the mica nanosheets.

For the elemental analysis of exfoliated mica nanosheets with our modified process, we took the scanning Auger spectroscopy (AES) peaks shown in Fig. 3.7 (a). The peaks that appeared on the AES spectra show all mica elements except the carbon ( $C_{KLL}$ ) which emerged at 272 eV. The C peak that appeared in mica elemental analysis is due to environmental contamination. It is also reported that the degree of carbon contamination depends on the exfoliation process and the related mechanical tools engaged in it [45,46]. Our previous groups also analyzed and compared C contamination between two exfoliation techniques which are shown in Fig. 3.7 (b) [5]. The PDMS stamp-related exfoliation of the mica nanosheet showed a higher C peak than our polyurethane hand roller technique

suggesting a higher carbon (C) arose from the surface of the PDMS stamp. Even though the polyurethane hand roller does not have any undesirable species, the remaining carbon peak possibly attributed to contamination from the laboratory environment (as mentioned before) during the sample preparation time in the air.

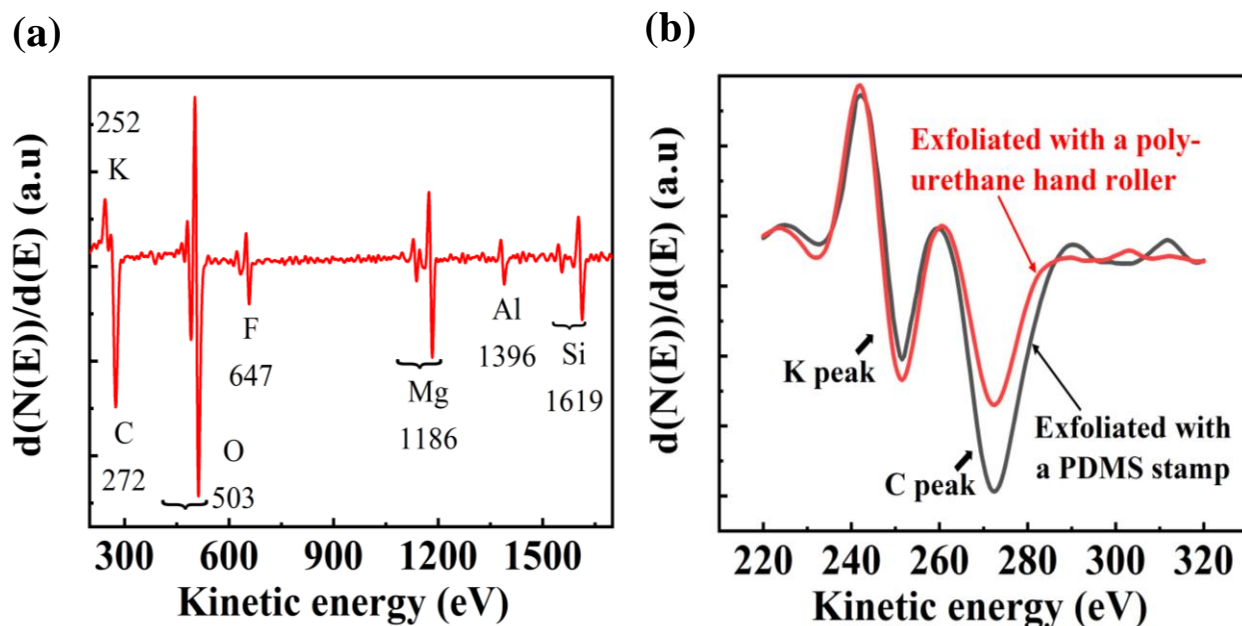
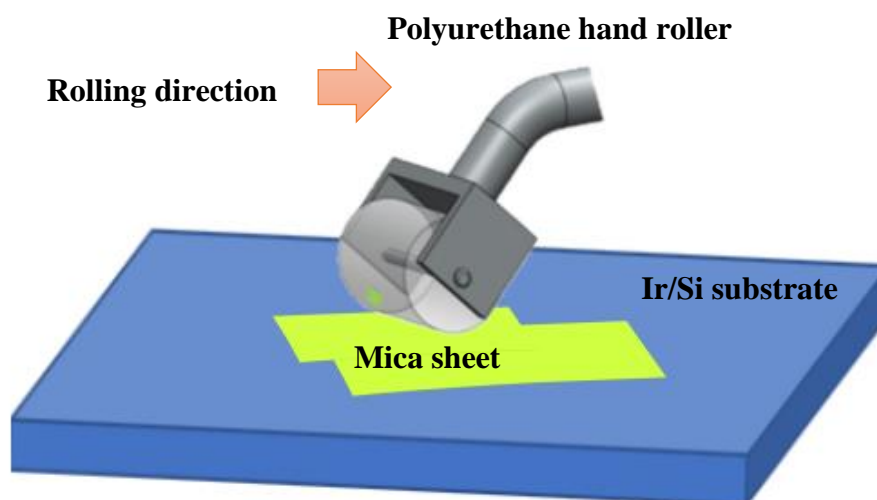


**Figure 3.7:** (a) Elemental analysis of 15nm mica pasted on Ir/Si substrate through AES. The corresponding peaks are represented by mica elements except for C which appeared at 272 eV, possibly due to lab environment-induced hydrocarbon contamination. (b) Two types of exfoliation shows the C contamination, suggesting polyurethane hand roller has lower contamination than PDMS.

The layer-by-layer mica structure has been assembled through the aluminosilicate layers where the potassium ( $K^+$ ) atoms layer is the connector between two aluminosilicate layers (Fig. 3.3). Inside mica, the aluminosilicate layer shows slightly negative charge dependence because of the replacement of a quarter of  $Si^{4+}$  ions by  $Al^{3+}$  ions which is electrostatically neutralized by positive  $K^+$  atom layer, as highlighted in the 3D atomic structure (Fig. 3.3). However, the bonding interaction force between the  $K^+$  layers and the aluminosilicate layers is considered as a weak attractive force resulting in an easy cleavage across their interface. On the other side, the long-range well-defined van der Waals (vdW) interaction force is dominated between exfoliated mica and the Ir coated Si (Ir/Si) substrate. A competition phenomenon happens between the vdW force that acts on the bottom

layer of mica and the weak electrostatic  $K^+$  layer of the upper exfoliated mica side. When an additional adhesive force concurrently works with vdW force between the bottom layer of mica and the Ir/Si substrate, the mica nanosheet can be separated from the layered structure, leaving the thin mica nanosheet on the substrate surface. A schematic diagram of modified mica exfoliation is presented in Fig. 3.8 (a) and (b). It demonstrates that the solid curved surface of the poly-urethane hand roller increases the interaction between the mica/substrate interface and thus enhances the exfoliation process. When the roller along with a few layers of mica (Fig. 3.8b) on its surface is rolled over the substrate, more uniform contact is established between the outermost mica layer and the supporting substrate which increased van der Waals force driven by an increase in pressure at the interface. The interaction forces between mica and substrate surface may vary due to differences in applied pressure, increased contact area, and decreased overall contact distances. For this reason, separations occurred between the mica layers i.e. started varying from monolayer to a few thin layers followed by thick layers and transferred onto the substrate surface (Fig. 3.8b). A similar mechanism happened when the roller is rolled over the bulk mica to transfer mica sheets onto the roller surface. There is also a probability that monolayer or few layers of mica flake that attached to the roller surfaces from the bulk mica are directly transferred onto the substrate surface. Upon cleavage of the mica surface exhibits a hexagonal arrangement of  $SiO_4$  tetrahedra and O atoms partly covered by potassium ions over the exposing surface [47]. Therefore, we also tried to image the exfoliated surface of mica at a smaller range which is shown in Fig. 3.9 (a) and (b) for a scan area of  $6\text{ nm} \times 6\text{ nm}$ . In Fig. 3.9 (c) and (d), the same area has been minimized to a  $3\text{ nm} \times 3\text{ nm}$  area to observe the structure more clearly. From our typical topographic AFM image in contact, the hexagonal periodic structure for the  $6\text{ nm} \times 6\text{ nm}$  scan area is clearly visible which has been enlarged in Fig. 3.9 (c) and (d) for a small area. The dark spots correspond to the holes of the hexagonal ring. Even though some distortion appeared on the images, the mean unit cell dimension is almost equal to the measured value reported in [47]. We used our contact AFM system for atomic imaging with a PtSi force sensor and all the images were taken in an Ar-gas controlled environment. We also used a rotational angle of  $50^\circ$  for the imaging which showed the most satisfactory atom resolved image.

(a)



(b)

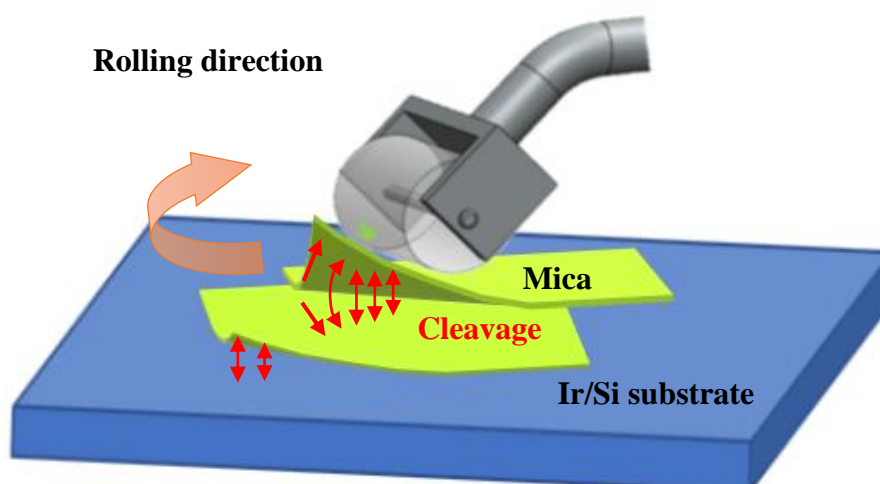


**Figure 3.8:** Enlarged schematic view of exfoliation of 2D mica nanosheet. (a) The initial position of the roller from where it started rolling, the increased pressure on the roller causes identical spacing between mica and substrate through which vdW on the interface enhanced. (b) At some arbitrary position where mica layer started to cleave and pasted on the substrate. Although the mica nanosheet is very small compared to the hand roller, a large representation of the nanosheets has been used on the above images for demonstration purposes.



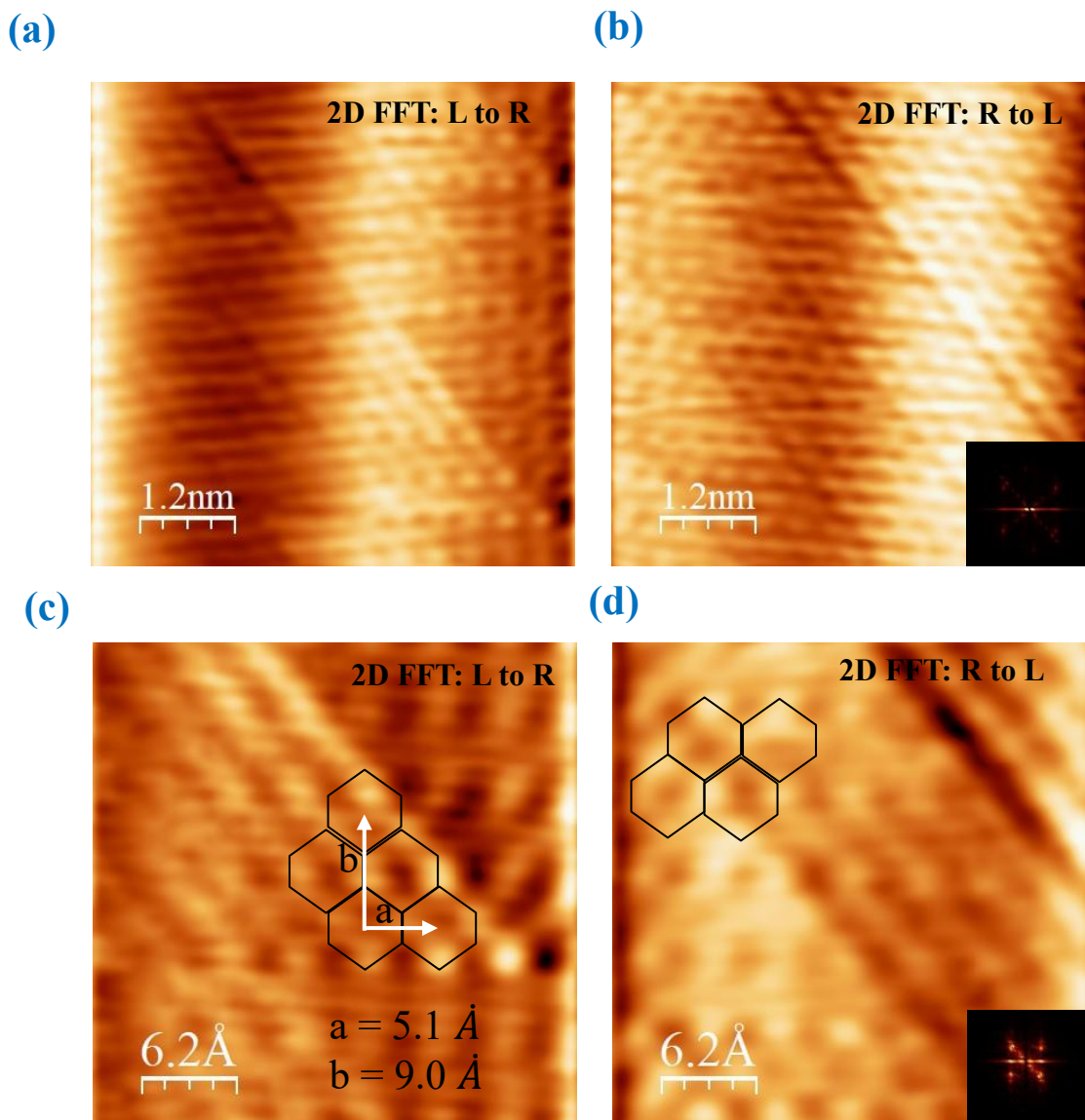


**Figure 3.9:** AFM topographic images of (001) basal plane of exfoliated phlogopite mica; (a) left to right, (b) right to left with a scanning area of  $6 \times 6 \text{ nm}^2$  and  $256 \times 256$  data points per line. The scanning speed was 290 nm/sec and the imaging time per frame was  $\sim 11$  sec. (c) and (d) represent a smaller area of  $3 \times 3 \text{ nm}^2$  and the scanning speed was 301 nm/sec with a minimal applied loading force on the cantilever and at zero bias voltage. Both images were taken at a rotation angle of  $50^\circ$ .

### 3.4 Summary:

The modified exfoliation technique for the cleaving of 2D materials has been discussed in this chapter. We chose artificially synthesized phlogopite mica as a representative for 2D layered materials and Ir coated n-type Si(111) as a substrate material. We hope this technique can equally be applied to other layered materials as well. We found optical images gave us an easy access to the area where mica sheets with thin thickness were possible as well as to run AFM analysis. From the typical AFM data, we measured the surface morphology, exact height, and dimension of the mica nanosheets. Through our results, we found successful deposition of mica nanosheets with a large dimension varying from thick to thin layer, confirmed by AES and AFM analysis. Similar results were also found for the different substrates reported in [5]. Additionally, atomic images by contact method also showed the similar results for exfoliated mica drawn previously. All of those data provided satisfactory results and validity of our exfoliation technique and offer further investigation for other 2D layered materials with less contamination.



## References:

- [1] J. Golden, M. McMillan, R.T. Downs, G. Hystad, I. Goldstein, H.J. Stein, A. Zimmerman, D.A. Sverjensky, J.T. Armstrong, R.M. Hazen, *Earth Planet. Sci. Lett.* 366 (2013) 1–5.
- [2] B.C. Brodie, *Philos. Trans. R. Soc.* 149 (1859) 249–259.
- [3] G.R. Bhimanapati, Z. Lin, V. Meunier, Y. Jung, J. Cha, S. Das, D. Xiao, Y. Son, M.S. Strano, V.R. Cooper, L. Liang, S.G. Louie, E. Ringe, W. Zhou, S.S. Kim, R.R. Naik, B.G. Sumpter, H. Terrones, F. Xia, Y. Wang, J. Zhu, D. Akinwande, N. Alem, J.A. Schuller, R.E. Schaak, M. Terrones, J.A. Robinson, *ACS Nano* 9 (2015) 11509–11539.
- [4] H.K. Christenson, N.H. Thomson, *Surf. Sci. Rep.* 71 (2016) 367–390.
- [5] M.R. Islam, M. Tomitori, *Appl. Surf. Sci.* 532 (2020) 147388–147401.
- [6] M. Ezawa, *Phys. Rev. Lett.* 109 (2012) 1–5.
- [7] Y. Huang, E. Sutter, N.N. Shi, J. Zheng, T. Yang, D. Englund, H.J. Gao, P. Sutter, *ACS Nano* 9 (2015) 10612–10620.
- [8] S. He, J. He, W. Zhang, L. Zhao, D. Liu, X. Liu, D. Mou, Y.B. Ou, Q.Y. Wang, Z. Li, L. Wang, Y. Peng, Y. Liu, C. Chen, L. Yu, G. Liu, X. Dong, J. Zhang, C. Chen, Z. Xu, X. Chen, X. Ma, Q. Xue, X.J. Zhou, *Nat. Mater.* 12 (2013) 605–610.
- [9] C. Zhang, C. Wang, F. Yang, J.K. Huang, L.J. Li, W. Yao, W. Ji, C.K. Shih, *ACS Nano* 13 (2019) 1595–1602.
- [10] M.A. McGuire, H. Dixit, V.R. Cooper, B.C. Sales, *Chem. Mater.* 27 (2015) 612–620.
- [11] D. Jiang, T. Hu, L. You, Q. Li, A. Li, H. Wang, G. Mu, Z. Chen, H. Zhang, G. Yu, J. Zhu, Q. Sun, C. Lin, H. Xiao, X. Xie, M. Jiang, *Nat. Commun.* 5 (2014) 1–6.
- [12] S. Tang, C. Zhang, Di. Wong, Z. Pedramrazi, H.Z. Tsai, C. Jia, B. Moritz, M. Claassen, H. Ryu, S. Kahn, J. Jiang, H. Yan, M. Hashimoto, D. Lu, R.G. Moore, C.C. Hwang, C. Hwang, Z. Hussain, Y. Chen, M.M. Ugeda, Z. Liu, X. Xie, T.P. Devereaux, M.F. Crommie, S.K. Mo, Z.X. Shen, *Nat. Phys.* 13 (2017) 683–687.
- [13] Y. Zhang, J.J. Lee, R.G. Moore, W. Li, M. Yi, M. Hashimoto, D.H. Lu, T.P. Devereaux, D.H. Lee, Z.X. Shen, *Phys. Rev. Lett.* 117 (2016) 1–5.

- [14] S. V. Morozov, K.S. Novoselov, M.I. Katsnelson, F. Schedin, D.C. Elias, J.A. Jaszczak, A.K. Geim, *Phys. Rev. Lett.* 100 (2008) 11–14.
- [15] I.V. Grigorieva, A.A. Firsov, K. S. Novoselov, A. K. Geim, S. V. Morozov, D. Jiang, Y. Zhang, S. V. Dubonos, *Science* 306 (2016) 666–669.
- [16] M. Xu, T. Liang, M. Shi, H. Chen, *Chem. Rev.* 113 (2013) 3766–3798.
- [17] K.S. Novoselov, A.K. Geim, S. V. Morozov, D. Jiang, M.I. Katsnelson, I. V. Grigorieva, S. V. Dubonos, A.A. Firsov, *Nature* 438 (2005) 197–200.
- [18] Y. Zhang, J.P. Small, W. V. Pontius, P. Kim, *Appl. Phys. Lett.* 86 (2005) 1–3.
- [19] C. Lee, X. Wei, J.W. Kysar, J. Hone, *Science* 321 (2008) 385–388.
- [20] R.R. Nair, P. Blake, A.N. Grigorenko, K.S. Novoselov, T.J. Booth, T. Stauber, N.M.R. Peres, A.K. Geim, *Science* 320 (2008) 1308.
- [21] F. Schedin, A.K. Geim, S. V. Morozov, E.W. Hill, P. Blake, M.I. Katsnelson, K.S. Novoselov, *Nat. Mater.* 6 (2007) 652–655.
- [22] Y.M. Lin, C. Dimitrakopoulos, K.A. Jenkins, D.B. Farmer, H.Y. Chiu, A. Grill, P. Avouris, *Science* 327 (2010) 662.
- [23] Y.M. Lin, K.A. Jenkins, V.G. Alberto, J.P. Small, D.B. Farmer, P. Avouris, *Nano Lett.* 9 (2009) 422–426.
- [24] X. Wang, L. Zhi, K. Müllen, *Nano Lett.* 8 (2008) 323–327.
- [25] X. Zhou, X. Huang, X. Qi, S. Wu, C. Xue, F.Y.C. Boey, Q. Yan, P. Chen, H. Zhang, *J. Phys. Chem. C* 113 (2009) 10842–10846.
- [26] X. Li, Y. Zhu, W. Cai, M. Borysiak, B. Han, D. Chen, R.D. Piner, L. Colomba, R.S. Ruoff, *Nano Lett.* 9 (2009) 4359–4363.
- [27] R. Sordan, F. Traversi, V. Russo, *Appl. Phys. Lett.* 94 (2009) 073305–073308.
- [28] X. Chen, K.J. Lee, D. Akinwande, G.F. Close, S. Yasuda, B. Paul, S. Fujita, J. Kong, H.S.P. Wong, *IEEE IEDM* (2009) 581–584.
- [29] B. Radisavljevic, A. Radenovic, J. Brivio, V. Giacometti, A. Kis, *Nat. Nanotechnol.* 6 (2011) 147–150.

- [30] T. Georgiou, R. Jalil, B.D. Belle, L. Britnell, V. Roman, S. V Morozov, Y. Kim, A. Gholinia, S.J. Haigh, O. Makarovsky, L. Eaves, L.A. Ponomarenko, A.K. Geim, K.S. Novoselov, A. Mishchenko, *Nat. Nanotech.* 8(2) (2013) 100–103.
- [31] R. Coehoorn, C. Haas, J. Dijkstra, C.J.F. Flipse, R.A. De Groot, A. Wold, *Phys. Rev. B* 35 (1987) 6195–6202.
- [32] H. Fang, S. Chuang, T.C. Chang, K. Takei, T. Takahashi, A. Javey, *Nano Lett.* 12 (2012) 3788–3792.
- [33] L. Liu, P. Feng, X. Shen, *Phys. Rev. B - Condens. Matter Mater. Phys.* 68 (2003) 1–8.
- [34] Y. Bitla, Y.H. Chu, *FlatChem* 3 (2017) 26–42.
- [35] L. Pauling, *Proc. N. A. S.* 16(2) (1930) 123–129.
- [36] L. Meng, Y. Wang, L. Zhang, S. Du, R. Wu, L. Li, Y. Zhang, G. Li, H. Zhou, W.A. Hofer, H.J. Gao, *Nano Lett.* 13 (2013) 685–690.
- [37] S. Wang, Y. Rong, Y. Fan, M. Pacios, H. Bhaskaran, K. He, J.H. Warner, *Chem. Mater.* 26 (2014) 6371–6379.
- [38] X. Wang, H. Feng, Y. Wu, L. Jiao, *J. Am. Chem. Soc.* 135 (2013) 5304–5307.
- [39] Y. Zhang, Y. Zhang, Q. Ji, J. Ju, H. Yuan, J. Shi, T. Gao, D. Ma, M. Liu, Y. Chen, X. Song, H.Y. Hwang, Y. Cui, Z. Liu, *ACS Nano* 7 (2013) 8963–8971.
- [40] S. Substrates, X. Lu, M.I.B. Utama, J. Lin, X. Gong, J. Zhang, Y. Zhao, S.T. Pantelides, J. Wang, Z. Dong, Z. Liu, W. Zhou, Q. Xiong, *Nano Lett.* 14 (2014) 2419–2425.
- [41] L. Colombo, X. Li, B. Han, C. Magnuson, W. Cai, Y. Zhu, R.S. Ruoff, *ECS Trans.* 28 (2019) 109–114.
- [42] Y. Huang, Y.H. Pan, R. Yang, L.H. Bao, L. Meng, H.L. Luo, Y.Q. Cai, G.D. Liu, W.J. Zhao, Z. Zhou, L.M. Wu, Z.L. Zhu, M. Huang, L.W. Liu, L. Liu, P. Cheng, K.H. Wu, S.B. Tian, C.Z. Gu, Y.G. Shi, Y.F. Guo, Z.G. Cheng, J.P. Hu, L. Zhao, G.H. Yang, E. Sutter, P. Sutter, Y.L. Wang, W. Ji, X.J. Zhou, H.J. Gao, *Nat. Commun.* 11 (2020) 1–9.
- [43] Y. Cao, V. Fatemi, S. Fang, K. Watanabe, T. Taniguchi, E. Kaxiras, P. Jarillo-Herrero, *Nature* 556 (2018) 43–50.

- [44] <https://dspace.jaist.ac.jp/dspace/bitstream/10119/17002/2/paper.pdf>.
- [45] S. Tongay, W. Fan, J. Kang, J. Park, U. Koldemir, J. Suh, D.S. Narang, K. Liu, J. Ji, J. Li, R. Sinclair, J. Wu, *Nano Lett.* 14 (2014) 1–14.
- [46] A. Jain, P. Bharadwaj, S. Heeg, M. Parzefall, T. Taniguchi, K. Watanabe, L. Novotny, *Nanotechnology* 29 (2018) 265203–265212.
- [47] Y. Kuwahara, *Phys. Chem. Miner.* 28 (2001) 1–8.

## Chapter 4: Evaluation of Mechanical Energy Dissipation using Frequency Modulation Atomic Force Microscopy

Due to the nonconservative interactions acting between the tip on a cantilever and a sample, mechanical energy preserved in an oscillating cantilever in frequency modulation atomic force microscopy (FM-AFM) was dissipated. Here, we estimated the variation of the energy dissipation ( $D_{\text{dis}}$ ) using the FM-AFM with a metal-coated tip for a metal-coated Si substrate partially covered with thin mica films (mica nanosheets) with various thicknesses. The variation of  $D_{\text{dis}}$  was predominantly governed by the electrostatic interaction under a bias voltage for distant tip-sample separations, chiefly responsible for Joule heat owing to the vertical tip oscillation in the FM-AFM. From the analysis of  $D_{\text{dis}}$  and the frequency shift of the cantilever, which depended quadratically on the bias voltage, electrical resistance presenting Joule heat was evaluated to be of the order of  $\text{G}\Omega$  and changed with the mica thicknesses. We comprehensively studied the source of such great values of resistance in terms of surface scattering of charges moved by the oscillating tip and dielectric energy loss for the mica nanosheet. Measurement of energy dissipation in the FM-AFM exhibited the potential to probe the local surface electronic properties in non-contact.

### 4.1 Introduction:

The most cutting-edged functional micro/nanodevices based on exotic materials have been developed for the miniaturization of electronic devices. For the advancement of those devices, microscopic analysis of new materials with a high spatial resolution of less than nanometers is indispensable. For the nanoscale analysis of conducting, semiconducting, and insulating materials, the atomic force microscopy (AFM) [1] has played a prime role in the observation of their surface topography [2–5] as well as characterization of their mechanical and electrical properties [6–11]. There are several types of AFMs operated in different modes for a cantilever as a force sensor. Among them, the frequency modulation atomic force microscopy (FM-AFM) [12] is highly preferred to carry out high-resolution analysis in a stable manner, because the sample damage caused by contact or tapping of a probe (tip) can be avoided owing to the apparent high-stiffness of an oscillating cantilever as well as its high force sensitivity [13–15]. In an FM-AFM, the nanotip at the end of a cantilever is being oscillated at its resonance frequency ( $f$ ), and the resonance frequency shift ( $\Delta f$ ) is measured;  $\Delta f$  sensitively changes depending on the conservative force interactions acting between the tip and the

sample [16,17]. Consequently, the tip can be brought in proximity to the sample surface so that its intricate properties are unveiled with a sub-nanometer resolution.

Moreover, the nonconservative force interactions acting between the tip and the sample can also be measured using the FM-AFM [18,19]. The mechanical oscillation energy stored in the oscillating cantilever is dissipated through the nonconservative interactions between the tip and the sample. In the FM-AFM, the cantilever excitation typically being performed using an excitation signal ( $V_{\text{exc}}$ ) and can be monitored, while the cantilever oscillating amplitude ( $A$ ) is being kept constant by a feedback controller. Any change in  $V_{\text{exc}}$  corresponds to the change in the energy dissipation ( $D_{\text{dis}}$ ). Using such a self-excitation cantilever the conservative and nonconservative (dissipative) interactions can be separately and simultaneously detected as  $\Delta f$  and  $V_{\text{exc}}$ , respectively, using a phase lock loop (PLL) along with a phase shifter [20]. Through the measurement of energy dissipation, many fascinating features of sample surfaces have been reported [21–24]. The observed dissipations have been categorized as Brownian motion [25], hysteretic force interactions [26,27] including single-atom contact adhesion [28] and atomic displacement,<sup>21)</sup> Joule heat [29], etc.

Denk and Pohl first studied the Joule heat dissipation induced by capacitive displacement current passing between a semiconductor surface and a conductive tip on the oscillating cantilever [30]. They observed the scanned images exhibiting the local variation of surface conductance via Joule heat dissipation. This had opened a novel method to examine the local resistivity near the surface without contact of the probe with the surface during AFM imaging. Subsequently, several attempts have been done to characterize the Joule heat dissipation depending on the tip–sample separation, the bias voltage between them, and resistance in a tip–sample circuit loop [20,29,31]. Additionally, Arai et al. derived the proportional relationship between  $D_{\text{dis}}$  and  $\Delta f_{\text{ele}}$ , which is the frequency shift due to the long-range electrostatic force; they also reported that resistance  $R_J$  representing the Joule heat generation could be evaluated from the slop of  $D_{\text{dis}}$  as a function of  $\Delta f_{\text{ele}}$  [32]. The value of  $R_J$  was experimentally measured to be so large as the order of  $G\Omega$  for a Si(111)-(7×7) surface of even a low resistivity Si wafer, examined using a low-resistivity boron-doped Si tip. It was pointed out that the oscillating tip caused the oscillatory motion of surface charges along the surface, resulting in Joule heat through the surface resistance. Because the oscillation also caused the oscillatory motion of the tip surface charges, the value of  $R_J$  could include the resistance for Joule heat on the tip surface. Although the evaluation of  $R_J$  as surface resistance using the dissipation channel of FM-AFM is fascinating for non-destructive nanoscale characterization, the interpretation of  $R_J$  is still unsettled. It

demands strong clarification of which part of the tip and sample dominantly contributes to the large value of  $R_J$  for extension of the analysis using the proportional relationship between  $D_{\text{dis}}$  and  $\Delta f_{\text{ele}}$ .

Through this research work, we measured the energy dissipation using the FM-AFM with a conductive Si tip coated with metal (Pt-Ir) for a conductive Ir-sputtered Si substrate locally covered with mica nanosheets with different nanometer thicknesses and evaluated the high values of electric resistance from the plots of  $D_{\text{dis}}$  as a function of  $\Delta f_{\text{ele}}$ . For the mica nanosheets, we used artificially synthesized phlogopite ( $\text{KMg}_3\text{AlSi}_3\text{O}_{10}\text{F}_2$ ) with high purity, purer than natural muscovite, as a member of mica family. The mica nanosheets of phlogopite with high mechanical and temperature stability and low dielectric loss have the potential for components of micro/nanodevices as very thin insulators [33–36]; their thickness is an integer multiple of its unit thickness (approximately 1 nm), and the exfoliated phlogopite exhibits an atomically flat surface. Since the mica nanosheet acts as an ultra-thin dielectric layer, the electrical properties between the tip and the sample could be locally changed over the nanosheet depending on its thickness, comparable with those of the bare metal-coated sample surface. Thus, we shed light on the difference in energy dissipation between the mica-covered and non-covered surfaces on the conductive substrate, which provides a key to understanding the energy dissipation induced by the tip oscillation under a bias voltage, detected by the FM-AFM.

## 4.2 Experimental:

We used a commercial AFM setup (5500 AFM/SPM, Agilent Technologies, Inc., Santa Clara, CA, USA), the head of which was placed in a closed environmental chamber filled with pure argon gas (Ar, 99.999%). The AFM was operated as the FM-AFM by use of a phase-locked loop (PLL) (easy PLL, Nanosurf AG, Liestal, Switzerland). Thereby the AFM cantilever was being oscillated at its resonance frequency ( $f$ ) by applying a sinusoidal excitation voltage with amplitude  $V_{\text{exc}}$  to a modulation piezo element supporting the cantilever; the phase difference between the oscillation output signal and the excitation voltage was adjusted so as to make the maximum amplitude ( $A$ ) of the resonant oscillation of the cantilever at a far distance from the sample. The force ( $F_{\text{ts}}$ ) acting between the sample and the tip at the end of the cantilever changed  $\Delta f$ , which was the shift of  $f$  from the resonance frequency ( $f_0$ ) of the cantilever at a far distance from the sample. The force  $F_{\text{ts}}$  could be calculated from the changes in  $\Delta f$  with respect to the tip-sample separation by Sadar-Jarvis numerical method [37]. The amplitude of the excitation voltage,  $V_{\text{exc}}$ , was adjusted to keep the

oscillation amplitude ( $A$ ) of the cantilever constant using a feedback controller. Under this condition, the energy dissipation ( $D_{\text{dis}}$ ) was evaluated from the change in  $V_{\text{exc}}$  using the following equation [20],

$$D_{\text{dis}} = 2\pi \frac{\frac{1}{2}kA^2}{Q} \left( \frac{V_{\text{exc}}}{V_{\text{exc}}(0)} - 1 \right). \quad (27)$$

Here,  $k$  is the spring constant of the cantilever,  $Q$  is the quality factor of the cantilever as an oscillator, and  $V_{\text{exc}}(0)$  is the amplitude of excitation voltage for the tip at a far distance from the sample. Labuda et al. reported that the value of  $D_{\text{dis}}$  should be corrected by the introduction of a prefactor at the front of  $V_{\text{exc}}/V_{\text{exc}}(0)$  in eq. 1, when excitation of the cantilever oscillation has spurious characteristics depending on the frequency due to the mechanical vibrational features through the piezo element and surrounding circumstances for the cantilever oscillation [38]. We estimated the features of our FM-AFM setup in terms of a transfer function, which is explained in Appendix I; here, the prefactor could be regarded as one.

Besides the topographic images of sample surfaces observed by the FM-AFM, we obtained the curves of  $\Delta f$  and  $D_{\text{dis}}$  as a function of the tip-sample bias voltage ( $V_s$ ) as well as a function of the tip-sample separation at our set positions over the sample surface; the tip electric potential was grounded. We used a commercial conductive Si cantilever coated with platinum-iridium (Pt-Ir) (PPT-NCHPt, NANOSENSORS<sup>TM</sup>, Neuchatel, Switzerland) having the resonance frequency ( $f_0$ ) = 265.8 kHz,  $k$  = 48 N/m, and  $Q$  = ~530 in Ar gas, and the nominal radius ( $r_{\text{tip}}$ ) of the metal-coated Si tip was less than 25 nm. The cantilever oscillation amplitude ( $A$ ) was 20 nm in this study. The intrinsic energy dissipation of the cantilever at a far distance from the sample surface was approximately 0.5 eV/cycle, estimated from the measured  $V_{\text{exc}}(0)$ .

As a substrate for sample preparation, an n-type Si(111) wafer with a resistivity of 0.4–0.9  $\Omega \cdot \text{cm}$  was cut into a rectangular piece. The substrate was cleaned in an ultrasonic bath of acetone and a UV ozone cleaner (NL-UV253, Filgen, Inc., Nagoya, Japan). Afterward, iridium (Ir) was coated on it to be ~12 nm in thickness to provide an electrical conductivity using a direct current (DC) magnetron sputtering machine (E-1030, Hitachi-Hightech Corporation, Tokyo, Japan); hereinafter denoted as Ir/Si substrate. The resistance between two spots of ~1 cm separation on the Ir/Si substrate, where copper wires were contacted with silver paste, was as low as about 10 k $\Omega$ , showing Ohmic characteristics in current-voltage curves. To form a very thin dielectric layer on the Ir/Si substrate, artificially synthesized phlogopite mica (10 mm  $\times$  10 mm  $\times$  0.5 mm, Itoh Kikoh Co., Ltd, Tokai, Japan) was mechanically exfoliated and affixed on the Ir/Si substrate using a polyurethane hand roller



which explained in the flow chart Fig. 4.1; also see the detailed preparation process explained in chapter 3. The thickness of exfoliated mica films was the integer multiples of 1 nm as the unit thickness of cleavage to the  $c$ -axis of the mica, usually ranging from 3 to 15 nm; named mica nanosheet. Since the sample was prepared in air, to remove water adsorbed on its surface, the sample was heated on the heating stage of the AFM at 120 °C for ~2 hours inside the chamber filled with pure Ar gas. After being cooled in the chamber, the sample was examined using the FM-AFM in the Ar gas.

Under a bias voltage as high as a few volts between a tip and a sample, the dominant force acting between the tip and the sample would be the electrostatic attractive force, when the tip-sample separation is wider than nanometers. Therein, the oscillating tip induces the displacement current ( $I_d$ ) through the capacitance ( $C$ ) between the tip and the sample that are electrically connected as a loop. When the loop has a resistance in series, represented by  $R_J$ , the displacement current generates Joule heat, which dissipates the mechanical energy of the tip oscillation. The Joule heat ( $D_J$ ) over one cycle of tip oscillation with frequency  $f$  is calculated as follows [32]:

$$D_J = \int_0^{\frac{1}{f}} I_d^2 R_J dt = \int_0^{\frac{1}{f}} \left( \frac{dC}{dt} \right)^2 (V_S - V_{CPD})^2 R_J dt = (V_S - V_{CPD})^2 R_J \int_0^{1/f} \left( \frac{dC}{dt} \right)^2 dt. \quad (28)$$

Here,  $V_S$  is the sample bias voltage, and  $V_{CPD}$  is the contact potential difference (CPD) between the tip and the sample. Meanwhile, the electrostatic attractive force ( $F_{ele}$ ) is expressed as follows [32]:

$$F_{ele} = \frac{1}{2} \frac{dC}{dz} (V_S - V_{CPD})^2, \quad (29)$$

where  $z$  is the tip-sample separation. Assuming that  $z$  is less than the tip radius ( $r_{tip}$ ) [38], we can derive the following equation,

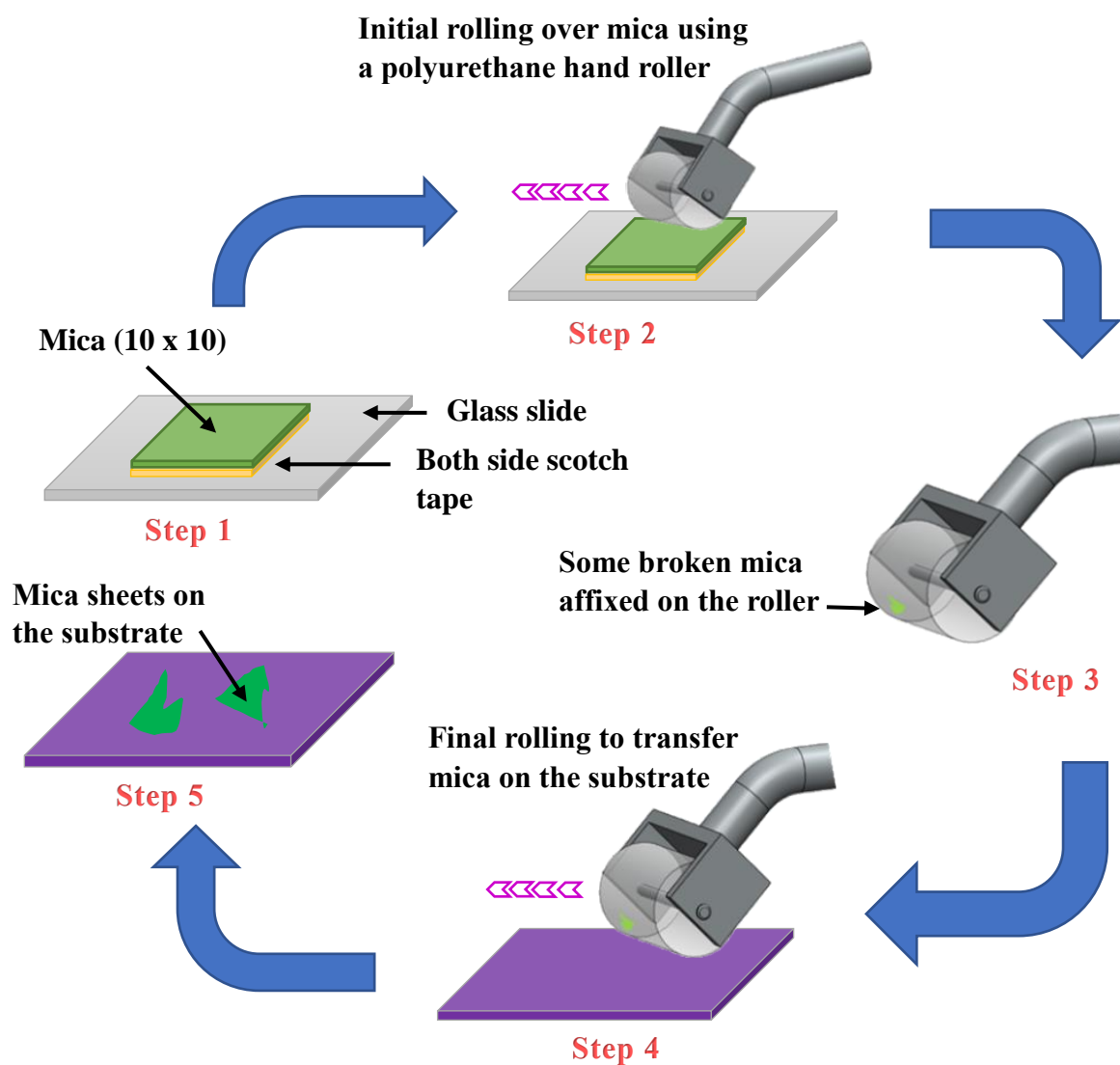


**Figure 4.1:** Profiling of mechanical exfoliation and affixing technique using polyurethane hand roller approach. Subsequent rolling over the bulk mica followed by second rolling on the Ir/Si substrate left mica nanosheet on the substrate, summarized completely by 5 steps.

$$F_{\text{ele}} = -\pi\epsilon_0 \frac{r_{\text{tip}}}{z} (V_S - V_{\text{CPD}})^2, \quad (30)$$

where  $\epsilon_0$  is the permittivity of vacuum. During continuous imaging, the tip position was scanned over the bare Ir/Si and mica surfaces. When the tip is placed over the mica nanosheet with thickness  $h$  and the relative dielectric constant  $\epsilon_r$ , as shown in Fig. 4.2 (a),  $z$  in eq. 30 should be replaced by  $z+h/\epsilon_r$ , according to ref. 40, by approximating the capacitance between a tip and a sample covered with a thin dielectric film. If the minimum tip-sample separation is  $d$ , eq. 30 can be rewritten by replacing  $z = d+A(1+\cos(2\pi f))$  by  $z = d+h/\epsilon_r+A(1+\cos(2\pi f))$  for the cantilever oscillating over the mica nanosheet. Then, the frequency shift due to the electrostatic force ( $\Delta f_{\text{ele}}$ ) is calculated as below, under a large amplitude approximation ( $d \ll A$ ), where  $d$  is the minimum tip-sample separation [31],

$$\Delta f_{\text{ele}} = -\frac{f_0 \pi \epsilon_0 r_{\text{tip}}}{\sqrt{2} k A^{3/2}} \frac{1}{(d+h/\epsilon_r)^{1/2}} (V_S - V_{\text{CPD}})^2. \quad (31)$$

Under the above approximation, we also obtain the equation for  $D_J$  on the basis of eq. 28 using  $dC/dz \cong -2\pi\epsilon_0 r_{\text{tip}}/(d+h/\epsilon_r)$ , as follows [32]:

$$D_J = 8\sqrt{2}\pi^4 \epsilon_0^2 f_0 A^{1/2} r_{\text{tip}}^2 R_J \frac{1}{(d+h/\epsilon_r)^{1/2}} (V_S - V_{\text{CPD}})^2. \quad (32)$$

Meanwhile, when dielectric films like the mica nanosheets cover the substrate under the alternating electric field induced by the tip oscillation, the electric dipoles in the mica nanosheets are forced to be parallel to the electric field. Even though the directional change of the dipoles under tip oscillation would be mostly elastic, the dipoles do not instantly respond to the change of the electric field. Consequently, the time delay causes energy dissipation, which is known as dielectric energy loss. When the dielectric energy loss of the mica nanosheet is large,  $R_J$  in eq. 32 can be replaced by the term  $(R_J + r_m \sin^2 \delta)$ , as described in Appendix II. Here,  $r_m$  is a resistor in parallel with a capacitance  $C_m$  in an equivalent circuit of the mica nanosheet, as shown in Fig. 4.2 (b), and  $\delta$  is the phase difference of the complex dielectric function of the mica nanosheet. Comparing eq. 31 with eq. 32, the following linear relationship between  $\Delta f_{\text{ele}}$  and  $D_J$  is derived by canceling  $(d+h/\epsilon_r)$  and  $(V_S - V_{\text{CPD}})$  in eqs. 31 and 32 [32],

$$D_J = -16\pi^3 \epsilon_0 k A^2 r_{\text{tip}} (R_J + r_m \sin^2 \delta) \times \Delta f_{\text{ele}}. \quad (33)$$

Thus, to study the relationship between  $D_J$  and  $\Delta f_{\text{ele}}$ , and to evaluate the value of  $(R_J + r_m \sin^2 \delta)$ , we experimentally took the curves of  $D_{\text{dis}}$  and  $\Delta f$  as a function of  $V_S$  for the samples partly covered with

the mica nanosheets of different thicknesses. It is noted that  $(R_J + r_m \sin^2 \delta)$  becomes  $R_J$  in eq. 33 for the bare Ir/Si substrate.

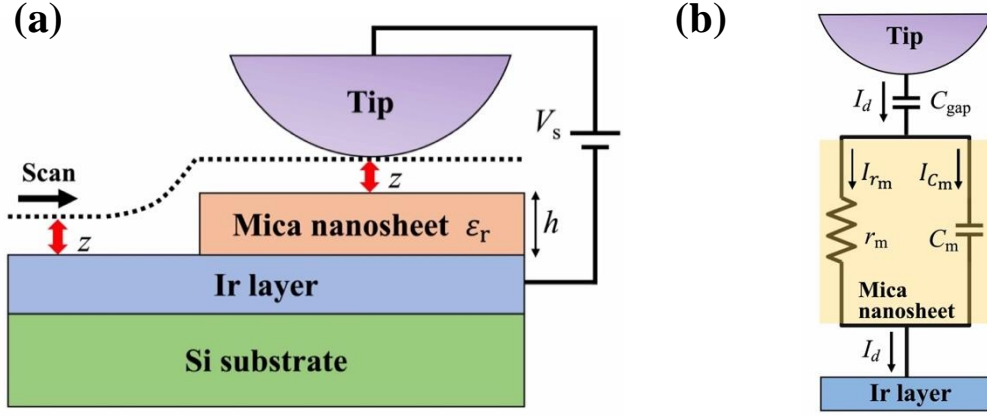


**Fig. 4.2:** (a) Schematic of the tip and the Ir/Si substrate partly covered with the mica nanosheet with thickness  $h$  and relative dielectric constant  $\epsilon_r$ . The tip is scanned by the FM-AFM over the sample with separation  $z$  between the tip apex and the sample surface under the bias voltage  $V_s$ . (b) Equivalent circuit representing the tip-sample system. The mica nanosheet is represented by a capacitor of  $C_m$  with a parallel resistor of  $r_m$  as dielectric energy loss. The gap between the tip and the surface of the mica nanosheet is represented by a capacitor of  $C_{\text{gap}}$ . The displacement current  $I_d$  passes through  $C_{\text{gap}}$ , and is divided into  $I_{C_m}$  and  $I_{r_m}$ , which respectively pass-through  $C_m$  and  $r_m$ . Details in Appendix II.

### 4.3 Results and Discussion:

Figures 4.3 (a) and (b) show the typical topographic FM-AFM image and the simultaneously obtained dissipation image of the sample surface with mica nanosheets pasted on the Ir/Si substrate at  $\Delta f = -40$  Hz at a sample bias voltage ( $V_s$ ) of  $-5$  V. The mica nanosheets with some rectangular in shape were found in Fig. 4.3 (a). The surface of the bare Ir/Si substrate, in the upper and left regions of Fig. 4.3 (a), seemed smooth and had no noticeable features. The cross-sectional line profiles along lines A and B, in Fig. 4.3 (a), across the regions of the mica nanosheets and the bare Ir/Si substrate are shown in Figs. 4.3 (c) and (d), respectively; the thickness of the nanosheets was approximately 4 nm, corresponding to 4-layer mica, and the regions as the mica nanosheets were overlapped, denoted by the red arrowheads in Fig. 4.3 (a), had the height of approximately 8 nm, which were the double of 4-layer mica thickness. The mica nanosheets looked distinct from the bare Ir/Si substrate in the topographic image but not in the dissipation image, even over the overlapped regions; these are also seen in the cross-sectional line profiles of dissipation in Figs. 4.3 (e) and (f), whereas the noise level of the dissipation was about 0.5 eV/cycle. Some prominent dots and a few faint strings on the mica nanosheets were also not recognized in the dissipation image. The small dots on the mica nanosheet could result from reactions with adsorbed water, or hydrocarbon residues in the preparation process, as reported [35,39].

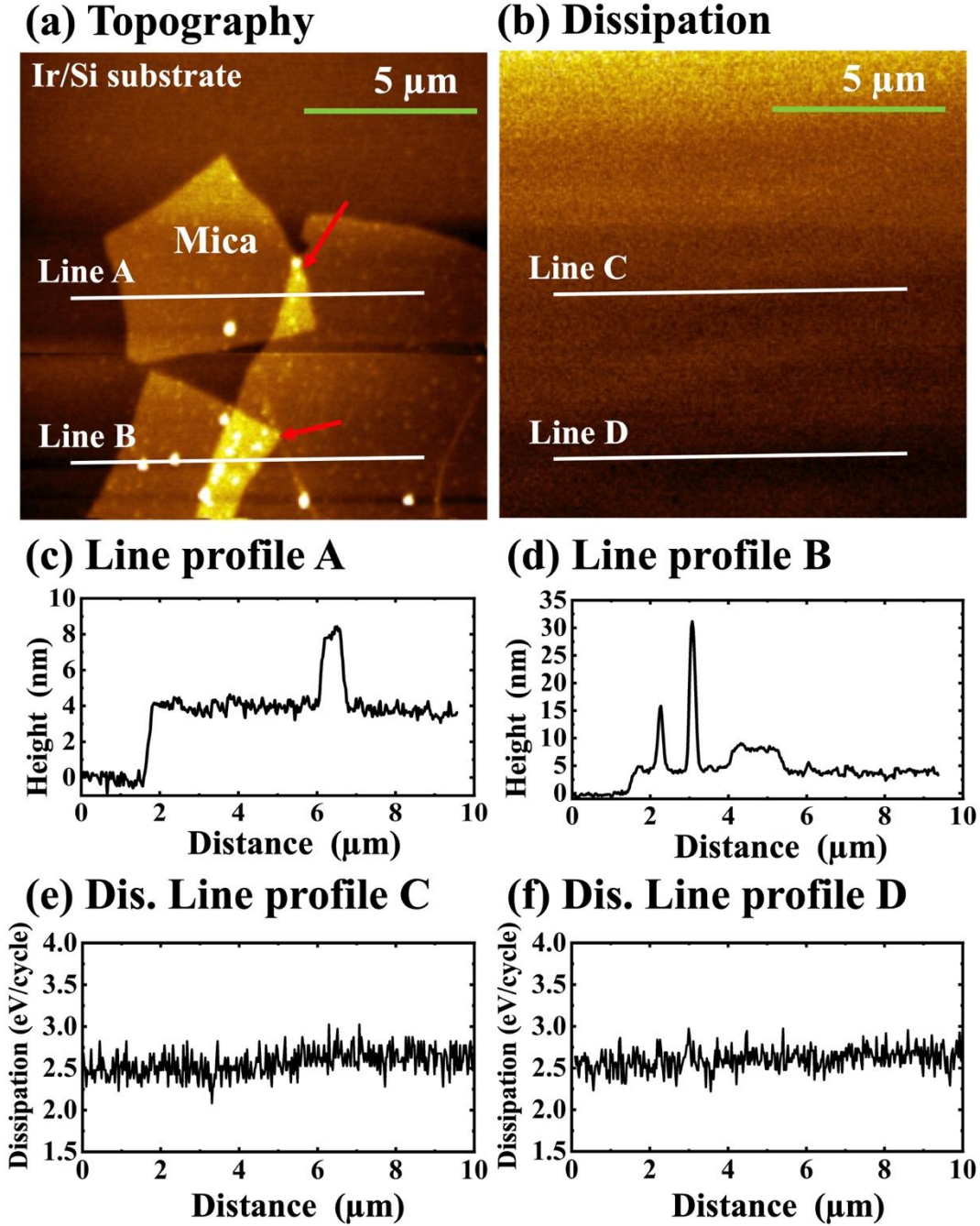


**Fig. 4.3:** (a) FM-AFM topographic image of the mica nanosheets with 4-layer thickness (4 nm) on the Ir/Si substrate in a scan area of  $13\ \mu\text{m} \times 13\ \mu\text{m}$  at  $\Delta f = -40\ \text{Hz}$  and  $V_s = -5.0\ \text{V}$ . The regions denoted by the red arrows in (a) indicate the regions of overlapped mica nanosheets. (b) dissipation image simultaneously taken with (a). (c) and (d) cross-sectional line profiles along lines A and B in (a), respectively. (e) and (f) cross-sectional line profiles of the dissipation along lines C and D in (b), respectively. Lines C and D in (b) are identical to lines A and B in (a), respectively, in the planar coordinates.

Figure 4.4 (a) shows the topographic image of the mica nanosheet with a thickness of 11 nm, taken at  $\Delta f = -45$  Hz and  $V_s = -5.0$  V, below which the cross-sectional line profile is presented (Fig. 4.4 (c)). The mica nanosheet with a few small dots was clearly observed in Fig. 4.4 (a). Contrasted to the dissipation image of the 4-layer mica nanosheet in Fig. 4.3 (b), the simultaneously obtained dissipation image of Fig. 4.4 (b) faintly shows the shape of the mica nanosheet, corresponding to that in Fig. 4.4 (a). The cross-sectional line profile of the dissipation in Fig. 4.4 (d) indicated slightly higher dissipation by  $\sim 1$  eV/cycle on average over the mica nanosheet, compared with that over the Ir/Si substrate, having the averaged value of dissipation of  $\sim 9.3$  eV/cycle.

We conducted the same observation for 8- and 15-layer mica nanosheets which are shown in Fig. 4.5 (a)–(d) with their corresponding line profiles below the images. We found a tendency that the shape of the mica nanosheets in the dissipation images was slightly more noticeable with the increasing thickness of the mica nanosheet. In Fig. 4.5 (a) and (b) where 8-layer mica nanosheet had been focused showed no dissipation contrast, but the folded region where the thickness of mica nanosheet becomes doubled (upper left segment for  $\sim 16$  nm) or higher (lower left segment for  $\sim 20$  nm) showed faint contrast similar to that of 11-layer discussed above. When we performed the experiment for 15-layer mica nanosheet (Fig 4.5 (c) and (d)), the dissipation contrast is clearly observed revealing the dependence of dissipation on mica thickness. Here, the scratches correspond to tip retraction to preserve the tip from unexpected damage due to any sharp objects appearing in its scanning path during fast scanning.

Figures 4.6 (a)–(f) show the curves of  $\Delta f$  and  $D_{\text{dis}}$  as a function of the tip–sample separation at  $V_s = -5.0$  V, taken over the regions of the Ir/Si substrate, which were far laterally from the mica nanosheets shown in Fig. 4.3, and the mica nanosheets with 4- and 11-layer thicknesses, the images of which are shown in Figs. 4.3 and 4.4, respectively. The curves of  $\Delta f$  showed decreases with decreasing separation, indicating that the attractive forces acted between the tip and the sample. The separations at  $\Delta f = -40$  Hz and  $-45$  Hz for the images in Figs. 4.3 and 4.4, respectively, and from the curves of  $\Delta f$ , were roughly estimated to be wider than a few tens of nanometers. At the separations, the resultant attractive forces acting between the tip and the sample were estimated to be  $\sim 1$  nN by Sadar–Jarvis method [37]. On the other hand, the curves of  $D_{\text{dis}}$  increased with decreasing separation over a few hundreds of nanometers. It is noted that the increase in  $D_{\text{dis}}$  was steeper at the closer separations for the thicker mica nanosheets.

Figure 4.7 shows the curves of  $\Delta f$  and  $D_{\text{dis}}$  as a function of the sample bias voltage ( $V_s$ ), taken at the same positions as those in Fig. 4.6. All the curves showed quadratic behaviors; according to eqs. 31 and 32,  $\Delta f_{\text{ele}}$  and  $D_J$  are proportional to  $(V_s - V_{\text{CPD}})^2$ . Thus, by subtracting an offset value, we can extract the values of  $\Delta f_{\text{ele}}$  and  $D_J$  from  $\Delta f$  and  $D_{\text{dis}}$  in Fig. 4.7, respectively;  $\Delta f$  and  $D_{\text{dis}}$  include the contribution from the van der Waals interactions that have no bias-voltage dependence. Using eqs. 31 and 32, we also estimated the values of  $V_{\text{CPD}}$ ;  $\Delta f$  and  $D_{\text{dis}}$  curves exhibit the maximum and the minimum at  $V_s = V_{\text{CPD}}$ , respectively. For the Ir/Si substrate,  $V_{\text{CPD}}$  was +0.1 V for both  $\Delta f$  and  $D_{\text{dis}}$  curves, and 0.0 V for 4-, 8-, 11-, and 15-layer mica nanosheets for both  $\Delta f$  and  $D_{\text{dis}}$  curves. This implies that electric dipole layers were formed at the interface between the mica nanosheet and the Ir/Si substrate and/or at the interface between the surface of mica nanosheet and the Ar gas environment, but almost no net uniform charges inside the mica nanosheets, because  $V_{\text{CPD}}$  did not change with increasing thickness of mica nanosheets. Notably, the value of  $D_{\text{dis}}$  at  $V_s = V_{\text{CPD}}$  was almost zero. This indicates that the long-range attractive forces such as van der Waals interactions did not contribute much to the energy dissipation, which was less than the detection limit of our measurement system.



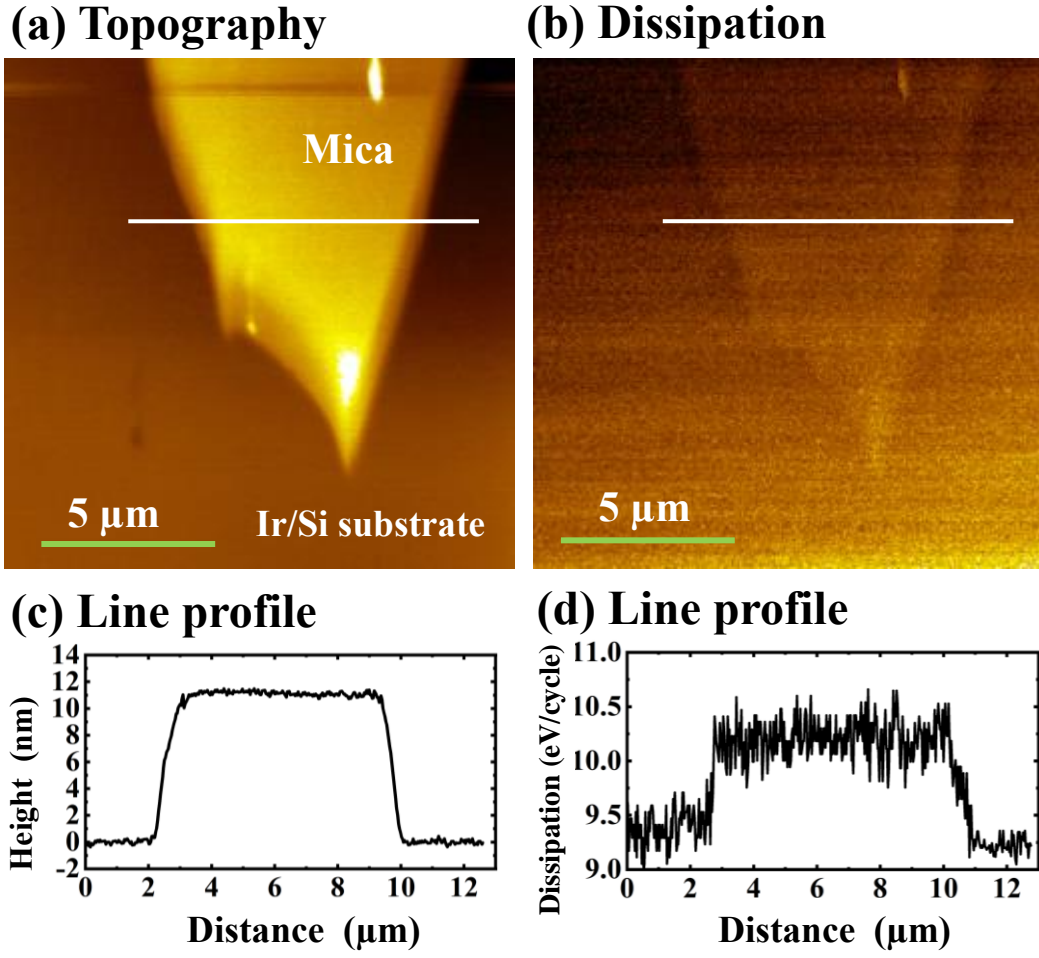
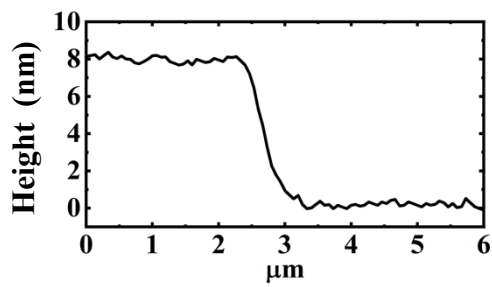
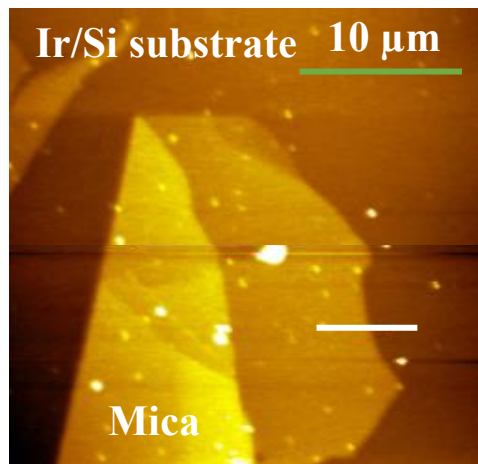
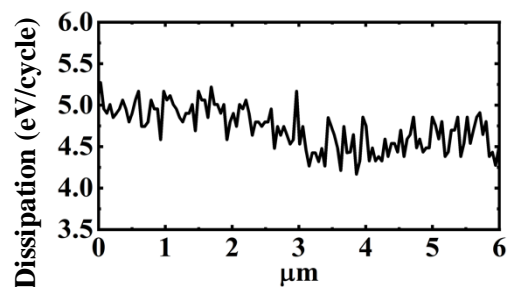
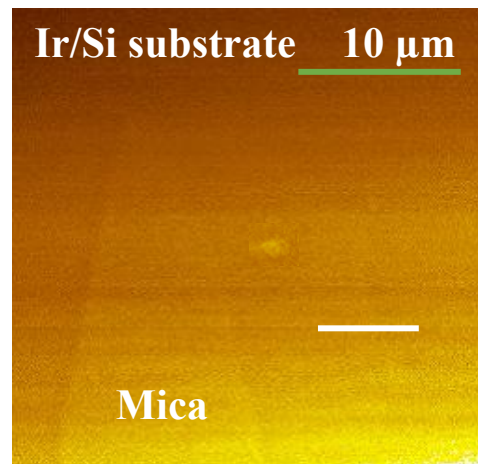


**Fig. 4.4:** (a) FM-AFM topographic image of the mica nanosheets with 11-layer thickness (11 nm) on the Ir/Si substrate in a scan area of  $15\ \mu\text{m} \times 15\ \mu\text{m}$  at  $\Delta f = -45\ \text{Hz}$  and  $V_s = -5.0\ \text{V}$ . (b) dissipation image simultaneously taken with (a). (c) cross-sectional line profile of the height along the line in (a). (d) cross-sectional line profile of the dissipation along the line in (b). The line in (b) is identical to the line in (a) in the planar coordinates.

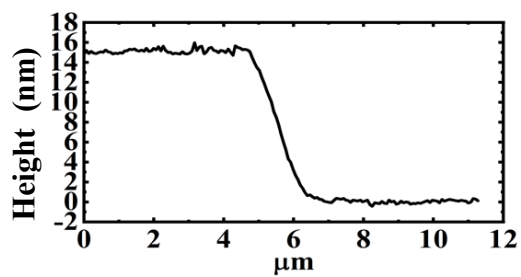
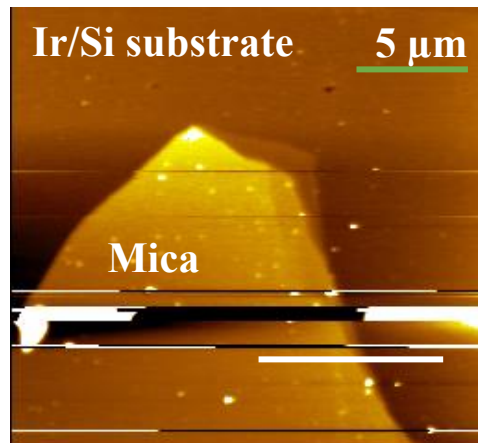
**(a) Topography**



**(b) Dissipation**



**(c) Topography**



**(d) Dissipation**

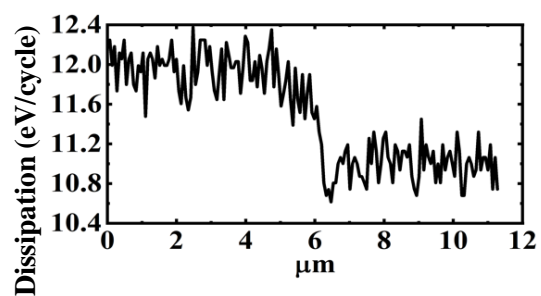
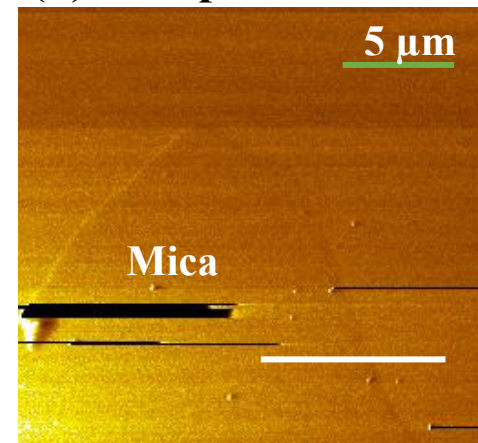


**Fig. 4.5:** (a) FM-AFM topographic image of the mica nanosheets with 8-layer thickness (8 nm) on the Ir/Si substrate in a scan area of  $30\ \mu\text{m} \times 30\ \mu\text{m}$  at  $\Delta f = -60\ \text{Hz}$  and  $V_s = -5.0\ \text{V}$ . (b) dissipation image simultaneously taken with (a). (c) topographic image of the mica nanosheets with 15-layer thickness (15 nm) on the Ir/Si substrate in a scan area of  $35\ \mu\text{m} \times 35\ \mu\text{m}$ . (d) simultaneously taken dissipation image faintly shows 15-layer mica nanosheet. The corresponding line profiles are shown below the images.

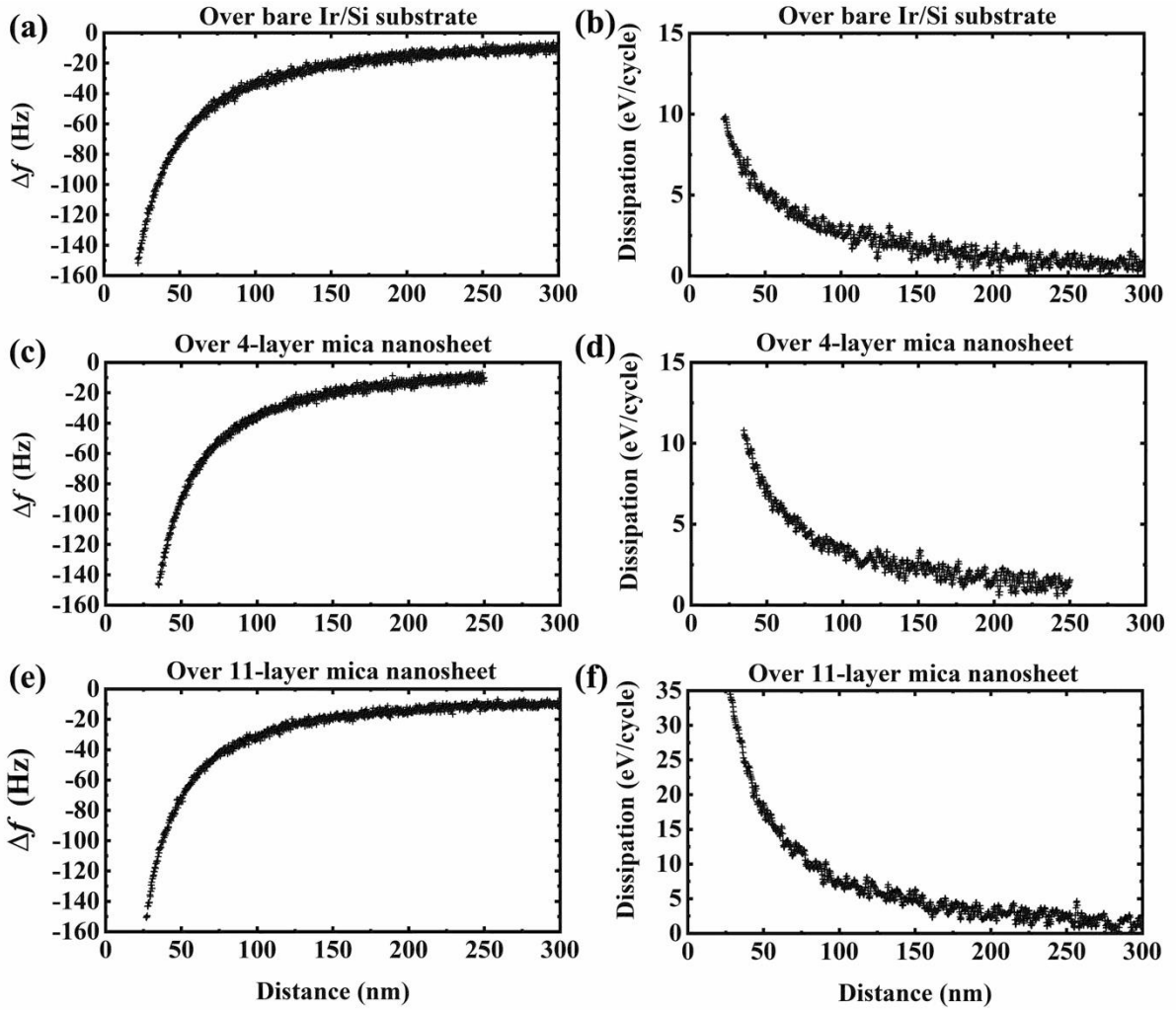


**Fig. 4.6:** (a) and (b) curves of frequency shift ( $\Delta f$ ) and dissipation ( $D_{\text{dis}}$ ) as a function of the tip-sample separation (distance), respectively, taken at a point over the Ir/Si substrate at  $V_s = -5.0\ \text{V}$ , which was far from the mica nanosheets in Fig. 4.3. (c) and (d)  $\Delta f$  and  $D_{\text{dis}}$  as a function of the distance, respectively, taken at a point over the 4-layer mica nanosheet, after the images in Fig. 4.3 were

observed. (e) and (f)  $\Delta f$  and  $D_{\text{dis}}$  as a function of the distance, respectively, taken at a point over the 11-layer mica nanosheet, after the images in Fig. 4.4 were observed.

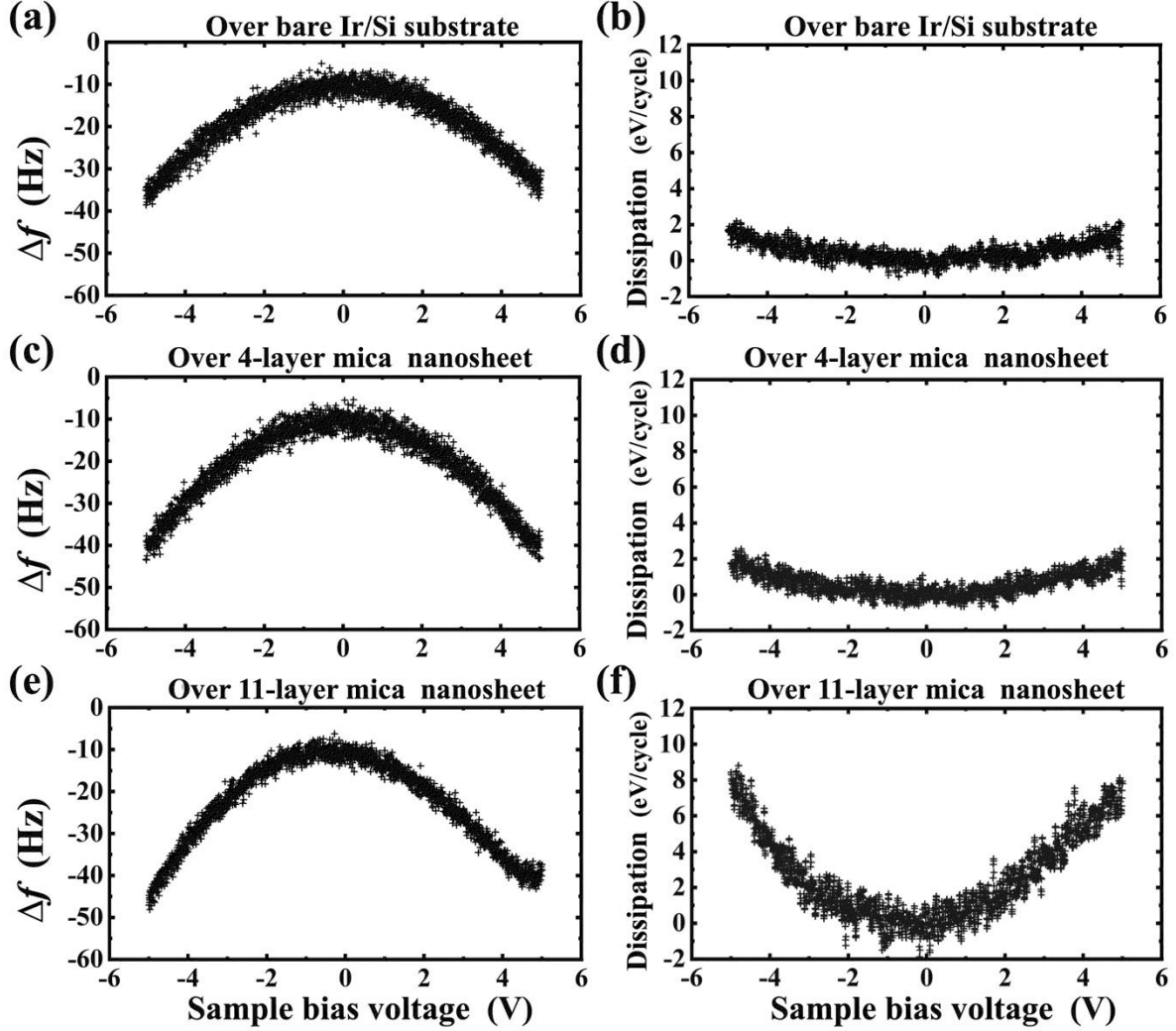


**Fig. 4.7:** (a) and (b). curves of frequency shift ( $\Delta f$ ) and dissipation ( $D_{\text{dis}}$ ) as a function of the sample bias voltage ( $V_s$ ), respectively, taken at a point over the Ir/Si substrate, which was far from the mica nanosheets in Fig. 4.3. (c) and (d).  $\Delta f$  and  $D_{\text{dis}}$  as a function of  $V_s$ , respectively, taken at a point over the 4-layer mica nanosheet, after the images in Fig. 4.3 was observed. (e) and (f).  $\Delta f$  and  $D_{\text{dis}}$  as a function of  $V_s$ , respectively, taken at a point over the 11-layer mica nanosheet, after the images in Fig. 4.4 was observed.

In comparison of the curves in Fig. 4.7, it is noticeable that  $D_{\text{dis}}$  for the 11-layer mica nanosheet more increased with increasing bias voltage than the others in Fig. 4.7, roughly 4 times, while  $\Delta f$

curves looked similar. Then, we looked into the relationship between  $D_J$  and  $\Delta f_{\text{ele}}$ , extracted from  $D_{\text{dis}}$  and  $\Delta f$ , by making the plots of  $D_J$  as a function of  $\Delta f_{\text{ele}}$  as shown in Fig. 4.8. For all samples, including the 8- and 15-layer mica nanosheets,  $D_J$  increased proportionally to  $\Delta f_{\text{ele}}$ , which agreed to the relationship of eq. 33. From the slope of  $D_J$  with respect to  $\Delta f_{\text{ele}}$ , we evaluated the values of  $(R_J + r_m \sin^2 \delta)$  in eq. 33, in which the dependence of the tip-sample separation ( $d$ ) was canceled; the results are summarized in Table I. The value of  $(R_J + r_m \sin^2 \delta)$  did not change much between the Ir/Si substrate and the 4-layer mica nanosheet, which was  $\sim 4 \text{ G}\Omega$ . However, it increased to 6 and 15  $\text{G}\Omega$  as the thickness of mica nanosheet increased from 8-layer to 11-layer. Meanwhile, the value for 15-layer was the same as that of 11-layer. It is worth mentioning that the linear relationship of  $D_J$  with respect to  $\Delta f_{\text{ele}}$  did not change on the polarities of  $\pm(V_S - V_{\text{CPD}})$ , differently for the semiconductor surfaces reported in ref. 32. This implies the metallic surface properties of both of the substrate and tip in the present study, as well as the insulating properties of mica nanosheets, different from semiconducting properties.

**Table I:**  $(R_J + r_m \sin^2 \delta)$  values representing the electrical resistance for Joule heat dissipation, evaluated from the slopes of  $D_J$  with respect to  $\Delta f_{\text{ele}}$  in shown Fig. 4.8. The tip radius ( $r_{\text{tip}}$ ) was assumed to be 25 nm as the nominal value for the calculation of resistance using eq. 33.

Ir/Si substrate	4-layer mica nanosheet	8-layer mica nanosheet	11-layer mica nanosheet	15-layer mica nanosheet
3.8 $\text{G}\Omega$	4.2 $\text{G}\Omega$	6.1 $\text{G}\Omega$	15 $\text{G}\Omega$	15 $\text{G}\Omega$

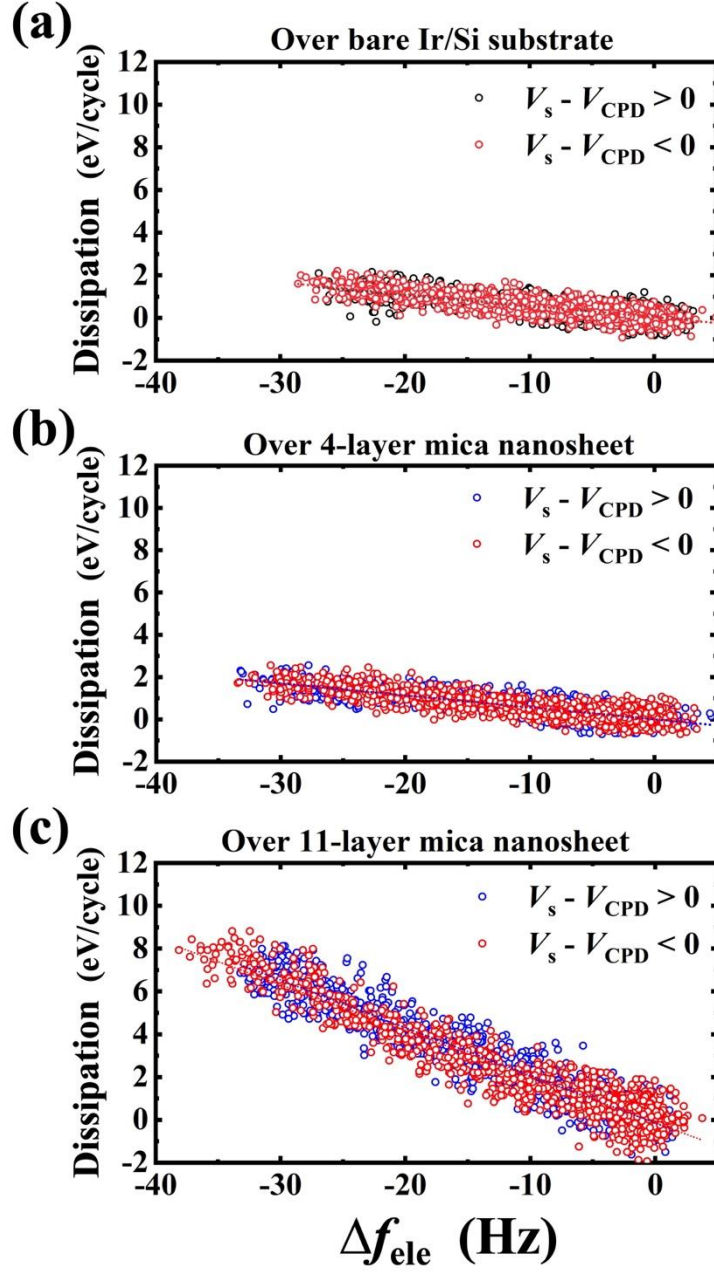


**Fig. 4.8:** Dissipation ( $D_J$ ) as a function of frequency shift ( $\Delta f_{\text{ele}}$ ) due to the electrostatic force: (a) for the Ir/Si substrate, plotted from Figs. 4.7 (a) and (b); (b) for the 4-layer mica nanosheet, plotted from Figs. 4.7 (c) and (d); (c) for the 11-layer mica nanosheet, plotted from Figs. 4.7 (e) and (f). The zeros of  $D_J$  and  $\Delta f_{\text{ele}}$  are adjusted as the values of  $D_{\text{dis}}$  and  $\Delta f$  at  $V_S = V_{\text{CPD}}$  are zero, respectively.

Here, we discuss the origin of electric resistance expressed as  $(R_J + r_m \sin^2 \delta)$ , which is evaluated from the slope of  $D_J$  as a function of  $\Delta f_{\text{ele}}$ . As described in 4.1 Introduction, the oscillating tip under a bias voltage ( $V_S \neq V_{\text{CPD}}$ ) could cause the oscillatory motion of surface charges of the sample and the

tip along their surfaces, as shown in Fig. 4.9, representing the bare Ir/Si substrate with no mica nanosheet. In this case, the resistance term  $(R_J + r_m \sin^2 \delta)$  simply becomes  $R_J$ . The motion of the charge would be scattered by the surface atoms and electrons, resulted in Joule heat through inelastic scattering. The amount of Joule heat is responsible for the mechanical energy dissipation of the oscillating cantilever. Noted that, in the present study, the tip-sample electrical connection via the bias voltage source had a resistance much less than  $G\Omega$ , as the resistance of the Ir/Si substrate was as low as  $10 \text{ k}\Omega$ ; the other parts were connected using conductive wires and films, including the Pt-Ir coated conductive Si cantilever. Therefore, it is deduced that the Joule heat occurred on the surfaces of the tip and the sample.

Next, we estimate the surface resistance responsible for  $R_J$  on the basis of Drude model [40]. According to the model, the resistivity of metal ( $\rho$ ) is expressed as follows:

$$\rho = \frac{m}{ne^2\tau}, \quad (34)$$

where  $n$  is the electron density,  $e$  is the elemental charge of an electron,  $\tau$  is the relaxation time of electron in metal, and  $m$  is the electron effective mass. Then, Joule heat ( $w$ ) per unit volume becomes

$$w = n \frac{mv^2}{\tau} = \frac{m}{ne^2\tau} (nev)^2 = \rho i^2, \quad (35)$$

where  $v$  is the averaged electron velocity, and  $i$  is the electron current density. Here we assume that the charge density ( $n_S$ ) and the relaxation time ( $\tau_S$ ) at the surfaces are different from those in bulk, as well as the resistivity at the surface ( $\rho_S$ ); that is,  $\rho_S = m/(n_S e^2 \tau_S)$ . Then, we can derive the following equation:

$$w = \rho \frac{n}{n_S} \frac{\tau}{\tau_S} i^2. \quad (36)$$

Furthermore, we assume that the current isotropically spreads and converges periodically along the sample surface from the point just under the tip, the Joule heat generated in a volume of a thin ring with radius ( $r$ ), a thin width ( $\Delta r$ ), and a thin thickness ( $h$ ) is expressed as follows, in the frame of cylindrical coordinate system with the axis along the tip:

$$\begin{aligned} \Delta W &= \rho \frac{n}{n_S} \frac{\tau}{\tau_S} i^2 \times 2\pi r (\Delta r) h = \rho \frac{n}{n_S} \frac{\tau}{\tau_S} \left( \frac{I_r}{2\pi r h} \right)^2 \times 2\pi r (\Delta r) h \\ &= \rho \frac{n}{n_S} \frac{\tau}{h \tau_S} I_r^2 \times \frac{\Delta r}{2\pi r} = \rho \frac{n}{\sigma/e} \frac{\tau}{\tau_S} I_r^2 \times \frac{\Delta r}{2\pi r}. \end{aligned} \quad (37)$$

where  $\sigma$  is the surface charge density and  $I_r (=2\pi rh \times i_r)$  is the current perpendicularly passing the circle with radius  $r$  on the surface ( $i_r$  is the radial component of current density). The current  $I_r$  passes dominantly in a surface area of the shape of a donut with an inner diameter size comparable to the tip radius ( $r_{\text{tip}}$ ) and an outer diameter size slightly larger than  $r_{\text{tip}}$ , because the value of  $I_r$  should be zero at  $r=0$ , just under the tip, owing to a finite value of  $i_r$  on the basis of the continuity of equation as  $\frac{1}{r} \frac{\partial(i_r \cdot r)}{\partial r} + \frac{1}{h} \frac{\partial \sigma}{\partial t} = 0$  in the cylindrical coordinate system. Furthermore, the value of  $I_r$  should also be zero at  $r=\infty$ , because the current finally flows into the electrical contact area formed on the sample as an electrode in reality. By integration of eq. 37 over the donut-like region, the total Joule heat  $D_J$  is estimated. By ignoring the geometric factor of  $\Delta r/2\pi r$ ,  $D_J$  is roughly regarded as  $R_J \times I_r^2$ . Then, we derive the equation below:

$$R_J \cong \rho (n/\sigma/e) (\tau/\tau_s). \quad (38)$$

For instance, we approximate  $\sigma \cong \epsilon_0 V_S / d$  for  $d=15$  nm, then  $\sigma/e = \sim 10^{16} \text{ m}^{-2}$ . In general, for metal,  $n = \sim 10^{28} \text{ m}^{-3}$ ,  $\rho = \sim 10^{-8} \Omega \text{ m}$ , and  $\tau = \sim 10^{-14} \text{ sec}$ . Then, for  $R_J = 10^9 \Omega$  that was evaluated of the order of magnitude in our experiments,  $\tau_s$  becomes  $10^{-19} \text{ sec}$ . This value is close to the relaxation time in electrostatic induction for metal, given by  $\epsilon_0 \rho$  [41], which is derived from the continuity of equation along with Ohm's law. This seems reasonable because we observed the oscillatory motion of charges induced the tip oscillation under the bias voltage, which is interpreted as electrostatic induction. Although this is a rough estimation, the surface scattering with  $\tau_s$  of moving charge in a very thin layer at the surface is possibly evaluated locally via the measurement of energy dissipation by the FM-AFM. Significantly, a similar amount of Joule heat is also generated on the surface of the tip. The amount of the heat can be estimated to be of the same order of that on the sample surface, which can be evaluated by changing the coordinate system from the cylindrical one for the flat sample surface to the spherical coordinate system for the tip apex. It should be noted that the evaluated value of  $R_J$  is the sum of the Joule heat at the surfaces of the tip and the sample. At present we have no experimental method to distinguish the Joule heat at the sample from that at the tip, but the local variation of Joule heat over the sample surface can be probed by use of the same tip.

In the measurement of energy dissipation for the 4-layer mica nanosheet (Fig. 4.3), the value of  $(R_J + r_m \sin^2 \delta)$  was almost the same as that over the bare Ir/Si substrate. This indicates that the Joule heat at the interface between the 4-layer mica nanosheet and the bare Ir/Si substrate did not change so much in comparison with that on the bare Ir/Si substrate. It is deduced that the inelastic scattering characteristics at the interface, e.g.,  $\tau_s$ , would be close to that at the surface of Ir/Si substrate



according to eq. 38, because  $\sigma$  does not change much for coverage with the very thin mica nanosheet as a dielectric layer. In our experiment, the sample surface and the tip surface were possibly covered with hydrocarbons, so that the inelastic scattering might be governed by the hydrocarbon layer, which likely existed between the mica nanosheet and the Ir/Si substrate. It implies that the high value of  $R_I$  reflects the frequent degree of inelastic scattering at the interfaces, where the symmetric and periodic structural conditions are broken and contact methods such as multi-probes cannot directly explore because the probes inject the carriers through the contact regions; the injected carriers tend to run into a path slightly deeper from the interface, seeking a minimum resistance path from the probe to another probe.

Here, we note the features of the FM-AFM observation for the mica nanosheets. Under a strong attractive electrostatic force, it can be regarded that  $\Delta f_{\text{ele}}$  over no mica nanosheet equals  $\Delta f_{\text{ele}}$  over the mica nanosheet during the FM-AFM scanning in the constant  $\Delta f$  mode. Equation 31 shows that  $\Delta f_{\text{ele}}$  is a function of  $(d + h/\epsilon_r)$ , where  $d$  is the minimum separation between the tip and the sample surface, and  $h$  is the thickness of the mica nanosheet. Here, we define  $d_{\text{Ir}}$  as the minimum separation over the bare Ir/Si substrate, namely for the case of  $h=0$ , and  $d_m$  as the minimum separation over the mica nanosheet. Then, from  $\Delta f_{\text{ele}}(d_{\text{Ir}}) = \Delta f_{\text{ele}}(d_m + h/\epsilon_r)$ , we can extract the relationship of  $d_{\text{Ir}} = d_m + h/\epsilon_r$ , under almost constant of the term of  $(V_S - V_{\text{CPD}})$  in this study. This relationship indicates that the tip-sample capacitance averaged over the cantilever oscillation is regarded as constant during the scanning.<sup>40)</sup> Accordingly, to discuss the effect of coverage with the mica nanosheets on the dissipation in the next paragraph, we will adopt the condition of the constant capacitance. In addition, it is worth mentioning that the topographic height difference between the Ir/Si substrate and the mica nanosheet is calculated as  $(d_m + h) - d_{\text{Ir}} = h - h/\epsilon_r = h(1 - 1/\epsilon_r)$ , which is measured from the surface of the substrate (Fig. 4.2 (a)). This means that the thickness of the mica nanosheet could be evaluated to be less by a factor of  $(1 - 1/\epsilon_r)$ . For the mica with  $\epsilon_r=7$ , the thickness would be underestimated by about 14%. In fact, because  $\Delta f$  includes the effect of the attractive van der Waals forces, the factor would be less. In this study, we presented the thickness of the mica nanosheets evaluated from the raw measured height difference.

The value of  $(R_I + r_m \sin^2 \delta)$  increased with the increase in thickness of the mica nanosheet up to 11 layers; the value for 8 layers was 6.1 G $\Omega$  and the values for 11 and 15 layers were 15 G $\Omega$ , as summarized in Table I. We took the data consecutively from the bare Ir/Si substrate with the same tip, and finally, the value for the bare Ir/Si substrate was confirmed to be  $\sim 4$  G $\Omega$ , which was the same value at the beginning of the measurement. This means that the tip did not change much during the

measurements. Accordingly, the increase in  $(R_J + r_m \sin^2 \delta)$  could be attributed to the properties of the thicker mica nanosheets. As described in the section of Experimental methods, the electric dipoles in the mica nanosheets as a dielectric are forced to be parallel to the electric field under the tip and respond to the field alternating at high frequency. The directional change of dipoles in the mica nanosheet by the tip oscillation would be mostly elastic. However, since the dipoles do not instantly respond to the change of the electric field, the time delay causes energy dissipation. It is known that the dielectric energy loss of phlogopite is about 0.2 % or less as  $\tan \delta$  in the frequency range of 200 – 400 kHz [44, 45].

As tabulated in Table I, the values of  $(R_J + r_m \sin^2 \delta)$  for 4-, 8-, 11-, and 15-layer mica nanosheets tended to increase with their thickness, though the increase was not uniform. Assuming that each mica layer has the same value of  $r_m$  and  $\sin^2 \delta$  is  $4 \times 10^{-6}$ , the average value of  $r_m$  per one layer for those samples was estimated to be  $0.16 \times 10^6 \text{ G}\Omega$  from the differences from the value of  $R_J$  for the Ir/Si substrate. Since  $\tan \delta = 1/(\omega r_m C_m)$  ( $= 2 \times 10^{-3}$ ),  $C_m$  for the one-layer mica nanosheet is evaluated to be  $\sim 2 \text{ aF}$  for  $\omega = 2\pi f_0 = 2\pi \times (265.8 \text{ kHz})$  as the fundamental frequency of the cantilever oscillation, though the displacement current  $I_d$ , passing between the tip and the sample (Fig. 4.2 (b)), contained integer multiples of the frequency of  $f_0$  as  $I_d = dC(z)/dt$ , where  $z = d + (1+A) \times \cos(2\pi f_0 t)$  [32]. Using a parallel capacitor model,  $C_m = \epsilon_0 \epsilon_r (\text{area}/h)$ , the value of area is roughly estimated as  $\sim (6 \text{ nm})^2$ . Although the tip radius is larger than 6 nm, the estimated value of  $C_m$  is plausible for our tip-sample system. On the other hand, if the value of  $C_m$  is measured, for example, using scanning capacitance microscopy (SCaM) techniques [46], independently from the measurement of the dissipation energy,  $\tan \delta$  representing the feature of dielectric energy loss can be evaluated using the value of  $r_m \sin^2 \delta$  as measured in this study. In general,  $\tan \delta$  is very small, so  $\tan \delta \approx \sin \delta$ . Under this approximation,  $\tan \delta$  would be evaluated with the values of  $(r_m \sin^2 \delta)$  and  $C_m$  as below. First, we obtain the following equation:

$$\tan \delta = \frac{1}{\omega r_m C_m} = 1/(\omega (r_m \sin^2 \delta) C_m) / \sin^2 \delta. \quad (39)$$

So, eq. 39 can be changed as below:

$$\tan \delta \sin^{-2} \delta = 1/(\omega (r_m \sin^2 \delta) C_m). \quad (40)$$

Since  $(\tan \delta \sin^{-2} \delta) \approx \tan^{-1} \delta$  under the approximation of small  $\delta$ , we obtain the equation for  $\tan \delta$ ,

$$\tan \delta = \omega C_m (r_m \sin^2 \delta). \quad (41)$$

Although at present we did not get the value of  $C_m$ , the FM-AFM with the capability of measurement of the dissipation energy, combined with SCAm techniques, would be a powerful tool to probe the local electronic properties for such composite devices covered with dielectric ultra-thin films.

According to ref. 47, the potassium (K) layer between the tetrahedral and octahedral layers of aluminosilicate and magnesia of phlogopite could contribute to the dielectric energy loss, through the jump of K ions responding to the change in an electric field. The K layer is the cleavable plane of the mica, and the binding force between the tetrahedral and octahedral layers with a separation of  $\sim 0.35$  nm is weak. The K atoms would slightly move in the separation under the alternating electric field with a time delay, resulting in dielectric energy loss. In addition, the mica exhibits the intercalation of impurity ions and water molecules in the separation, though the artificially synthesized phlogopite is purer than natural micas. Those intercalated impurities might also contribute to the energy loss. For further analysis of their contribution to the energy loss, it is crucial to control the purity of the sample in the preparation processes. Although the mechanism of increase of the dissipation with the thickness of mica nanosheets is not fully understood at present, the dissipation measurement using the FM-AFM has the potential to study the nanoscale properties of metallic and dielectric materials on a nanoscale, through the dynamic behaviors of materials responding to the tip oscillation.

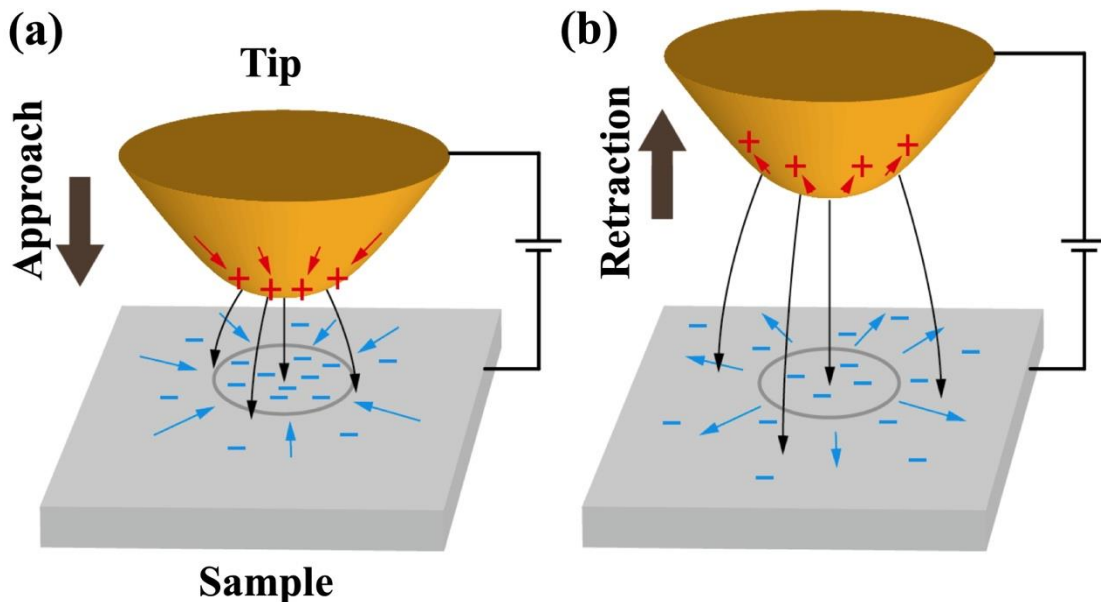


**Fig. 4.9:** Schematic illustration of the surface charges on the sample and the tip, moved by the oscillating tip under a bias voltage. (a) tip approaches to the sample surface. (b) tip retracts from the sample surface. The motion of the surface charges results in current flow on the sample surface in axial symmetry with the tip axis. The grey ring on the surface shows the virtual region to calculate the symmetric surface current passing through it using the continuity of equation. On the surface of the tip, the current flows approximately in the spherical symmetry.

## 4.4 Conclusions:

We measured the mechanical energy dissipation using the FM-AFM with the conductive Si tip coated with Pt-Ir for the Ir-coated Si substrate partly covered with the mica nanosheets having different thicknesses while observing FM-AFM topographic images. The dissipation images simultaneously obtained with the topographic images showed no contrast for the 4-layer mica nanosheet with respect to the substrate, but faint contrast for the thicker mica nanosheets. We measured the curves of Joule heat ( $D_J$ ) and the resonance frequency shift ( $\Delta f_{\text{ele}}$ ) due to long-range electrostatic force as a function of the sample bias voltage. The plots of  $D_J$  as a function of  $\Delta f_{\text{ele}}$  derived from the curves evidently showed the linear relationship for all samples with the mica nanosheets with different thicknesses. The importance of the equation expressing the linear relationship between  $D_J$  and  $\Delta f_{\text{ele}}$  lies in the independence from the tip-sample separation and the bias voltage for the analysis of the surface and interface electronic properties. From the slopes, we evaluated the resistance value of  $(R_J + r_m \sin^2 \delta)$  representing the dissipation energy to heat; which was of the order of magnitude of  $G\Omega$ , and tended to increase with increasing thickness of the mica nanosheets. We discussed the large values of the resistance in terms of surface scattering of charges along the surface, which were moved by the oscillating tip under a bias voltage, and the dielectric energy loss in the mica films. Through this study, we emphasize that the mechanical energy dissipation channel of the FM-AFM with a conductive tip under a bias voltage has the potential to reveal the nanoscale electronic properties at surfaces and interfaces via long-range electrostatic interaction in non-contact.

**Appendix I: Evaluation of the excitation of cantilever oscillation in our FM-AFM setup via transfer function**

In order to accurately measure the mechanical energy dissipation through nonconservative forces acting between a sample and a tip on the oscillating cantilever in an FM-AFM, it should be recommended to assess the efficiency of excitation of the cantilever oscillation in the FM-AFM setup in terms of a transfer function, where the cantilever is conventionally oscillated mechanically via a vibrating piezo element (piezoacoustic excitation) as in this study. Because the mechanical coupling between the cantilever and the piezo element is not always perfect as a rigid body, spurious features in the frequency mechanical response often appear; for example, some specified frequencies of the excitation signal to vibrate the piezo element extraordinarily enhance the excitation of the cantilever oscillation, which could lead us to measure false “apparent” damping.<sup>38)</sup> Because the specified enhancement enlarges the magnitude of the excitation even if the true damping (dissipation) to be measured is constant, the evaluated dissipation looks less under the feedback condition of constant amplitude of the cantilever oscillation. Such mechanical features can be evaluated in terms of the amplitude transfer function ( $T(f)$ ) as a function of frequency ( $f$ ), which is defined as the ratio of the amplitude of cantilever oscillation ( $A(f)$ ) with respect to the amplitude of piezo excitation signal ( $V_{\text{ext}}(f)$ ). The transfer function  $T(f)$  sometimes shows forest peaks as a function of  $f$ . Here, we show that  $T(f)$  in our setup exhibited a flat feature over the frequency range for the data in the main text, which was derived by the following experimental procedures referring to the protocol proposed by Labuda et al [38].

1. First, the cantilever used in this study was acoustically excited via the piezo element at a far tip–sample separation. After the tip was brought closer to the sample using the FM-AFM setup, the distance feedback controller of the setup was inactivated to fix the tip position. Subsequently, the tip was lifted up several tens of nanometers.
2. The piezoacoustic excitation was stopped, and a sinusoidal voltage signal was applied to the sample, which caused alternating electrostatic forces between the tip and the sample, to excite the cantilever oscillation. While the resonance frequency was searched by sweeping the frequency of the electrostatic excitation, the amplitude of the sinusoidal voltage signal ( $V_{\text{ext}}$ ) at the resonance was adjusted so as to give almost the same amplitude of cantilever oscillation as that by the piezoacoustic excitation ( $A = 20$  nm and  $V_{\text{ext}} = 8.5$  V in this study). The resonance frequency was 264.8 kHz, lower than  $f_0 = 265.8$  kHz at the far tip–sample separation under a sample bias voltage of 0 V. Because the excitation via the electrostatic excitation at the frequency ( $\nu$ ) was not enough to successfully excite the cantilever oscillation at  $f = \nu$  owing to the output limitation of our voltage source for the sinusoidal signal (noted that the

electrostatic force is proportional to  $(V_{\text{ext}} \cos(2\pi\nu t) - V_{\text{CPD}})^2$ , and  $V_{\text{CPD}} \approx 0$  V in this study), we used the doubled frequency ( $2\nu$ ) of the electrostatic excitation to excite the cantilever oscillation at  $f = 2\nu$ .

3. The amplitude responses as a function of  $f$  were measured by the sweep of frequency ( $\nu$ ) of electrostatic excitation. To infer the detailed response, the sweeping ranges for  $f (= 2\nu)$  were set to 240–290 kHz as wide, 264–267 kHz as middle, and 265–266.4 kHz as narrow.
4. Next, we changed the excitation from electrostatic to piezoacoustic. The sample bias voltage ( $V_s$ ) was adjusted as the frequency at the peak amplitude of cantilever oscillation became almost the same as the peak frequency by electrostatic excitation;  $V_s$  was found to be  $-3.0$  V. Subsequently, we swept the frequency  $f$  from 240 to 290 kHz as wide, 264–267 kHz as middle, and 265–266.4 kHz as narrow, similarly to item 3.
5. To derive the amplitude transfer function as a function of frequency for the middle and narrow frequency ranges, we divided the measured amplitude of cantilever oscillation in the acoustic excitation by that in the electrostatic excitation at the same frequency, after eliminating the floor noise as described below.

Figures A1 (a) and (b) show the measured root-mean-square amplitude responses as a function of the frequency for the wide range. For the electrostatic excitation, the value of excitation frequency for the x-axis was doubled as  $f = 2\nu$ . For a forced harmonic oscillator with damping, the measured root-mean-square amplitude  $A_{\text{rms}}(f)$  at frequency  $f$  is expressed as below:

$$A_{\text{rms}}(f) = \sqrt{\frac{F^2}{2k^2 \left[ \left\{ 1 - \left( \frac{f}{f_0} \right)^2 \right\}^2 + \left( \frac{f}{f_0 Q} \right)^2 \right]} + n^2}, \quad (\text{A-1})$$

where  $F$  is the amplitude of the force to excite the cantilever,  $k$  is the spring constant of cantilever, and  $n$  is the floor noise. The measured amplitude responses were numerically fitted to eq. A-1 using fitting parameters of  $F/k$ ,  $f_0$ ,  $Q$ , and  $n$ , as shown in the red solid lines in Fig. A1 (a) and (b); the floor noise  $n$  was estimated to be approximately 1.3 nm. The amplitude response for the electrostatic excitation shows a better agreement to the fitted curve, in particular, around the peak tails, compared with that for the piezoacoustic. This means that the electrostatic excitation holds the advantage to extract the transfer function as an ideal excitation method without spurious features, as proposed by Labuda et al [38].

Figures A1(c) and (d) show the measured root-mean-square amplitude responses for the middle and narrow frequency ranges, and the derived amplitude transfer functions, which were calculated

after the floor noise  $n$  was subtracted using eq. A-1 and normalized to be one at the intrinsic frequency  $f_0$  of 268.5 kHz. In the main text, the concerning frequency range for our examination of the dissipation was from  $f_0$  to  $f_0 - 50$  Hz. In the range, the transfer function exhibits flat with random noise (see Fig. A1 (d)). This indicates that the piezoacoustic excitation in our FM-AFM setup did not provide apparent damping much, which would be less than the noise level. That is, the correction prefactor could be regarded as one in the frequency range. Although the phase transfer function could also give the apparent damping through a sine term in the prefactor, the effect would be ignored in our study, because the phase shift measured in the frequency range of 50 Hz below  $f_0$  was around  $1^\circ$  [38].

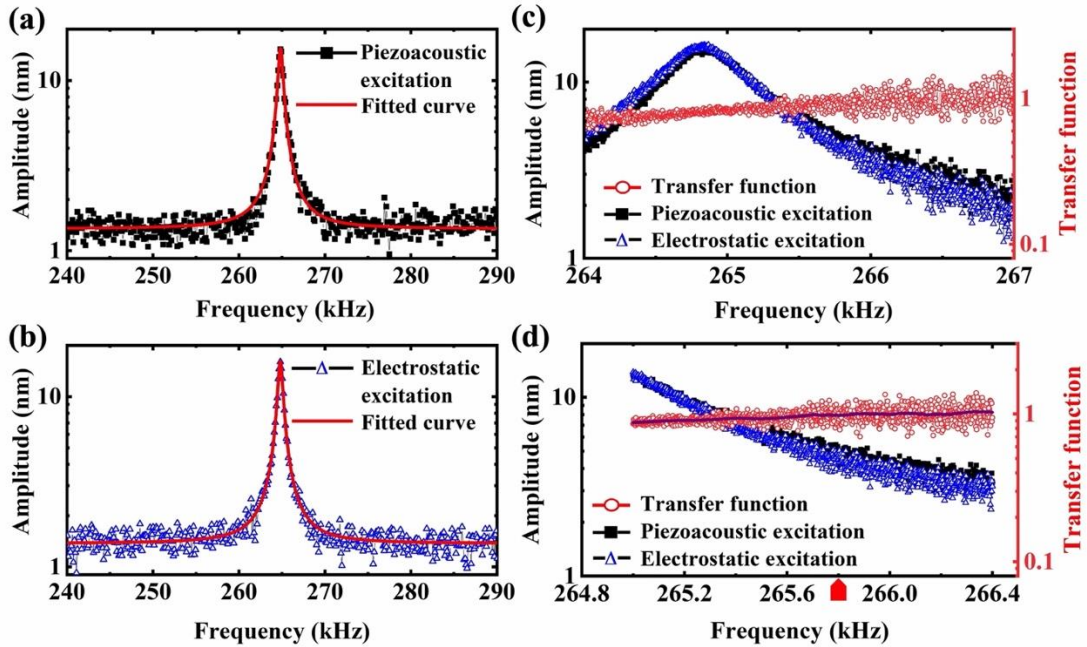


**Fig. A1.** (a) and (b) root-mean-square amplitude responses of the cantilever as a function of frequency for excitation by piezoacoustic and electrostatic, respectively, in the wide frequency range. The red curves show the curves fitted to the responses using eq. A-1. (c) and (d) root-mean-square amplitude responses in the middle and the narrow frequency ranges, respectively, and the amplitude transfer functions derived from the ratio of the response by piezoacoustic to that by electrostatic. The black rectangle symbols denote the plots by piezoacoustic excitation, the blue triangles denote the plots by electrostatic excitation, and the red circles denote the transfer functions. The smoothed transfer function is shown by the purple solid line in (d). The red arrow below the lateral axis indicates the intrinsic cantilever frequency of  $f_0 = 265.8$  kHz.

## Appendix II: Contribution to $D_J$ from mica nanosheets with dielectric energy loss using an equivalent circuit

To represent the electrical response of the dielectric thin film (mica nanosheet in this study) on a metal substrate, an equivalent circuit diagram, as shown in Fig. 1(b), can be used with a capacitor of  $C_m$  with a parallel resistor of  $r_m$ . In Fig. 1(b), we denote the gap between the tip and the surface of the mica nanosheet by a capacitor of  $C_{\text{gap}}$ . We assume that the alternating displacement current  $I_d$  with angular frequency  $\omega$  passes through the circuit, which is induced by the tip oscillation over the mica nanosheet. Then, the equation of  $\tan\delta=1/(\omega r_m C_m)$  that expresses the degree of dielectric energy loss can be derived from the resultant impedance of the equivalent circuit of the mica nanosheet. The displacement current  $I_d$  passing  $C_{\text{gap}}$  is divided into  $I_{C_m}$  and  $I_{r_m}$ , which are the currents passing in  $C_m$  and  $r_m$ , respectively, as  $I_d = I_{C_m} + I_{r_m}$ . The resistance value of  $r_m$  is much larger than the impedance value of the capacitor of mica nanosheet as  $1/(\omega C_m)$ , because  $\tan\delta$  is known to be about 0.2 % or less for the phlogopite in the frequency range of 200 – 400 kHz.<sup>44,45)</sup> Accordingly, we can approximate the current of  $I_d$  as the current passing in the series circuit of  $C_{\text{gap}}$  and  $C_m$ . Namely, the current of  $I_d$  is given by  $dC/dt \times (V_S - V_{\text{CPD}})$ , as appeared in eq. 2 in the main text, where  $1/C = 1/C_{\text{gap}} + 1/C_m$ . Meanwhile, the current of  $I_{r_m}$  can be expressed as

$$I_{r_m} = I_d \frac{1-j\omega r_m C_m}{1+(\omega r_m C_m)^2} = I_d \frac{1-j\frac{1}{\tan\delta}}{1+\frac{1}{\tan^2\delta}} = I_d \sin\delta (\sin\delta - j \cos\delta), \quad (\text{A-2})$$

where  $j$  is the unit of an imaginary number. Thus, the dissipated power  $P$  at the mica nanosheet is expressed as

$$P = r_m I_{r_m} I_{r_m}^* = r_m |I_d|^2 \sin^2 \delta, \quad (\text{A-3})$$

where  $I^*$  is the complex conjugate of  $I$ . By referring to eq. 2 describing the Joule heat for the bare Ir/Si substrate, the above dissipation power  $P$  can be inserted into eq. 2 as an additional term as follows:

$$D_J = \int_0^{\frac{1}{2}} I_d^2 (R_J + r_m \sin^2 \delta) dt. \quad (\text{A-4})$$

After all, the term of  $R_J$  in eq. 7 can be replaced by  $(R_J + r_m \sin^2 \delta)$  for the coverage with the mica nanosheet:

$$D_J = -16\pi^3 \varepsilon_0 k A^2 r_{\text{tip}} (R_J + r_m \sin^2 \delta) \times \Delta f_{\text{ele}}. \quad (\text{A-5})$$



It is noted that  $\sin^2\delta$  becomes as small as  $4\times 10^{-6}$ , because  $\delta$  for the mica is very small as  $\tan\delta \sim 0.2\%$  [44, 45].

## References:

- [1] G. Binnig, C. F. Quate, and Ch. Gerber, Phys. Rev. Lett. **56**, (1986) 930–933.
- [2] K. Shin-ichi and M. Iwatsuki, Jpn. J. Appl. Phys. **34**, (1995) L145–L148.
- [3] F. J. Giessibl, Science **267**, (1995) 68–70.
- [4] A. S. Foster, C. Barth, A. L. Shluger, and M. Reichling, Phys. Rev. Lett. **86**, (2001) 2373–2376.
- [5] S. Nishimura, S. Biggs, P.J. Scales, T.W. Healy, K. Tsunematsu, T. Tateyama, Langmuir **10** (1994) 4554–4559.
- [6] J. Yin, C.D. Haese, B. Nysten, Appl. Surf. Sci. **330** (2015) 65–73.
- [7] Y. Martin, D.W. Abraham, H.K. Wickramasinghe, Appl. Phys. Lett. **52** (1988) 1103–1105.
- [8] L. Jiang, J. Weber, F.M. Puglisi, P. Pavan, L. Larcher, W. Frammelsberger, G. Benstetter, M. Lanza, Materials **12** (2019) 1–10.
- [9] M.P. Boneschanscher, J. Van Der Lit, Z. Sun, I. Swart, P. Liljeroth, D. Vanmaekelbergh, ACS Nano **6** (2012) 10216–10221.
- [10] S. Patil, A. V. Kulkarni, C.V. Dharmadhikari, J. Appl. Phys. **88** (2000) 6940–6942.
- [11] B. Gotsmann, C. Seidel, B. Anczykowski, H. Fuchs, Phys. Rev. B **60** (1999) 11051–11061.
- [12] T.R. Albrecht, P. Grütter, D. Horne, D. Rugar, J. Appl. Phys. **69** (1991) 668–673.
- [13] M. Bammerlin, R. Lüthi, E. Meyer, A. Baratoff, J. Lü, M. Guggisberg, C. Loppacher, C. Gerber, H.J. Güntherodt, Appl. Phys. A Mater. Sci. Process. **66** (1998) 293–294.
- [14] J.B. Pethica, Phys. Rev. Lett. **57** (1986) 3235.
- [15] R. Bennewitz, T. Gyalog, M. Guggisberg, M. Bammerlin, E. Meyer, H.J. Güntherodt, Phys. Rev. B **60** (1999) R11301–R11304.
- [16] B. Gotsmann, B. Anczykowski, C. Seidel, and H. Fuchs, Appl. Surf. Sci. **140**, 314 (1999).

- [17] S. Hudlet, M. Saint Jean, B. Roulet, J. Berger, C. Guthmann, J. Phys. I 4 (1994) 1725–1742.
- [18] H. Hölscher, B. Gotsmann, W. Allers, U. D. Schwarz, R. Wiesendanger, and H. Fuchs, Phys. Rev. B **64**, 075402 (2001).
- [19] U. Dürig, Surf. Interface Anal. 27 (1999) 467–473.
- [20] C. Loppacher, R. Bennewitz, O. Pfeiffer, M. Guggisberg, M. Bammerlin, S. Schär, V. Barwich, A. Baratoff, E. Meyer, Phys. Rev. B - Condens. Matter Mater. Phys. 62 (2000) 13674–13679.
- [21] T. Arai, R. Inamura, D. Kura, M. Tomitori, Phys. Rev. B 97 (2018) 115428–115434.
- [22] T.D. Stowe, T.W. Kenny, D.J. Thomson, D. Rugar, Appl. Phys. Lett. 75 (1999) 2785–2787.
- [23] O. Pfeiffer, L. Nony, R. Bennewitz, A. Baratoff, E. Meyer, Nanotechnology 15 (2004) S101–S107.
- [24] A.A. Farrell, T. Fukuma, T. Uchihashi, E.R. Kay, G. Bottari, D.A. Leigh, H. Yamada, S.P. Jarvis, Phys. Rev. B Phys. 72 (2005) 1–6.
- [25] S. Morita, R. Wiesendanger, and E. Meyer, *Noncontact Atomic Force Microscopy* (Springer, Heidelberg, 2002).
- [26] H. Yoshizawa, Y.L. Chen, J. Israelachvili, J. Phys. Chem. 97 (1993) 4128–4140.
- [27] G. Cross, A. Schirmeisen, A. Stalder, P. Grütter, M. Tschudy, U. Dürig, Phys. Rev. Lett. 80 (1998) 4685–4688.
- [28] N. Oyabu, P. Pou, Y. Sugimoto, P. Jelinek, M. Abe, S. Morita, R. Pérez, Ó. Custance, Phys. Rev. Lett. 96 (2006) 106101–106105.
- [29] T. Fukuma, K. Umeda, K. Kobayashi, H. Yamada, K. Matsushige, Japanese J. Appl. Physics, Part 1 Regul. Pap. Short Notes Rev. Pap. 41 (2002) 4903–4907.
- [30] W. Denk, D.W. Pohl, Appl. Phys. Lett. 59 (1991) 2171–2173.
- [31] M. Guggisberg, M. Bammerlin, C. Loppacher, O. Pfeiffer, A. Abdurixit, V. Barwich, R. Bennewitz, A. Baratoff, E. Meyer, H. Güntherodt, Phys. Rev. B - Condens. Matter Mater. Phys. 61 (2000) 11151–11155.
- [32] T. Arai, D. Kura, R. Inamura, M. Tomitori, Jpn. J. Appl. Phys. 57 (2018) 08NB04-1–6.

- [33] A. Castellanos-Gomez, M. Wojtaszek, N. Tombros, N. Agraït, B.J. Van Wees, G. Rubio-Bollinger, *Small* **7** (2011) 2491–2497.
- [34] H. Tanaka, M. Taniguchi, *Jpn. J. Appl. Phys.* **58** (2019) 078003–078007.
- [35] M.R. Islam, M. Tomitori, *Appl. Surf. Sci.* **532** (2020) 147388–147401.
- [36] M.R. Islam, M. Tomitori, *Appl. Phys. Express* **13** (2020) 106502–106509.
- [37] J.E. Sader, S.P. Jarvis, *Appl. Phys. Lett.* **84** (2004) 1801–1803.
- [38] A. Labuda, Y. Miyahara, L. Cockins, and P. H. Grütter, *Phys. Rev. B* **84**, (2011) 125433–125444.
- [39] S. Hudlet, M. Saint Jean, C. Guthmann, and J. Berger, *Eur. Phys. J. B* **2**, (1998) 5–10.
- [40] G. Gomila, J. Toset, and L. Fumagalli, *J. Appl. Phys.* **104**, (2008) 024315–024323.
- [41] F. Ostendorf, C. Schmitz, S. Hirth, A. Kühnle, J. J. Kolodziej, and M. Reichling, *Nanotechnology* **19**, (2008) 305705–305711.
- [42] N. W. Ashcroft and N. D. Mermin, *Solid State Physics* (Saunders College, Philadelphia, 1976).
- [43] B. I. Bleaney and B. Bleaney, *Electricity and Magnetism* (Oxford Univ. Press, Oxford, 1976).
- [44] T. Noda, *J. Am. Ceram. Soc.* **38**, (1955) 147–152.
- [45] S. Kaur, S. Singh, L. Singh, and S.P. Lochab, *Nucl. Instrum. Meth. Phys. Res. B* **301**, (2013) 17–22.
- [46] J.R. Matey and J. Blanc, *J. Appl. Phys.* **57**, (1985) 1437–1444.
- [47] S. Taruta, R. Obara, N. Takusagawa, and K. Kitajima, *J. Mater. Sci.* **40**, (2005) 5597–5602.

## Chapter 5: Summarization and Future Prospects

### 5.1 Summary:

The summary of our entire research work is as follows –

We have measured the mechanical energy dissipation of an oscillating cantilever at a range where the long-range attractive forces were crucial for an Ir-coated conductive Si (Ir/Si) substrate partially covered with mica nanosheet for varying thicknesses under a sample bias voltage using FM-AFM. The discrete thickness of the mica nanosheet with apparently larger dimensions was exfoliated mechanically. The topographic imaging and dissipation mapping were performed simultaneously over the bare Ir/Si surface and the mica regime containing 4-, 8-, 11- and 15-layer nanosheet. When we observed a very sharp topographic contrast allowing us to measure the mica height accurately as well as with notable features between bare Ir/Si and mica layers specified above; here, however, the dissipation was faintly appeared for only the thicker mica layers (i.e., 11- and 15-layer) with a trend to be increased in dissipation concurrently with the increasing thickness. At imaging  $\Delta f$  where the separation gap between tip and sample was measured with few tens of nanometer,  $\sim 1\text{ nN}$  force was estimated numerically responsible for long-range interaction.

To justify the thickness-dependent energy dissipation frequently appeared in dissipation images, and to find out the dominancy between long-range electrostatic and van der Waals interactions, we measured the bias-dependent frequency shift ( $\Delta f$ ) and dissipation curves ( $D_{\text{dis}}$ ) using spectroscopy; separately and consecutively (started from Ir/Si and then on mica layers) for all layers. All the bias voltage-dependent curves showed parabolic behavior by keeping their maxima and minima at contact potential difference (CPD) estimated by fitting with the typical parabolic equations for the corresponding surfaces. We observed a similarity in dissipation plots between the thin mica layers (4-layer mica) and bare Ir/Si substrate even experimented separately. In comparison, the parabolic behavior became sharper for 8-, 11-, and 15-layer nanosheets for almost the same  $\Delta f$  from where the quantitative energy dissipation was calculated for each layer. This supports the appearance of energy dissipation (or faint contrast) related to the thick mica layer in the dissipation images summarized in the first paragraph.

As it is recognized that the van der Waals (vdW) interaction is independent of bias voltage, therefore, we subtracted the offset value containing vdW and short-range interactions to get the pure electrostatic ( $\Delta f_{\text{ele}}$ ) contribution and the corresponding energy dissipation which is regarded as Joule heat ( $D_J$ ). Additionally, from our experiment after minimization of vdW, we found almost zero dissipation at  $V_{\text{CPD}}$  which concludes that almost no effect of vdW for energy dissipation.

Finally, we considered the characteristics between  $\Delta f_{\text{ele}}$  and  $D_J$  where we avoided the distance and bias dependence. Our results showed that a linear relationship is constant for all layers as well as bare Ir/Si except without the slope of the line. As a result, we calculated the slope to get the surface resistance ( $R_J$ ) using dissipation equation which in this case in the order of  $G\Omega$  and is responsible for Joule heat generation, numerically lower for bare Ir/Si and thin mica sheet but tends to be increased for thick layer. Based on Drude model established for the metallic sample and using the continuity equation of current, we showed that our measured resistance ( $R_J$ ) is valid because the surface relaxation time ( $\tau_s$ ) estimated for electron movement using our calculated resistance supports electrostatic induction. Even though the mica is being considered as a lossless dielectric sample, we still encountered a higher resistance value for thicker mica which is possibly due to an unexpected dielectric loss inside the mica nanosheet and needs further treatment. Lastly, we hope that such type of electrical characterization using FM-AFM by preserving the tip and sample natural environment will be added some extra new information for the nanodevice fabrication where the most demanded properties such as resistance, capacitance, charge distribution on surfaces along with current conduction, heat generation may differ from our expectation to the nanoscale from that of microscale.

## 5.2 Future Prospect:

FM-AFM-based characterization of 2D materials, nowadays, getting attention as it can extract nanoscale surface properties by ensuring the environmental originality of the sample surface with almost no or little damage which is essential for nanodevice fabrication. Based on our experience, we can conclude the following prospects –

- In the nearest future the definite open question regarding the tendency to increase the resistance over the thicker mica layer will be reinvestigated and explained according to the experimental results.
- As this present work is entirely focused on linear relationship between dissipation and electrostatic interaction by removing distance and bias dependence, next we will try to modify the dissipation equations including the mica dielectric constant ( $\epsilon_r$ ) where distance dependence with the relative electric field changing will be considered.
- Through our present research work, we found the mica layer folding phenomenon on Ir/Si substrate i.e. thin layer of mica had been folded and made the folded region height doubled concerning the unfolded region. We want to perform electrical characterization over this region.

### 5.3 Probable Application:

- This method is applicable to observe energy dissipation and the elementary surface charge's behavior without considering distance and bias dependence for any surfaces under electrostatic interaction consisting of metal, dielectric or semiconducting surfaces without disturbing the tip-sample's physical structure.

### Scientific Contributions:

#### List of publications:

- i) **M. M. Hasan**, T. Arai, and M. Tomitori, Jpn. J. Appl. Phys. **61**, 065006 (2022).

## **Domestic conferences: (Oral presentation)**

- i) M. M. Hasan and M. Tomitori, “Dissipative interaction via capacitive coupling through mica nanosheets examined by non-contact atomic force microscopy”, the 81st JSAP Autumn Meeting 2020, September 8– 11, 2020, Online virtual meeting, Japan.
  
- ii) M. M. Hasan and M. Tomitori, “Dissipative interaction due to Joule heat through displacement current on mica nanosheets examined by non-contact atomic force microscopy”, Annual Meeting of the Japan Society of Vacuum and Surface Science, November 19–21, 2020, Online virtual meeting, Japan.
  
- iii) M. M. Hasan and M. Tomitori, “Observation of mechanical energy dissipation between a conductive tip and a thin dielectric film on a metal-coated Si-substrate by frequency modulated atomic force microscopy”, The 68th JSAP Spring Meeting 2021, March 16–19, 2021, Online virtual meeting, Japan.

## **International conferences: (Oral presentation)**

- i) M. M. Hasan and M. Tomitori, “Mechanical Energy Dissipation via a Thin Mica Film on a Metal-Coated Si Substrate Measured by Frequency Modulation Atomic Force Microscopy”, the 28th International Colloquium on Scanning Probe Microscopy (ICSPM28), December 10–11, Online virtual meeting, Japan.